TU Clausthal

HCF Property Improvement through Microstructure Optimization and Shot Peening in $(\alpha + \beta)$ Ti Alloys

Doctoral Thesis
Dissertation
To be awarded the degree
Doctor of Engineering (Dr.-Ing.)

Submitted by
Shan Yang
from Wuhan, PR China

Approved by the Faculty of Natural and Materials Science
Clausthal University of Technology

Date of oral examination
14. August 2014

Chairperson of the Board of Examiners

Prof. Dr. Arnold Adam

Chief Reviewer

Prof. Dr.-Ing. habil. Lothar Wagner

Reviewer

apl. Prof. Dr. rer. nat. Dr.-Ing. habil. Heinz-Günter Brokmeier

Acknowledgement

My sincere gratitude is dedicated to my PhD. supervisor Prof. Lothar Wagner for his generous offering of scientific guidance, considerate support and persistent encouragement, without which this work could not be implemented fluently. Besides, I am so thankful to the co-referent Prof. Heinz-Günter Brokmeier for his critical discussion and suggestions covering part of the work.

The appreciation also goes to all the members in our research group. Especially I would like to thank Mr. Christian Teichmann, Mr. Mansour Mhaede and Mr. Zheng Ye Zhong for their kind support and help in carrying out shot peening and synchrotron radiation.

I would like also to thank all the technical staffs at IWW for their selfless support and warm-hearted help during performance of the practical work, particularly, Mr. Jörg Schumann who is in charge of the metallography laboratory, Mr. Gerd Neuse for his patient guidance on the operation of testing equipments and Mr. Peter König for performing SEM.

I am particularly grateful to China Scholarship Counsel for sponsoring me to achieve a PhD. degree at IWW, TU Clausthal.

At last, my deepest gratitude and love belong to my beloved mother and sisters for their selfless support and caring as always, no matter where and what I am.

Abstract

This work is focusing on investigating the high cycle fatigue behaviours (HCF) of Ti-6246 and TIMETAL-54M under various work conditions and improving HCF through microstructure optimization by means of thermo-mechanical processing (TMP) and shot peening (SP).

TMP routes were designed to develop different sorts of microstructures. Optical microscope (OM) and high energy synchrotron X-ray diffraction (HESXRD) were utilized to characterize the microstructures and phase constitutions, respectively. HCF of various microstructures was evaluated under rotary bending load (R-B) to clarify its microstructural dependence. The optimal microstructure was opted for surface strengthening by SP. To investigate the influence of loading mode, mean stress and environment, axial fatigue tests were carried out on the electro-polished (EP) optimal condition under different test parameters. The effect of SP was also determined on the peened specimens under axial load at both RT and 450 ℃. Characterization of surface roughness, microhardness and residual stress depth profiles of the peened and thermo-relaxed samples was performed using profilometer, microhardness tester and hole drilling method to help interpret the role of SP playing in HCF. Positioning of the crack nucleation sites and observation of fracture characters in fatigued specimens were conducted using scanning electron microscope (SEM) to elucidate the mechanisms of crack nucleation.

The results achieved by OM and HESXRD confirm the martensitic transformation in Ti-6246, which reaffirms the alloy's classification into ($\alpha + \beta$) group. Duplex structure with 10 % primary α grains (α_p) stands out for Ti-6246 with great advantage in HCF in comparison to the other microstructures and the as-received condition. The alloys exhibit high sensitivity to loading mode. Mean stress sensitivities are proven to be normal, regardless of test temperature. Increase in temperature from RT to 450 ℃ only results in minor decrease in HCF. The thermal stability of Ti-6246 in HCF is satisfactory. The material shows superior HCF performance in vacuum to that in the air. At RT, SP contributes a moderate improvement in HCF. As increasing temperature to 450 ℃, fatigue limits are maintained. While, lifetimes at high stress amplitudes decrease due to the overwhelming detrimental effect of deteriorated surface finish after SP against the residual compressive stress. Fatigue crack nucleation (FCN) at subsurface region in EP condition is commonly observed within conventional fatigue regime ($\sim 10^7$ cycles), despite of load ratio. The likelihood of subsurface FCN is found to increase with the decrease of stress levels. Multi-competing crack nucleation modes are operative, strongly depending on local microstructural configuration.

Abstrakt

In dieser Arbeit wird das Langzeitermüdungsverhalten (HCF) von Ti-6246 und TIMETAL-54M nach Gefügeoptimierung mittels thermo-mechanischer Behandlung (TMP) und nach Kugelstrahlen (SP) untersucht. Durch Lichtmikroskopie (OM) und Synchrotron-Röntgenbeugung (HESXRD) wurden die verschiedenen Mikrostrukturen und Phasen charakterisiert. Das HCF-Verhalten wurde an beiden Legierungen unter Umlaufbiegebelastung (RB) untersucht. Die optimalen Mikrostrukturen wurden für die Oberflächenverfestigung durch SP gewählt. Um die Einflüsse der Belastungshöhe, der Mittelspannung und des umgebendes Mediums zu untersuchen, wurden axiale Ermüdungstests an elektropolierten (EP) Zuständen unter verschiedenen Testparametern durchgeführt. Der Effekt von SP wurde durch Vergleich von EP-Proben und kugelgestrahlter Proben unter axialer Belastung bei Raumtemperatur (RT) und 450 ℃ bestimmt. Die Charakterisierung der Rauhigkeit, Mikrohärte und Eigenspannung von den gestrahlten und spannungsarmgeglühten Proben wurde mit Profilometer, Mikrohärteprüfer und Bohrlochmethode durchgefühlt. Eine Untersuchung der Rissbildungsorte und der Bruchmechanismen wurden durch Rasterelektronenmikroskopie (SEM) durchgeführt.

Die von OM und HESXRD erzielten Ergebnisse bestätigen die martensitische Umwandlung in Ti-6246 nach Abschrecken von Temperaturen oberhalb des Beta-Transus. Die Duplexstruktur mit 10 % primär α-Körner (α_p) zeigt in Ti-6246 große Vorteile im HCF-Verhalten im Vergleich zu den anderen Mikrostrukturen. In beiden Legierungen wird eine normale Mittelspannungsempfindlichkeit der Schwingfestigkeit beobachtet. Eine Erhöhung der Testtemperatur von RT auf 450 ℃ zeigt in Ti-6246 nur eine geringfügige Abnahme in der HCF-Festigkeit. Die thermische Stabilität von Ti-6246 bei der HCF-Beanspruchung ist zufriedenstellend. Das Material zeigt überlegene HCF-Festigkeiten im Vakuum und an Laborluft. Bei einer Erhöhung der Testtemperatur von RT auf 450 ℃ ändert sich die Ermüdungsfestigkeit nicht, nur bei hohen Spannungsamplituden wird die Lebensdauer aufgrund der nachteiligen Wirkung der kugelstrahlbedingten hohen Rauhigkeit und der reduzierten Druckeigenspannungen abgesenkt. Ermüdungsrissbildung (FCN) unter der Probenoberflächen wurde im Bereich der Langzeitermüdung allgemein beobachtet. Die Wahrscheinlichkeit von FCN unter der Oberfläche nimmt mit der Abnahme der Belastung zu. Multi-competing Rissbildungsphänomene sind in Ti-6246 stark abhängig vom lokalen Gefüge.

Table of contents

1. Introduction

In 1791 titanium was first discovered as a new metallic element by the British mineralogist William Gregor in England, and was named Titanium four years later by the Chemist Martin Heinrich Klapproth after the Titans from Greek mythology due to the analogy between the difficulty in extracting ore and the captivity of Titans by their father Uranos under the earth. At the end of 1930s (1937-1940) chemist Wilhelm Justin Kroll from Luxemburg achieved a significant amount of Titanium through a reduction of $TiCl_4$ with magnesium in an inert gas atmosphere [1, 2]. The resulting product is called titanium sponge due to its porous and spongy morphology. And this process is named 'Kroll process' after the inventor. Even up to date it is still the most widely used extracting method for Titanium. Based on the aforementioned development, in 1948 Titanium was first commercially produced by the DuPont Company in USA with the driving force for military application. As after the World War II, titanium based alloys were considered as the key materials for manufacture of aircraft engines. It is sarcastic that the greatest propulsion and interest in the production and development are always found in the military concerns as well as for plenty of other research objects.

With a commercial production history of 65 years, Titanium and its alloys are relevantly new in structural materials family. But titanium industry boomed up drastically during the past decades. The most competitive attributes of titanium alloys are high strength to weight ratio (specific strength), low density (4.51 g/cm3), superior corrosion resistance (resistance to chlorides, seawater, sour and oxidizing acidic media) and exceptional elevated temperature properties. These attributes explains why titanium and its alloys stand out for applications in aerospace sector, chemical processing, medical engineering, marine, power generation, leisure and sporting goods.

With a weight fraction of about 0.6 % in the earth's crust, titanium is listed as the ninth most abundant element and the fourth richest structural metal after aluminium, iron and magnesium [3, 4]. In nature titanium usually occurs in mineral sands containing ilmenite ($FeTiO_3$) and rutile (TiO_2). Significant deposits of Ti containing ore are found in Australia, China, Russia, Kazakhstan, Ukraine, India, South Africa and Mexico [5]. Initial input raw materials for titanium metal production include rutile and upgraded titanium rich slag derived from ilmenite [6]. World production of Ti mineral concentrates (ilmenite and Rutile) in 2011 [7] is shown in Fig. 1.1. Major production in 2011 was found in Australia (26 %), China (15 %) and

Vietnam (13 %). Whereas titanium metal production just accounts for a small portion of the total ore minded, around 5 % in 2010 and may reach 8 % by 2018 [8]. This suggests that the titanium metal industry is not strongly dependent on the supply and demand for ore and the exploitation of new deposits.

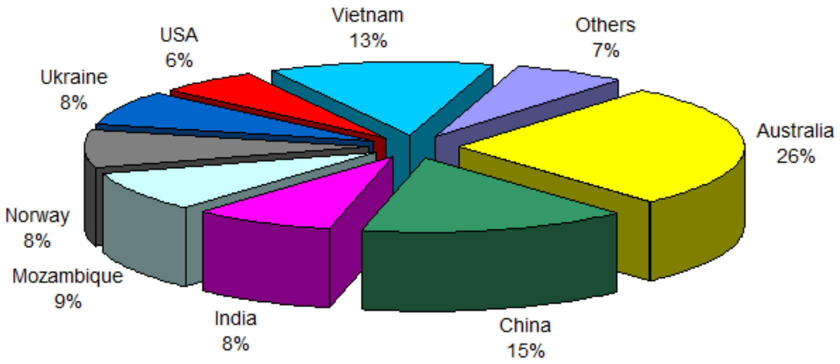

Figure 1.1, World production of titanium mineral concentrates (ilmenite and rutile) in 2011.

Commercial production of titanium metal involves the chlorination of titanium mineral concentrates to produce titanium tetrachloride ($TiCl_4$), which is then reduced with magnesium (Kroll process) or sodium (Hunter process) to produce a commercially pure form of titanium metal, referred as sponge due to its form. Titanium sponge is regarded as the basis of this industry, as it is the raw material for mill products, powder and other components. Its production is an important index of industrial output. According to data of U.S. department of interior and Roskill consulting group [9, 10], a pie chart in Fig. 1.2 is fabricated to present the world production of titanium sponge in 2012. The world total output reached 241000 t. China has achieved a major share of 32 %. USA succeeds with 21 %. Then Russia and Japan follow with 17 %. There was a global sponge surplus of 20000 t mainly contributed by industrial (standard) grade production in China. This indicates an excess capacity in Chinese titanium industry, which should be taken as a signal of warning. The buyer's market is mainly induced by two factors, one is the world economic crisis since 2008 which slows down the demand growth, and the other is the over-investment in sponge production in China. Moreover, most of China's output is of industrial grade for the domestic market. In Japan, Russia and Kazakhstan it is mostly of aerospace grade for export. Hence, an adjustment in configuration of graded sponge products could be suggested in China in order to meet the need of world market for aerospace graded sponge and to ease the pressure of excess production in domestic market.

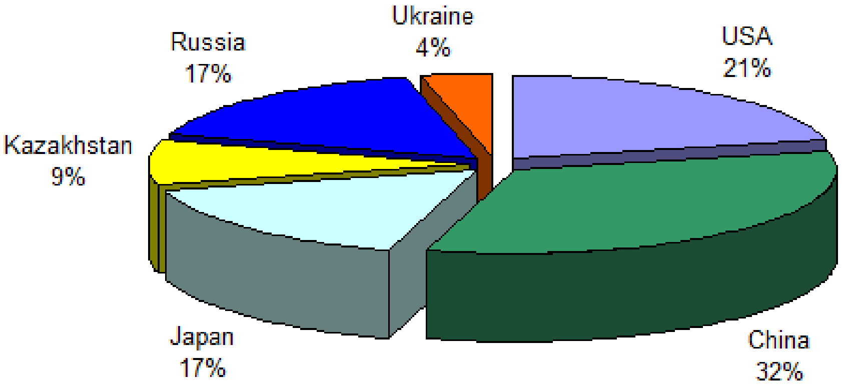

Figure 1.2, World production of titanium sponge in 2012.

Titanium ingot is produced by melting titanium sponge, scrap and alloying elements by means of electron beam, plasma melt, scull or vacuum-arc remelting. Mill products are then produced from drawing, forging, and rolling ingots into products of various sizes and shapes. Fig. 1.3 shows the output of titanium mill products in the main titanium manufacture countries and regions [11]. The total production in the world is more than 110000 t at the end of 2010. The output of China takes up a portion of 34 %, closely followed by USA with 31 %. Production of mill products is still growing significantly in countries such as China and USA, especially for aerospace application. Till the second quarter of 2013, titanium mill products shipments in USA reached 18500 t. Approximately 75 % of the mill products and castings in the second quarter were produced for commercial and military aerospace applications [12].

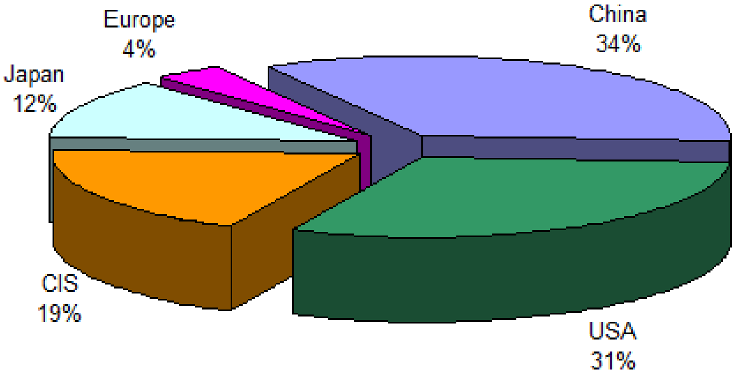

Figure 1.3, World production of titanium mill products in 2010.

Based on the aforementioned chart and data, the thrust of aerospace application in Titanium industry is self-explanatory. Hence alloy development routes focusing on applications for aero-engines, especially for elevated temperature sections were oriented strategically. One of the aim alloys in this study Ti-6Al-2Sn-4Zr-6Mo (Ti-6246) was first produced by Pratt & Whitney at this background in early 1970s. It is a solid-solution-strengthened alloy that responds to heat treatment as a result of the beta-stabilizing effect of its 6 wt. % molybdenum. Silicon addition up to 0.08 % improves creep resistance. This alloy combines virtues of the long-term, elevated-temperature strength properties of Ti-6Al-2Sn-4Zr-2Mo-0.08S (long-term load-carrying applications at temperatures up to 400 ℃ and short-term load-carrying applications up to 540 ℃) and much improved short-term strength levels of a fully hardened (α + β) alloy [13]. Ti-6246 is mainly used for forgings in intermediate-temperature sections in aero-engines, such as compressor disks, blades, seals and airframe components. It replaces Ti-6Al-4V (Ti-64) because of its higher basic strength and better temperature endurance. It is also under evaluation for deep, sour-well applications.

The other targeted alloy within this work is an (α + β) alloy TIMETAL-54M with a nominal composition of Ti-5Al-4V-0.75Mo-0.5Fe. It was newly developed by TIMET on the basis of modifying the working horse of titanium alloys family Ti-64. The addition of small amounts of β-stabilizers Mo and Fe and reduction in Al-content compared to Ti-64 lead to lower β transus temperature and improved formability (lower working temperatures and working stresses). In addition, work has shown that the machinability is also improved through higher cutting speed and/ or improved cutting tool life compared to Ti-64 [14–17]. Thus, the application of this alloy is particularly interesting for components that require intensive machining and can provide a cost benefit over Ti-64. TIMETAl-54M also covers the traditional application field of Ti-64 such as medical and chemical industries, and aerospace sections working under 350 ℃.

Problem definition and objectives

Nowadays the ever-increasing interest in aerospace industry of these two alloys requires correspondent development in determination of the microstructure-mechanical property relationship, and the beneficial application of specific microstructures in component design for optimized mechanical performance. Hence four issues are involved. First accurate characterization of phase and microstructure evolution through various TMP should be carried out. Second, considering the working environment in fatigue failure-critical aerospace components, optimization of microstructure regarding HCF properties is also set up as a target. HCF behaviour of various microstructures generated through TMP will be determined. Meanwhile effects of TMP on microstructure and HCF properties could be also elucidated. Third aim is to investigate the effects of testing conditions on HCF behaviour, such as loading mode, mean stress, testing temperature and ambient environment. In addition, attempt to improve the HCF performance by means of surface mechanical treatment SP will be made. The effect of SP on the HCF behaviour will be examined.

Characterization of phase and microstructure evolution through TMP

The focus of this study upon these two-phase alloys is concerning the mechanical properties esp. HCF, which is very sensitive to the microstructure (geometrical arrangement of the two phases). The microstructure is highly dependent from details of TMP used in the production, such as recrystallization temperature, cooling rate and aging. That's why microstructure examination using microscopy is indispensable. Furthermore its evolution whilst TMP route with the above mentioned processing variables should also be investigated to clarify the effect of TMP on microstructure. It is of great importance to provide a physical perspective to assist the analysis of its mechanical performance and to ascertain the relationship between microstructure and mechanical properties.

On the other hand, phase characterization is very necessary, as for long the classification of Ti-6246 remains controversial because of the complexity in identifying whether the alloy transforms martensitically while quenching from high temperature. In USA, Great Britain and France it is widely recognized as an ($\alpha + \beta$) alloy [13, 18, 19], which is characteristic of the transformation into martensite with orthorhombic crystal structure (α'', space group C_{mcm}) during fast cooling from above a certain temperature [20–22]. Based on the pseudo-binary β-isomorphous phase diagram, it should be classified into ($\alpha + \beta$) group with its 6 % Mo. However, researchers in Germany represented by G. Lüterjing [3] concluded martensitic features observed under OM as artefacts induced by improper mechanical surface finishing procedures such as grinding and polishing, i.e. stress-induced. They consider Ti-6246 as a near-β alloy. Therefore HESXRD comes into our focus for quantitative phase identification, because of its large penetration depth which imparts the possibility to detect phases in the bulk material, while excluding the involvement of intensive mechanical surface finish preparation.

Optimization of microstructure regarding HCF properties

For aerospace alloys, major rotating components in engines are designed against fatigue on the basis of 'life to first crack' (initiation controlled, HCF) criteria or through crack propagation (damage tolerance) calculation procedures [23]. Hence in this study, microstructures will be optimized regarding HCF properties. Different sorts of microstructures for both alloys will be developed through hot-rolling based TMP. Specifically for Ti-6246 duplex structure with around 30 % α_p (D30), duplex structure with 10 % α_p (D10) and fully lamellar structure (FL) will be generated through TMP. The typical fully equiaxed structure (EQ), D40 and FL will be produced for TIMETAL-54M. HCF testing under rotary-bending load is planned to determine the fatigue strength limits of the developed microstructures. Hence, the influence of microstructure on HCF could be revealed. The optimal structure will be selected for the following HCF tests under various conditions.

Effects of testing conditions on HCF performance

There are many possible factors which may influence HCF performances of Ti alloys, such as loading mode, mean stress, testing temperature and atmospheric environment. Further HCF tests will be implemented on electro-polished specimens under axial load at both load ratio ($R = \sigma_{min}/\sigma_{max}$) -1 and 0.1. In comparison with the fatigue behaviour under the aforementioned rotary-bending load (R-B), the effect of loading mode could be analyzed. At axial load, mean stress effect could be attained according to fatigue limits at $R = -1$ and 0.1, respectively. As a material for application in aero-engines, Ti-6246 should also be examined for its thermal stability of HCF at elevated temperature (450 ℃). Fractographic study was done to understand the possible influence of these factors on FCN mechanism. Fatigue failure initiating from subsurface is frequently observed, although HCF tests applied are within conventional fatigue limit ($\leq 10^7$ cycles), during which surface crack nucleation is predominant [24]. The relationship between the local microstructure such as macrozone and the crack initiation modes is to be investigated. HCF in vacuum was scheduled to display whether there are atmospheric impacts on crack nucleation.

Effects of SP on HCF performance

Some other influence factors on HCF are surface finish, work-hardened layer and residual stress and so on. These could be introduced by mechanical surface treatments. The benefits in promoting HCF performance by proper mechanical surface treatments are widely reported. Attempt to improve HCF by means of SP will be made. The effect of SP will be examined at both RT and 450 ℃. In order to interpret the possible influence of SP on HCF, it is obliged to study the SP-induced variation in surface finish, work-hardening and residual stress and the thermal stabilities of these properties. Therefore, surface profilometer, microhardness-tester and hole-drilling methods will be employed to perform the measurements.

2. Theoretical background

2.1 Basic metallurgy of Ti alloys

2.1.1 Crystallographic phases

Titanium is an allotropic element, which occurs in several different crystallographic forms. At room temperature, pure titanium exists as a close-packed hexagonal crystal structure (hcp), termed α phase. With the increase of the temperature to 882 ℃, it exhibits an allotropic phase transformation, changing to a body-centred cubic crystal structure (bbc), called β phase [3]. The crystal structures of α and β are illustrated in Fig. 2.1 [4]. The transformation from α to α phase in titanium follows the Burgers relationship [25] same as that reported for zirconium and lithium, namely:

$(0002)\alpha \parallel (110)\beta, \quad [11\bar{2}0]\alpha \parallel [111]\beta$

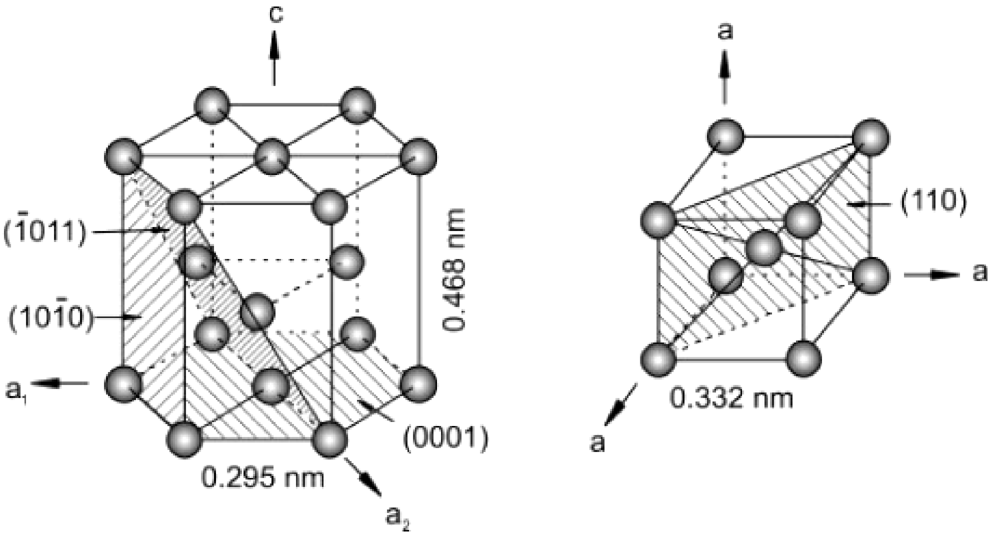

Figure 2.1 Crystal structures of hcp α and bcc β phase

The transformation temperature to β phase (β transus, T_β) of an alloy is strongly dependent on interstitial and substitutional elements, such as inpurities or alloying elements. Depending on the influence on T_β, the alloying elements in titanium are usually classified as neutral, α-stabilizers, or β -stabilizers (Fig. 2.2).

Neutral elements such as Sn and Zr have only minor influence on T_β. However, the so called 'neutral' is only regarding their effect on T_β. If strength is concerned, they are not neutral, in fact they could strengthen α phase.

The α-stabilizing elements extend α phase field to higher temperatures, i.e. they increase the T_{β}. The substitutional element Al and the interstitial elements O, N and C are all strong α-stabilizers. Al is the most widely applied alloying element in titanium alloys, as it is the only common metal raising T_{β}, and showing high solubility in both α and β phases. Attempt has been made by Rosenberg [26] to merge the effect of α-stabilizers as an equivalent Al content ($[Al]_{eq.}$) by the following equation:

$[Al]_{eq.} = \quad [Al] + 0.33\,[Sn] + 0.17\,[Zr] + 10\,[O]$

It should be noted that with the presence of Al, neutral stabilizer Sn and Zr behave as α-stabilizers which strengthen α phase by solid solution strengthening. That is why in the $[Al]_{eq.}$ equation they are counted. Due to the poorer ductility and the deformation capability of α phase compared to β phase, $[Al]_{eq.}$ should not exceed 9 % for alloy development. Otherwise the hard and brittle intermetallics Ti_3Al (α_2) will be over precipitated, resulting in embrittling effect.

While β-stabilizing elements decrease T_{β}, shifting the β phase field to lower temperatures. According to details of the resulting binary phase diagram shown in Fig. 2.2 [4], β-stabilizers are subdivided into β isomorphous and β eutectoid elements. β isomorphous stabilizers, e.g. Mo, V and Ta have a moderate solid solution strengthening effect on β phase, and are more important because of their higher solubility in titanium, and lower tendency in forming brittle intermetallics compared to β eutectoid elements, e.g. Fe, Mo, Cr, Co, Ni, Cu, Si and H. The effect of these β-stabilizers could be expressed in terms of an equivalent Mo content ($[Mo]_{eq.}$) for multicomponent titanium alloy [13]:

$[Mo]_{eq.} = [Mo] + 0.2\,[Ta] + 0.28\,[Nb] + 0.4\,[W] + 0.67\,[V]\ H\text{-}\ 1.25\,[Cr] + 1.25\,[Ni] + 1.7\,[Mn] + 1.7\,[Co] + 2.5\,[Fe]$.

Together with $[Al]_{eq.}$ developed by Rosenberger, these enable the prediction of the constitution of an alloy with a given chemical composition.

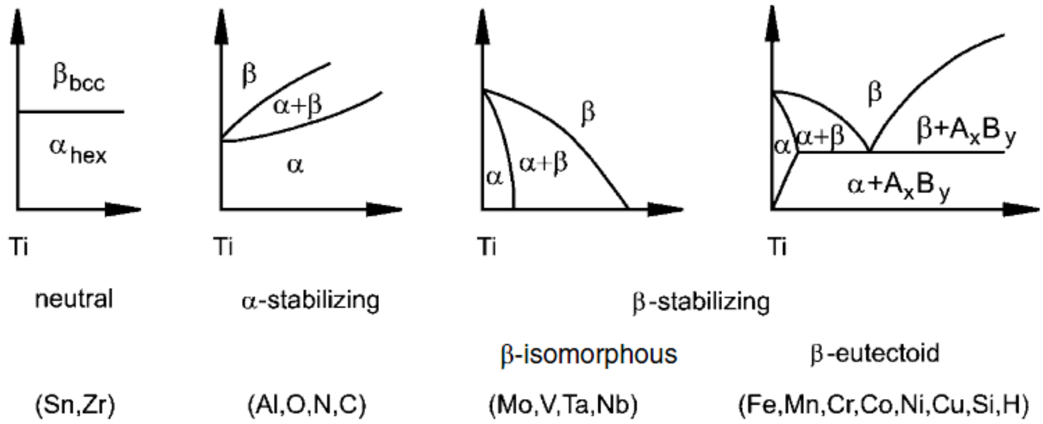

Figure 2.2 Effect of alloying elements on phase diagrams of titanium alloys.

However, it is not explicit enough to exhibit the synergistic effect of both α- and β-stabilizers only using binary phase diagrams. Hence a three-dimensional phase diagram is needed, as shown in Fig. 2.3 [4]. From the side view at the left side, it could be taken as an α-isomorphous phase diagram with $[\mathrm{Al}]_{\mathrm{eq.}}$ as X-axis. Alloys located in this diagram with $[\mathrm{Al}]_{\mathrm{eq.}}$ less than 9 % are called α alloys. The orthograph is a pseudo-binary section through a β isomorphous phase diagram with $[\mathrm{Al}]_{\mathrm{eq.}}$ of 6 %.

Within (α + β) phase field, there is an M_s line, which indicates the martensite transformation temperature. Fast quenching above M_s results in a homogeneous transformation of the bbc β phase into martensite structure with hexagonal crystal structure (α′) or orthorhombic structure (α″). The foot of M_s line ends at 10% $[\mathrm{Al}]_{\mathrm{eq.}}$ [13], which separates (α + β) alloys from metastable β alloys. This means that alloys located beyond this point, i.e. metastable β alloys have M_s lower than room temperature, β could be retained to after quenching, showing no martensite transformation. As a matter of fact this is just the essential distinction between (α + β) and metastable β alloys.

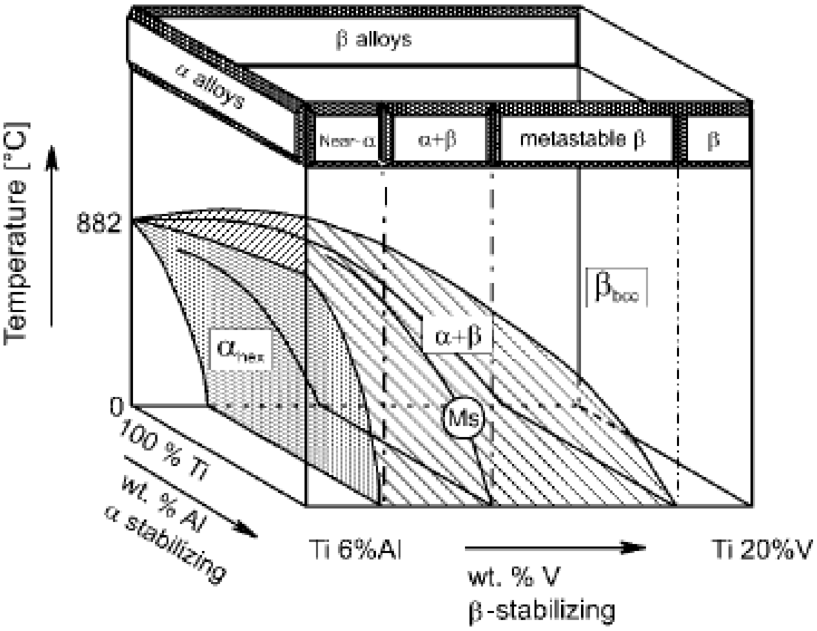

Figure 2.3 Three-dimensional phase diagram.

Another important dividing point within the (α + β) phase field is α′/ α″ martensite boundary located at 4 % $[Mo]_{eq.}$, meaning that alloys with less than 4 % $[Mo]_{eq.}$ such as Ti-64 and TIMETAL-54M possess α′. While with no less than 4 % $[Mo]_{eq.}$ such as Ti-6246 (6% $[Mo]_{eq.}$), alloys transforms into α″. So theoretically Ti-6246 corresponds to an (α + β) alloy. Experimentally, α″ of Ti-6246 was confirmed using OM, laboratory X-ray diffraction (XRD) and transmission electron microscopy (TEM) [20–22]. Meanwhile the difficulty in retaining martensite during the thin foil preparation for TEM has also been emphasized by R.A. Spurling [20], as α″ in Ti-6246 could revert to parent β due to the spontaneous relaxation during the chemical and electrolytic thinning. Whereas, different opinions were proposed by G. Lütjering [3, 27], considering Ti-6246 as a β alloy. They reported that the martensitic features observed under OM were artefacts induced by inappropriate mechanical surface finishing procedures such as grinding and polishing, i.e. stress-induced. However, it was not specified how deep the resultant artificial layer could be. They mentioned that the electro-polished specimens did not show the martensite, although actually no discernible structure was present. While in the case of examination with TEM, the martensitic-like features were again concluded as artefacts deriving from the spontaneous relaxation of β due to the release of the bulk constraint in the foil-thinning process, which is exactly reverse to the conclusion of R.A. Spurling [20]. This is the reason why phase characterization is included as one of the major focuses in this work.

2.1.2 Deformation mechanisms of (α + β) alloys

Plastic deformation in titanium and its alloys involves in twinning and the motion of dislocations. Twinning occurs primarily for the deformation of commercially pure Titanium and some α alloys. In (α + β) alloys twinning is suppressed almost completely by the small phase dimensions, high solute content, and the presence of secondary α (α_s) [3]. In this case plastic deformation proceeds by means of slip of dislocation.

For these kinds of two-phase alloys, slip systems of the two crystal structures hcp α and bcc β will be depicted. Fig. 2.4 [3] indicates the various slip planes and slip directions (burgers vector) in α phase.

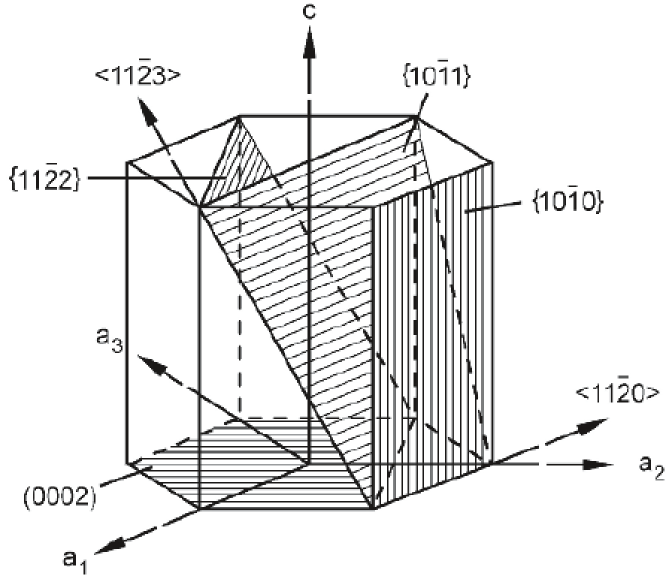

Figure 2.4 Slip planes and directions in the hcp α phase.

In crystal lattices slip planes are those having densest atomic packing, such as basal plane (0002), prism plane $(10\bar{1}0)$, first order pyramidal plane $(10\bar{1}1)$ [28]. Their corresponding burgers vectors are all $<11\bar{2}0>$ ($\vec{a}$, basal burgers vector), the slip direction with the highest linear atomic density. The aggregate number of slip systems based on the above three types of slip planes and slip directions is 12 [29, 30], which could be reduced to 4 independent ones. According to the von Mises Criterion, five independent slip systems are required for a homogenous plastic deformation of polycrystalline materials. Therefore, another slip system with a non-basal burgers vector must be activated. It was observed by TEM in plenty of titanium alloys that secondary pyramidal plane $(11\bar{2}2)$ could also be involved into slip with the slip direction $<11\bar{2}3>$, i.e. $\vec{c}+\vec{a}$ burgers vector [31, 32]. All slip systems in α phase are listed in Table 2.1 together with those of β phase. Beside the slip systems where the dislocation can move, the driving force of dislocation movement on specific slip planes should also be concerned. That is resolved shear stress, that determines which slip system could be easiest activated. Therefore, Schmid factor (cosΦcosλ) regarding a spatial orientation of a specific slip plane according to the sample coordination and applied stress plays an important roll on dislocation movement. The slip plane with highest Schmid factor (when Φ and λ approach 45°) has the greatest potential to reach critical resolved shear stress (CRSS) at first, and turns activated for slip preferentially. It is confirmed in Ti-6.6Al single crystal that it is much more difficult to activate type 4 slip on secondary pyramidal plane with $\vec{c}+\vec{a}$ vector than type 1-3 slip with $\vec{a}$ vector even for an angle of about 10° between the stress axis and c-axis of the hcp lattice [33].

In β phase, slip with the same burgers vector $\langle\bar{1}11\rangle$ is possible on planes {110}, {211} and {321}, as shown in Tab. 2.1 [28–30]. Obviously β phase has more available slip systems than α phase, and can afford more extensive plastic deformation. Conversely, α phase having fewer active slip systems, is normally brittler.

Table 2.1 Slip systems in hcp α and bcc β phase.

Slip system type	Slip direction	Slip plane	Independent slip systems
		hcp	
1	$\langle 11\bar{2}0\rangle$	$\{0002\}$	3
2	$\langle 11\bar{2}0\rangle$	$\{10\bar{1}0\}$	3
3	$\langle 11\bar{2}0\rangle$	$\{10\bar{1}1\}$	6
4	$\langle 11\bar{2}3\rangle$	$\{11\bar{2}2\}$	6
		bcc	
1	$\langle\bar{1}11\rangle$	$\{110\}$	12
2	$\langle\bar{1}11\rangle$	$\{211\}$	12
3	$\langle\bar{1}11\rangle$	$\{321\}$	24

2.1.3 Hardening mechanisms of ($\alpha + \beta$) alloys

The four hardening mechanisms (solid solution hardening, grain refinement strengthening, strain hardening and precipitation hardening) for metallic materials are all operative in ($\alpha + \beta$) alloys. All the strengthening techniques rely on the principle that restrict or hinder dislocation motion, yielding improvement in materials hardness and strength.

At first, solid solution hardening is basic for both α and β phases. In α phase, interstitial elements could result in significant hardening effect. Substitutional solid solution hardening in α phase is mainly caused by elements Al, Sn and Zr which have fairly large atomic size differences to titanium and also large solid solubility in α phase [3]. In β phase, the solid solution hardening deriving from Fe, Cr and V. Nb and Mo has a moderate hardening effect [34]. Regarding the aforementioned solutes, alloy element partitioning effect (AEPE) should be mentioned. That is the enrichment of α- and β-stabilizers in α and β phases, respectively, during annealing in ($\alpha + \beta$) field [35, 36].

Second, grain refinement strengthening by fast cooling has great influence in ($\alpha + \beta$) alloys, resulting in reduction of α colony size and α lamellae width (spacing), or resulting in martensite as if the cooling rate is high enough. In both cases dislocation density is created which also contributes to hardening. However, it should be noted that martensite transformation in titanium alloys could not lead to significant hardening effect as that in Fe-C alloys because the interstitial oxygen atoms only cause small elastic distortion of the titanium martensite lattice.

The last one precipitation hardening plays an important role in both α and β phases. In α phase, it occurs by precipitation of nano-scaled coherent α_2 particles during aging if the alloy contains more than 5 % Al [35]. α_2 has an ordered hexagonal structure, can be sheared by moving dislocation, resulting in planar slip and extensive dislocation pile-ups. Oxygen is known to stabilize α_2. Owing to the AEPE present during annealing in ($\alpha + \beta$) field, the high concentration of α-stabilizers in α_p could promote the precipitation of α_2, leading to significant hardening effect. For titanium alloys, this is also termed age hardening. Different alloys have different α_2 solvus. Aging lower than the solvus could precipitate α_2, or else, it will be only a stress relieving treatment. For Ti-64, α_2 solvus lies around 550 ℃, and varies up to 600 ℃ depending on the exact Al and O content. Therefore, aging treatment at 500 ℃ for 24 h is applied for Ti-64. Considering the same nominal contents of α-stabilizer in TIMETAL-54M to those of Ti-64, same aging process is applied for TIMETAL-54M in this study. But it should be mentioned that the aging treatment for typical high temperature ($\alpha + \beta$) alloys such as Ti-6242 is below α_2 solvus temperature at 595 ℃ for 8 h, i.e. these alloys always contain of α_2 particles. So as it is the same for Ti-6246 due to the same contents of α-stabilizers.

In β phase, fine α_s can be precipitated during the final aging depending on the specific processing route. α_s can also be formed during cooling at moderate speed (air cooling), if the intermediate annealing temperature is high enough. The other important precipitation hardening in β phase could be achieved through martensite-involved phase transformation. A full acicular shaped hexagonal Martensite (α') structure in Ti-64 could be attained by cooling from above 1050 ℃ at a least rate of 410 ℃/s [37, 38]. Martensite formed through the diffusionless nucleation process during fast cooling is supersaturated in β stabilizers [3]. Upon annealing in ($\alpha + \beta$) phase field, α' in alloys such as Ti-64 could decompose to fine lamellar α_s and incoherent β particles as a needle-like matrix, both of which could highly impede slip of dislocation. In ($\alpha + \beta$) alloys with no less than 4 % $[\text{Mo}]_{\text{eq.}}$, such as Ti-6246), the orthorhombic martensite (α'') could experience a spinodal decomposition during aging, resulting in a precipitation of modulated structure of $\alpha_2 + \beta$ phase. This modulated structure comprises of arrays of very small, closely spaced particles. These disordered, solute rich zones become strong obstacles for dislocation motion, as size difference and misfit bring about remarked hardening effect.

2.2 Fatigue behaviour of ($\alpha + \beta$) alloys

2.2.1 Microstructural dependence of HCF behaviour

The mechanical properties of titanium alloys are essentially determined by two factors: the chemical composition and the microstructure. The chemical composition of the titanium alloys primarily determines volume fraction of α and β phases. TMP applied on the alloys also play a rather critical roll in the microstructure configurations, such as prior β grain size, α_p volume fraction and grain size, colony size of ($\alpha + \beta$) lamellae, and width of α lamellae. To interpret the relationship between microstructure and HCF behaviour, introduction of the microstructures in ($\alpha + \beta$) alloys is necessary. Three kinds of typical microstructures can be developed by varying TMP route: FL, duplex and EQ.

FL is generated by annealing the alloy above T_β, and is composed of ($\alpha + \beta$) lamellae or exactly speaking, α lamellae in β matrix with continuous α layers at prior β grain boundaries. In this structure the most influential microstructural parameter on HCF is α colony size and α lamellae spacing controlled by the cooling rate from the homogenization and recrystallization, because it determines the effective slip length. With the increase in cooling rate, α colony size (slip length) and lamellae spacing decreases and the yield stress $\sigma_{0.2}$ rises [39]. A drastic increase $\sigma_{0.2}$ can be realized by fast quenching because of the martensite transformation accompanied by high dislocation density. HCF strength (resistance to crack nucleation) mainly depends on the first dislocation motion and therefore in most cases on the yield stress. Hence, refinement of α lamellae and colony size could improve the HCF strength. This relationship is termed as α colony effect.

Duplex structure is composed of α_p in a $(\alpha + \beta)$ matrix. The morphology of the matrix changes with the variation in alloy chemistry. In $(\alpha + \beta)$ alloys with less than 4 % $[\mathrm{Mo}]_{eq.}$ such as TIMETAL-54M and Ti-64, it appears usually in the form of $(\alpha + \beta)$ lamellae [40]. Or it can be shaped in a fine particle like structure for alloys with more than 4 % $[\mathrm{Mo}]_{eq.}$, due to the aforementioned spinodal decomposition of α''. Duplex structure could be obtained through four steps TMP: homogenization in β field, deformation in $(\alpha + \beta)$ field, crystallization in $(\alpha + \beta)$ field, and final aging at lower temperatures. The temperature and cooling rate from recrystallization and homogenization determine α_p volume fraction and the α colony size, which are most influential on HCF. According to the three dimensional phase diagram in Fig. 2.3, it could be seen that α_p volume fraction increases with the drop of recrystallization temperature. The more α_p the duplex structure contains, the stronger AEPE will be. α_p will be enriched in α stabilizers especially oxygen. α_2 formed in α_p during final aging will be more than that in $(\alpha + \beta)$ matrix. Thus precipitation hardening will be much prominent in α_p than in the matrix. Therefore in microstructure with higher α_p volume fraction, difference in strengths between α_p and $(\alpha + \beta)$ matrix is intensified (exception should be mentioned that the martensitic transformation induced α_s precipitation from β could prominently compensate the strength difference). As HCF is crack nucleation controlled, crack prefers to initiate on the weaker links, i.e. the relatively weaker lamellae tend to be preferential for crack nucleation. However, higher content of α_p confines α colony size, leading to shorter slip length, which is beneficial in improving HCF strength. These two effects compete with each other. Experimental studies of G. Lüterjing [35] demonstrates the predominant effect of AEPE over α colony effect, i.e. duplex structure with lower α_p volume fraction shows higher HCF strength, although the slip length in it is longer. On extreme example is the FL having no α_p, it exhibits higher HCF strength than duplex [36]. An exception should be mentioned that for duplex structures in alloys with particle like $(\alpha + \beta)$ matrix instead of lamellar matrix, there is no α colony effect. And it is still not fully investigated how the matrix involves itself into the slip mode as well as how it interacts with AEPE. Therefore, experimental work is planned in this study on Ti-6246, as if this alloy does transform to α″.

EQ is another extreme type of duplex structure, mainly consisting of equiaxed α_p with small amount of β located at the triple points of α_p grains and grain boundaries as seams. The TMP route to develop EQ is similar to that for duplex, with only recrystallization temperature lower than the latter. The slip length in α_p is the most decisive parameter influencing HCF. Hence, grain refining by high rate cooling from homogenization could be an effective way to improve HCF strength.

Among three kinds of microstructures, EQ has a good combination of ductility and HCF (excellent resistance to fatigue crack nucleation) due to its fine microstructure [40]. FL exhibits superior fatigue-crack growth resistance to fine grained structures. This is attributed to a crack path which is characterized by a high degree of crack deflection, bifurcation and secondary cracking, and also a high degree of crack closure (roughness induced) [41]. Duplex structures combine compromised advantages of EQ and FL, displaying a well-balanced ductility and strength level. In order to diminish AEPE, volume fraction of duplex structure should be limited to about 15 % [35].

2.2.2 Influence of loading mode

It is tacitly assumed that fatigue under cyclic tension and cyclic bending are not much different [42]. But the difference between fatigue under cyclic tension-compression and under cyclic bending is not fully characterized.

These two loading modes lead to different stress profiles perpendicular to the material surface. Cyclic bending such as rotary-bending has a constant load ratio $R = \sigma_{min}/\sigma_{max} = -1$, showing σ_{min} at the geometrical center of the specimen and σ_{max} at the surface. As fatigue is an accumulative consequence of cyclic slip in slip bands carrying the maximum shear stress, which involves in cyclic plastic deformation as a result of moving dislocations. Correspondingly in the case of bending load, fatigue crack nucleation (FCN) emerges always at the specimen surface, because the presence of σ_{max} at the surface leads to the highest tendency in occurrence of maximal resolved shear stress in slip bands. While under a cyclic tension-compression load, a fully reversed axial load with the same $R = -1$, a certain cross section perpendicular to the surface always experience a homogeneous stress distribution simultaneously. Although there is no stress gradient, FCN at the surface still dominates, because micro-plasticity can occur more easily in grains at the material surface as the surrounding material is present at one side only. However, it is worth noting that inhomogeneous stress distribution in the bulk materials due to a notch effect of a pore or other discontinuities such as inclusions in high strength steels [43–48] and nickel based superalloys [49–52] may act as fatigue crack nuclei, leading to FCN under the surface and even a concomitant fish eye. But the effects of discontinuities on the crack nucleation under these two loading modes also differ from each other. M. Nakajima [53] has reported on a high strength carbon chromium steel that under rotating bending, most of the crack nuclei and fish eyes are very close to the specimen surface, while under axial load, crack initiating sites are much deeper. One important reason is related to inclusion size, location and number [54]. Another reason lies in the variation of control volume in specimens under two loads. The control volume under rotary bending load is only limited on the surface layer where the stress is maximum because of the stress gradient. And this control zone is much smaller than that under axial loading, which covers through the whole cross section with the minimum diameter. As a result, fatigue limit is much lower under axial load than under rotary bending load due to the higher probability of subsurface FCN from the discontinuities. Y. Murakami et al. [55] have predicted that subsurface fracture with fish-eye is significantly affected by loading condition.

Considering the fact that titanium alloys are relatively free from pores and inclusions, unlike steels and nickel based superalloys, it is supposed that discontinuities in titanium alloys due to local microstructural configuration might be more probably to function as crack nuclei.

Regarding the aforementioned, it is still early to take it for granted that fatigue under these two loading modes are comparable, experimental studies are required to display the possible effect of loading modes, although some studies [56] have been carried out, taking these two fatigue limits replaceable.

2.2.3 Mean stress sensitivity

The mean stress of the applied cyclic load is known to play an important role in fatigue behaviour of titanium alloys. A tensile normal mean stress has a detrimental effect on fatigue strength, whereas, in general, a compressive normal mean stress has a beneficial effect on it [57]. It is reported that subsurface FCN is strongly dependent on mean stress. For titanium alloys, as increasing mean stress the FCN sites of titanium alloys shift from surface at $R = -1$ to subsurface at $R > 0.1$ [58]. In order to facilitate the interpretation of relationship between mean stress and Fatigue behaviour, some models are to be introduced. As an instance, the common rotary bending load provides a load cycle of sinusoidal waveform. Its stress range, stress amplitude and the mean stress could be denoted as:

$\sigma_a = \sigma_{max} - \sigma_m$ (1)

$\sigma_m = (\sigma_{max} + \sigma_{min})/2$ (2)

$R = \sigma_{min}/\sigma_{max}$ (3)

The S-N curve with σ_a as a function of cycles to failure is actually also a function of the applied σ_m. For a given σ_a, as increasing in mean stress, the fatigue life decreases, in other word, the fatigue limit in terms of σ_a decreases too [59]. One of the most well known models to present this mean stress effect is the Modified Goodman relation [60]:

$\sigma_{a\,|\,10^7} = \sigma_{a\,|\,\sigma m = 0}\ \{1 - \sigma m \ /\ UTS\}$ (4)

$\sigma_{a\,|\,\sigma m = 0}$ is the fatigue strength in terms of σ_a when the R is equal to -1, i.e. under fully reversed load. σ_y and UTS are the yield stress and ultimate tensile strength, respectively.
The fatigue strength ends up at zero if the σ_m is as high as UTS. At even a small σ_a, σ_m = UTS should immediately results in failure as σ_{max} > UTS. With the decrease in σ_m, the fatigue strength rises, until the $\sigma_m = 0$, fatigue strength reaches σ_a. The modified Goodman relationship displays a linear decrease of the fatigue strength as increasing σ_m. From (2) and (3), it could be deduced the relationship between σ_{max} and σ_m:

$\sigma_{max} = 2\ \sigma_m\ /\ (1+R)$ (5)

Inputting (1) into (4), the modified Goodman relationship could be converted into the equation of σ_{max} and σ_m:

$\sigma_{max} = \sigma_{a\,|\,\sigma m = 0} + \sigma_m\ (1 - \sigma_{a\,|\,\sigma m = 0}\ /UTS)$ (6)

R and $\sigma_{a\,|\,\sigma m = 0}$ are constants during a test. Thus both equations (5) and (6) could be plotted in a diagram with σ_{max} as a function of σ_m. This diagram is the so called Smith-diagram. The intersect of the two linear functions as shown in Fig. 2.5.a is the coordinate of the estimated σ_{max} at R = 0.1 based on the modified Goodman relationship. J. Schijve [42] noted that this approximation is conservative for titanium alloys which could show fatigue strength somewhat higher than the estimated value from the diagram. This behaviour along with well estimated one are denoted as normal mean stress effect or sensitivity (NMSS). Practically, NMSS could be indicated by a prominent improvement in strength limit (in terms of σ_{max}) when R increases, for example from ratios such as -1 to 0.1 [58]. On the contrary, if the experimentally obtained fatigue strength at R = 0.1 is lower than the estimation, i.e. close to that at R = -1 (Fig. 2.5.b), the mean stress sensitivity of the material is then anomalous (AMSS).

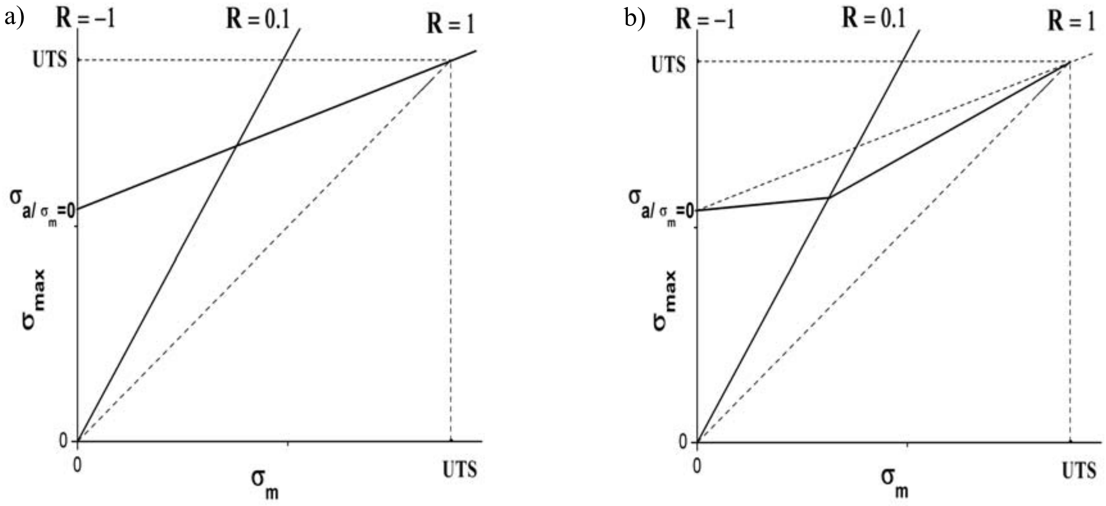

Figure 2.5 Smith diagram (a) normal mean stress sensitivity (NMSS), (b) anomalous mean stress sensitivity (AMSS).

Mean stress sensitivity was examined in various titanium alloys. AMSS is widely observed in air cooled (AC) duplex structures in (α + β) alloys such as Ti-64 [61], Ti-5Al-2.5Fe and Ti-6Al-7Nb [62] and near α alloys such as Ti-1100 [63]. J. Lindemann [56, 62] concluded that the prerequisite of the presence of AMSS is a strength differential of at least two components in microstructure such as the air cooled duplex structures in (α + β) and near α alloys. Due to the significant precipitation hardening effect of α_s, α_p has a higher strength level than the lamellar matrix. Thus dislocation slip preferentially initiates within the lamellae at lower applied maximum tensile stresses, and pile up against the interface between α_p and lamellae (i.e. α_p grain boundaries), finally resulting to FCN. One of the possible methods to reduce or eliminate AMSS is to enhance the strength of lamellar matrix by increasing the cooling rate from AC to water quenching (WQ) (see hardening mechanisms in 2.1.3). Hence, early plastic deformation in lamellae could be prevented, and mean stress sensitivity turns normal. Although the mechanism of AMSS is not completely clarified, it is confirmed that AMSS is controlled by FCN and independent of environment as it occurs in vacuum too. At high temperature, it is found that AMSS disappeared in TIMETAL-1100.

2.2.4 Environmental effect

Components in aircraft engines such as compressor disks and blades where titanium alloys are widely applied usually are subjected to cyclic load at elevated temperatures. Temperature has a great influence on cyclic slip, which is not fully reversible, partly due to the oxide layer formed at the slip step [42]. In solid solution alloys, the stacking fault energy usually increases with increasing temperature [64]. High temperature accelerates both the motion of dislocation and oxidation at the slip steps. Thus, the combination of surface diffusion of oxygen or other embrittling species and slip step oxidation promotes the irreversibility of cyclic slip, resulting in acceleration in both crack nucleation and propagation [60]. On the other hand, preferential oxidation at certain microstructural parts, such as the intersection of a grain boundary at a free surface, causes microscopic stress concentration (notches) to develop. Micronotches raise the local stresses and promote crack nucleation [65]. Besides, hydrogen and water vapour in the testing environment are also suspected to be active species activating FCN. Hydrogen atoms from gas hydrogen or resulting from the dissociation of water vapour molecules would ingress into the strain materials and subsequently embrittle surface and promote crack initiation. Worth noticing, the above mentioned environment-assisted FCN are limited in surface cracks. The deterioration of fatigue performance at elevated temperature is merely a consequence of environmental interaction.

Studies on the fatigue behaviour of Ti-6242 [66] and Ti-64 [67] demonstrated an enhanced fatigue life in vacuum in comparison to that in the air. The effect of the atmosphere environment is mainly explained by the decreased crack growth rate in vacuum due to the irreversibility of dislocation glides because of the oxidized film at the slip bands in air. The lack of oxidation in vacuum can validate reversible slip along the original slip bands. According to the study of C. Sarrazin-Boaudoux [68], the influence of air environment at 300 ℃ has been attributed to hydrogen embrittlement provided by atmospheric water vapour. At 500℃ or higher temperatures, the enhancement in growth rate is related to the dominant effect of the surface oxidation. The influences of environment on Ti-6246 are complex, up to date, still not fully interpreted.

2.3 Shot Peening

SP is a one of the most widely applied mechanical surface treatments in a wide variety of industrial components. Parts typically shot peened include: crankshafts, springs, gears, valves, exhaust manifolds, turbines and particularly in welding joints. It is an important mechanical surface treatment in automobile and aerospace industries.

SP is a cold-working process in which a component surface is bombarded by tiny shots of steel, cut wire, glass or ceramic. These small shots serving as hammer strike on the surface of the parts being treated, as shown in Fig. 2.6 [69]. The kinetic energy of the shot stream is thus transferred to the material, resulting in plastic deformation on the surface, i.e. dimples. This kinetic energy is evaluated by the so called Almen-intensity. The measurement of the Almen-intensity is accomplished by determining the effect on standard strips made of steel SAE 1070 (Almen Strips). Almen strips are classified into 3 types: ‘A’, ‘N’ and ‘C’. They differ in their thickness, while have the same width and length. ‘A’ strips are predominantly used for SP with cast shots or cut wire shots. ‘N’ strips for glass and ceramic beads. ‘C’ strips are rarely applied and are thicker than the other two. For strengthening the fatigue critical titanium parts, cast shots and cut wire shots are mostly applied. Correspondently ‘A’ strips are involved. The fixed Almen strip is first exposed to the shot stream, and removed from the holding fixture. The arch height of the peened strip measured by a gage (Almen gage) is representing the Almen intensity.

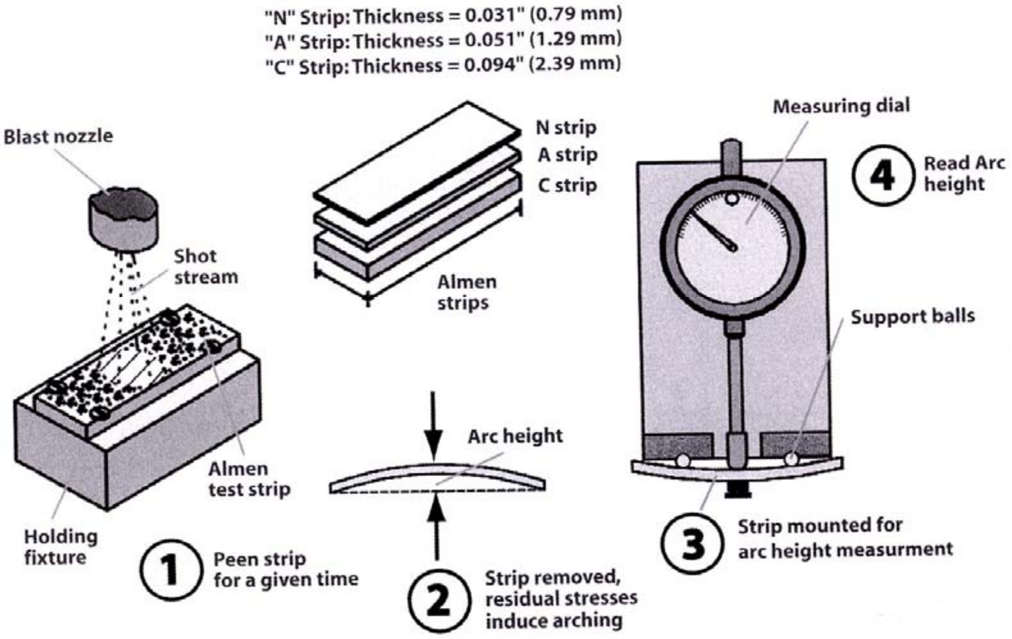

Figure 2.6 Determination of Almen intensity of SP.

2.3.1 Modification of surface properties

In most cases the following three surface properties are modified by SP:

- Surface roughness
- Cold work or dislocation density
- Residual stresses

SP-induced plastic deformation in the near-surface regions leads to a characteristic surface roughness and increases the dislocation density, leading to work-hardening. This could be characterized by the micro-hardness depth profile. The increase in surface hardness depends on the hardening potential of the material as well as the material condition before SP. In the case of highly hardened initial conditions, no additional increase in surface hardness could be achieved by mechanical surface treatments. Exceptionally mechanical surface treatments on highly hardened metals might even result in a reduction of the surface hardness [70]. On the other hand, since the peened surface is plastically stretched, the elastic substrate tries to restore to its original form, the residual compressive stress (RCS) is generated at the surface layer. Concomitantly the residual tensile stress (RTS) appears underneath this surface layer to balance the outer RCS.

2.3.2 Influence on HCF

The above mentioned surface properties have great influence on FCN and fatigue crack propagation (FCP) behaviours. Specific effects of surface properties on the fatigue behaviour in titanium alloys are characterized by L. Wagner et al. Systematically [71], as presented in Tab. 2.2.

Table 2.2 Influences of surface properties on HCF.

	FCN	FCP
Surface roughness	Accelerates	No effect
Cold Work	Retards	Accelerates
Residual compressive stress	Minor or no effect	Retards

The surface roughness determines whether fatigue life is mainly FCN (smooth surface) or FCP controlled (rough surface). High surface roughness could accelerate FCN because surface defects such as notches and dimples induced by SP serve as stress raiser at which cracks may easily nucleate due to stress concentration. Thus FCN phase might be very short or even does not exist at all, fatigue life is then mainly controlled by FCP. As long as the crack emerges, roughness has no effect on FCP since the depths of microcracks even in their early stages are much greater than the maximum roughness. On the contrary, if the surface is smooth, FCN phase dominates in the fatigue life. The influence of SP-induced surface roughness should be evaluated with reference to the original surface quality whether SP increase or lower the roughness. For example, in comparison with an electro-polished original surface, peened condition exhibits a detrimental effect on fatigue owing to the acceleration in FCN. Cold work leads to a retardation of FCN due to the increase in strength. But it is a disadvantage for FCP because of the low residual ductility [4]. Residual compressive stresses could counteract the applied tensile stresses which is the driving force for FCP, thus stress concentration at the crack tip is reduced, crack growth will be slowed down, and FCP is retarded [72–74]. Residual compressive stresses have minor influence on life of FCN [71].

Since the fatigue life is the sum of the number of cycles to FCN and those of FCP, SP-induced modification in surface properties have contradictory effects on fatigue. Experimental studies on various titanium alloys [75–79] confirm the improvement in fatigue properties after SP, i.e. benefits due to the residual compressive stress overcompensate the detrimental effects of cold work and roughness. L. Wagner [80] reported that the fatigue response of various titanium alloys to mechanical surface treatments such as SP depends on their work-hardening capability (work-hardenability) and cyclic deformation behaviour. Severe cyclic softening in meta-stable β alloys leads to only small improvements or even a deterioration in HCF strength after SP. While (α + β) alloys with only slight cyclic softening respond more positively to SP benefits. Presumably, the cyclic deformation behaviour affects the cyclic stability of the process-induced dislocation strengthening and residual compressive stress fields. This implies that cyclic stressing could lead to the reduction in the amount of cold work (dislocation density) and residual stresses. Besides, recovery and recrystallization can also eliminate the amount of cold work. Similarly, thermal relaxation plays also an important roll in the instability in residual stresses, which is related to the healing of crystalline defects, such as dislocation density induced by SP during thermally activated processes [81].

3. Experimental Procedures

3.1 Materials

One of the object materials Ti-6246 was produced by TIMET UK LTD., Birmingham as billets for forging stocks, and then thermo-mechanically processed by Otto-Fuchs KG Germany, which delivered the material in forged disks with diameter and thickness of 300 mm and 80 mm, respectively. The as-received material exhibits a typical β processed microstructure or so called pancake structure (PC), corresponding to a pre-β process. Ti-6246 is a solid-solution-strengthened alloy that responds to heat treatment as result of the β-stabilizing effect of its 6 % Mo content. Meanwhile, the addition of Si could improve creep resistance. The chemical composition characterized by flame emission spectroscopy is listed in Tab. 3.1 in comparison with the specification MIL T-9047. Basic properties according to MIL T-9047G are listed in Tab. 3.2.

TIMETAL-54M with composition displayed in Tab. 3.1 was a newly developed alloy with improved machinability compared to Ti-64. It was supplied by the developer TIMET, Henderson Laboratory, NV (USA) as square bar stocks (38×38 mm^2) in mill-annealed condition. The addition of small amounts of the β-stabilizers Mo and Fe and the reduction in Al-content compared to Ti-64 lead to lower β transus temperature and improved formability (lower working temperatures).

Table 3.1 Chemical compositions of the studied Ti-6246 compared to MIL T-9047G and TIMETAL-54M.

wt. %	Al	Sn	Zr	Mo	V	Fe	Si
Ti-6246	6.04	1.92	4.23	5.90	-	0.08	0.05
MIL T-9047G	5.50~6.50	1.75~2.25	3.60~4.40	5.5~6.5	-	~0.15	~0.08
TIMETAL-54M	5.03	0.03	0.01	0.57	3.95	0.51	0.11

Table 3.2 Typical physical properties of Ti-6246.

Melting range (℃)	T_m	1595~1675
β–Transus (℃)	T_β	935
Density (g/cm^3)	ρ	4.64
E-Modulus at 20℃ (GPa)	E	114
Specific Heat at 20 ℃ (J/ kg·K)	c	500
Thermal conductivity at 20 ℃ (W/m·K)	λ	7.7

3.2 Material processing

The as-received Ti-6246 exhibits an inhomogeneous microstructure, which might result in negative effects on the mechanical properties (confirmed by the under-average strength levels of yield stress and ultimate tensile strength revealed in the pre-investigation on the alloy), and TIMETAL-54M was just obtained in a mill-annealed condition with relatively coarse microstructure, so firstly it is necessary to develop series of TMP for the alloys with the aim of optimizing the microstructures regarding mechanical properties. Furthermore, in order to improve in the HCF, mechanical surface treatment as shot-peening was applied for the specimens to induce working hardening and residual compressive stress in the surface layer.

3.2.1 Thermo-mechanical processing

As one of the most important hardening mechanisms by microstructural configuration for (α + β) titanium alloys depends on the extent of precipitation of the fine α_s or correspondently, the content of α_p, therefore, the following TMP are aiming at generating different types of microstructures with variant proportions of α_p.

a). Ti-6246

Generally 3 types of microstructures are commonly applied, β annealed, normal duplex structures with equiaxed α_p embedded in transformed β phase ((α + β) matrix) and pancake structures characteristic of plate-like α_p within the (α + β) matrix. The microstructural optimization will be performed using the duplex structures as an instance.

The received disks were first sectioned into rectangles (38×38×50 mm^3), then subjected to a four-step TMP. First heat treatment termed homogenization is carried out at 55 ℃ above T_β to assure the whole blocks were thoroughly heated up into β phase field. As implied by the name, it is used to homogenize the materials into fully β phase, free of previous microstructural histories. Following deformation was in the form of hot rolling. The rolling temperature decides the types of microstructures. If the homogenized materials were rolled in (α + β) phase field, i.e. 900℃, the microstructures could be further developed into duplex or β annealed structures, depending on the recrystallization temperature. On the other hand if the rolling temperature reached above T_β, the microstructure would turn into pancake. The deformation degree $\varphi = \ln(l_0 / l_f) = 1.4$ was kept constant for all specimens to size down the thickness of the material to 9mm. Solution treatments were performed on the specimens (9×9×60 mm^3) sectioned in the transverse direction of the rolled sheets at different temperatures which decides the contents of α_p. At last aging is applied on the specimens at 595 ℃ for 8 hours in order to further precipitate α_s. As the alloy was first recognized as metastable β alloy, the aging temperature is selected to be above the solvus temperature of the metastable coherent particles ω and β′, which act as precursors for the nucleation of α_s. So their presence during the heating period to the aging temperature is beneficial to obtain a uniform distribution of fine α_s. Therefore before figuring out identification on the classification of the alloy by the later phase analysis using high energy synchrotron X-ray diffraction, the aging temperature was taken as that in documents where the alloy was considered as a metastable β alloy.

As the main factors determining the microstructures during the TMP are deformation and recrystallization temperature, the TMP for each type of microstructure would be described and illustrated mainly with respect to these two points.

Duplex structures with 30 % α_p in (α + β) matrix (D30)

D30 was obtained by rolling at 900 ℃ and then recrystallization at 900 ℃ for an hour. Two cooling methods from the recrystallization temperature were adopted, fast cooling by WQ with cooling rate at about 8000 K/ min and air cooling (AC) with cooling rate at 400 K/ min approximately, to exhibit the influence of cooling rate on the microstructural features and resultant mechanical properties. The correspondent two microstructures are designated as D30/ AC and D30/ WQ, respectively. Final aging was done at 595 ℃ for 8 hours to precipitate α_s within the β matrix. The procedures are illustrated in Fig.3.1.a.

Duplex structures with 10% α_p in α+β matrix (D10)

As increasing the recrystallization temperature to 920 ℃, α_p proportion decreases to approximately 10 %, indicating that there would be higher content of α_s precipitated from the rest α phase. Same to the above mentioned D30, D10/ WQ and D10/ AC were developed using different cooling methods from 920 ℃ (Fig.3.1.b).

β annealed structures (β)

As the recrystallization temperature reaches 990 ℃ (in β phase field), a fully lamellar structure appears, with most α phase in the form of lamellae within the β matrix. This condition serves as an extreme example with 0 % equiaxed α_p for the comparison with other structures with different α_p contents. It is a typical structure displaying high strength level but limited ductility, especially the water quenched condition β/ WQ. That is why these are not preferred for industrial applications (Fig.3.1.c).

β processed structures or Pancake structures (PC)

In order to achieve PC, the material was rolled at 970 ℃ (β phase field). The following recrystallization was performed at 920 ℃ (same to that of D10) to get a correspondent condition to D10 for further comparisons with respect to microstructural types and resultant mechanical properties (Fig.3.1.d).

b). TIMETAL-54M

The main procedures of TMP for TIMETAL-54M are similar to those of Ti-6246. A four-step TMP was used, including homogenization in β phase field (1050 ℃), hot rolling in (α + β) phase field (800 ℃) with deformation degree of $\varphi = 1.4$, recrystallization at three different temperatures and the final aging at 500 ℃ for 24 h. The use of aging temperature at 500 ℃ is to acquire optimum hardening effect via Ti_3Al (α_2) precipitation, besides the common α_s precipitation hardening. As the solvus of α_2 in Ti-64 is around 550 ℃, there should be no significant difference in the solvus considering the slight modification of the element composition in TIMETAL-54M relative to Ti-64. Aging treatment below the α_2 solvus could help precipitate α_2 particles. While aging above the solvus will be only a stress relief treatment. The details of three types of typical microstructures and relevant TMP would be illustrated respectively.

Fully equiaxed structures (EQ)

As indicated by the name, the microstructure mainly consists of equiaxed α_p, the maximum content that could be achieved. With the purpose of transforming most α phase into the form of α_p, the recrystallization temperature was set at 800 ℃, in the lower range of (α + β) phase field. Two kinds of cooling modes WQ and AC were used after the recrystallization. α_p will grow during the cooling process and no α lamellae are formed within the prior β grains, resulting in a fully equiaxed structure with the equilibrium volume fraction of β phase located at the 'triple-points' of α_p (Fig. 3.2.a).

Duplex structures with 15 % α_p within the (α + β) matrix (D15)

With the increase of the recrystallization temperature to 940 ℃, fine α_s precipitation would be enhanced as the α_p content drops to approximately 15 % (Fig. 3.2.b).

Fully lamellar structures (FL)

In fact FL of TIMETAL-54M is correspondent to the β annealed structure of Ti-6246. There are just different nomenclatures in different alloys. These were recrystallized at 1050 ℃ (50 ℃ above its T_β) to get fully β phase, and cooled down either by WQ or AC, corresponding to FL/ WQ and FL/ AC, respectively (Fig. 3.2.c).

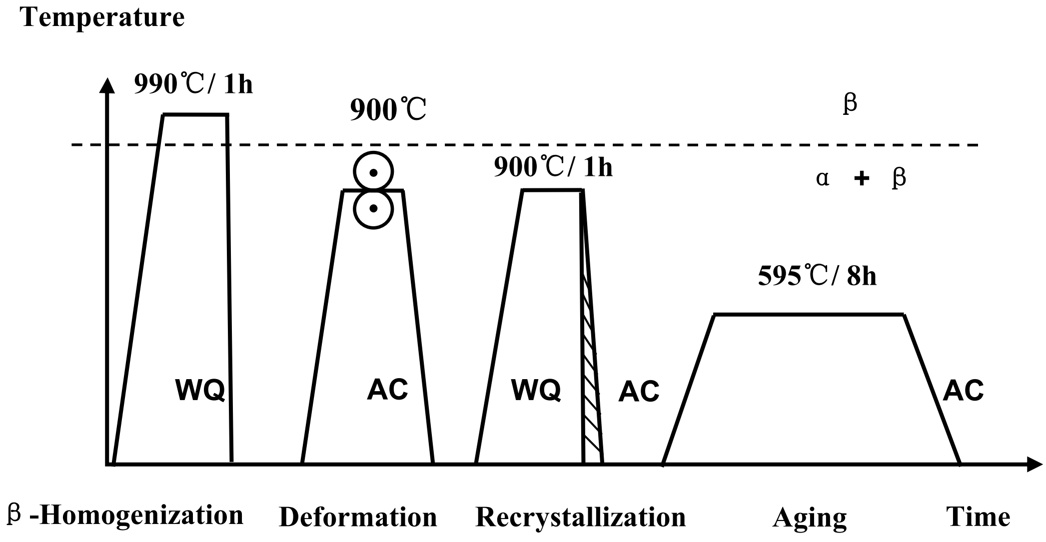

Figure 3.1.a TMP for Ti-6246 D30.

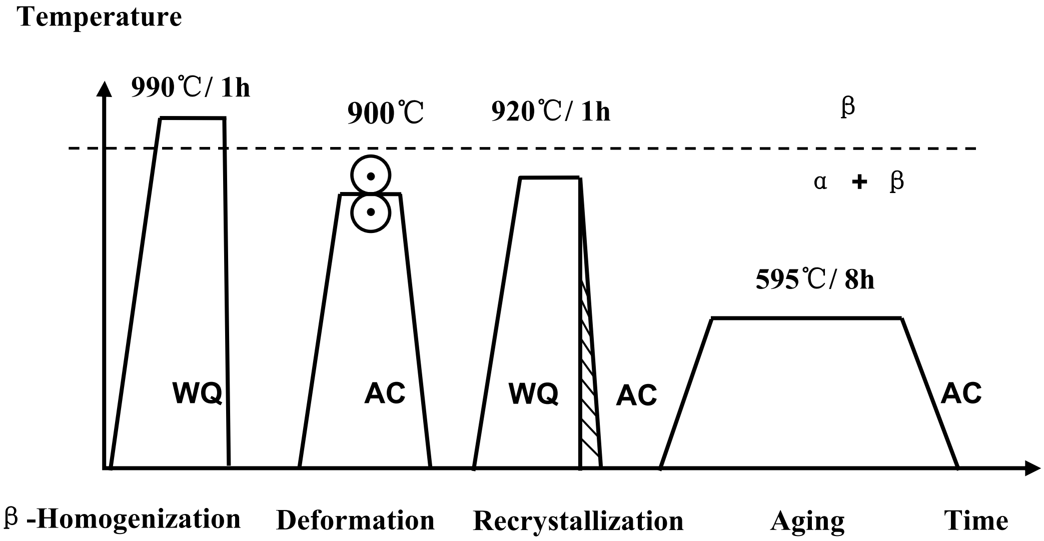

Figure 3.1.b TMP for Ti-6246 D10.

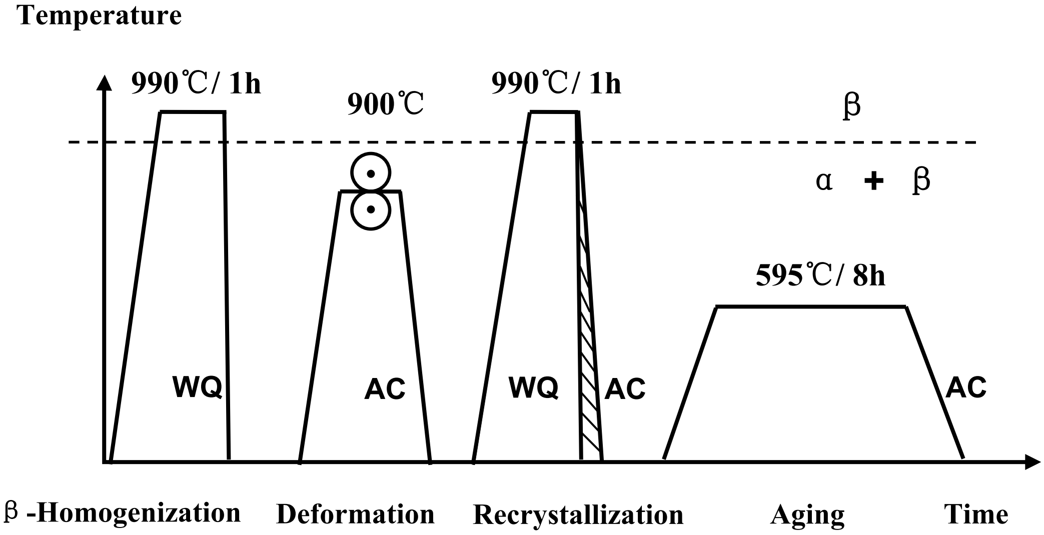

Figure 3.1.c TMP for Ti-6246 β annealed structures.

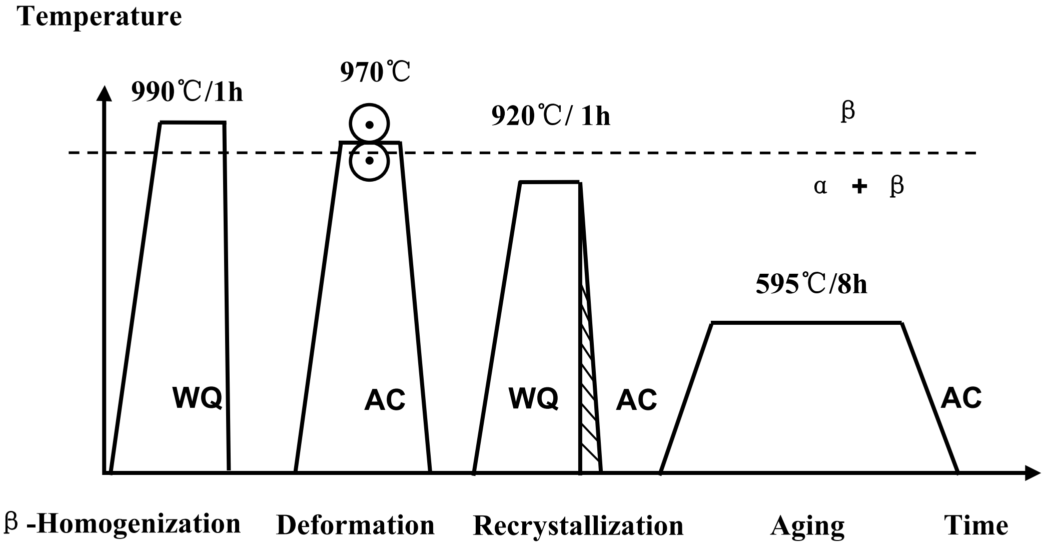

Figure 3.1.d TMP for Ti-6246 pancake structures.

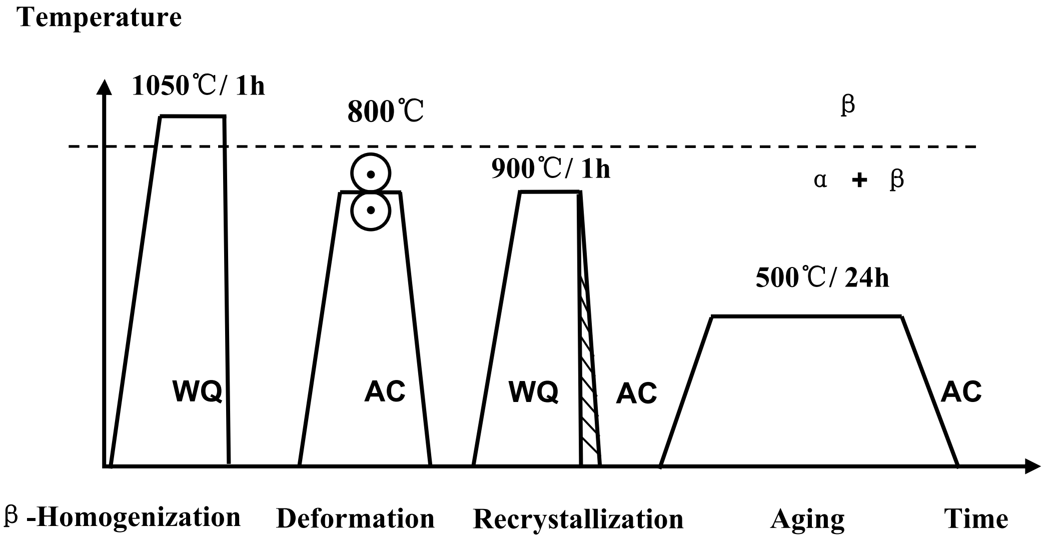

Figure 3.2.a TMP for TIMETAL-54M EQ.

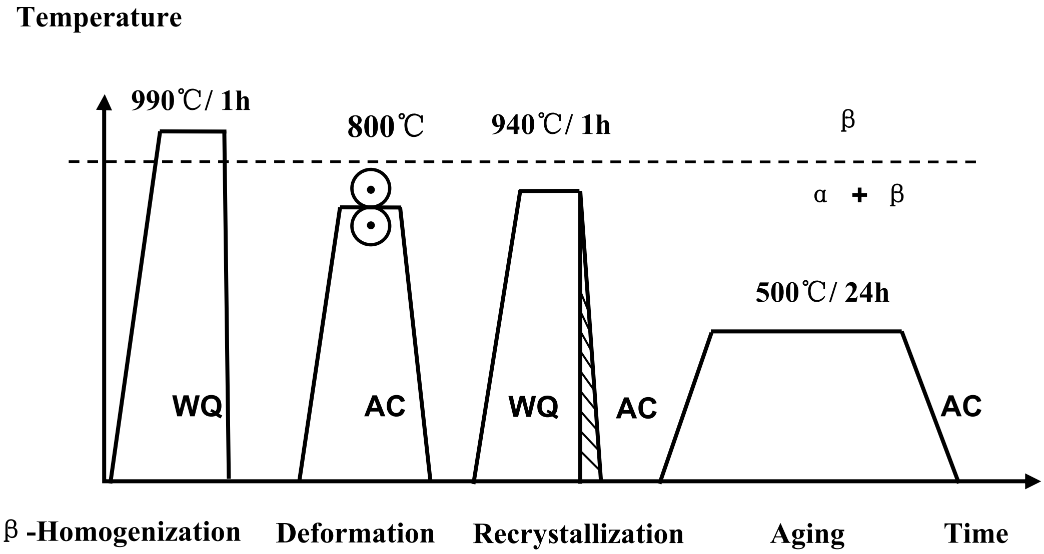

Figure 3.2.b TMP for TIMETAL-54M D15.

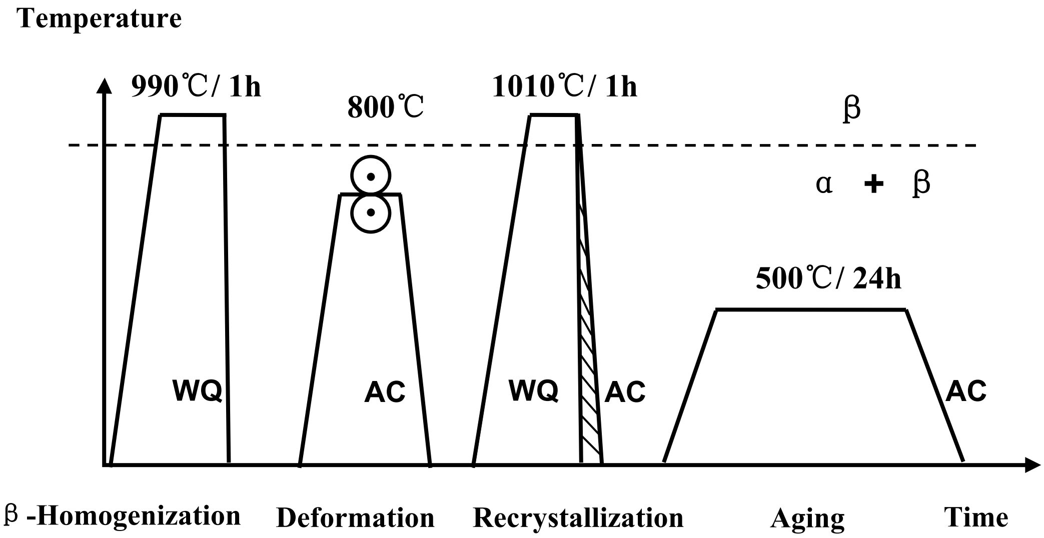

Figure 3.2.c TMP for TIMETAL-54M FL.

3.2.2 Shot peening

SP was carried out on a computer-controlled peening machine powered by compressed air (gravitation system), produced by OSK-Kiefer GmbH (Fig. 3.3.a). The shot media utilized in this study is spherically conditioned (rounded) cut wire shots (SCCW 14) with average size at 0.36 mm. SCCW shots possess spheroidal shapes with slight deviation because of the manufacturing process, showed in Fig. 3.3.b. The hardness of shots is around 700 HV. Shots were propelled by air blast system into the path of high pressure air and accelerated through a blasting nozzle which is directed at the specimen. Then each shot functions as a small ball-peen hammer, impinging the specimen surface. (Fig.3.3.c). A recycling system is operated to collect the blasted shots and refuel them back to the nozzle. As these cut wire shots could sustain long and be reused due to its conditioned roundness, unlike cast shot which tend to break into pieces that can damage the specimen surface.

The peening coverage is an important quality controlling parameter, exhibiting how completely the specimen surface has been peened by impinging shots. The factors influencing coverage include: number of impacts (shot flow), exposure time, shot properties and work piece properties. It was monitored by optical examination to determine the coverage. It was ascertained in pretesting that it takes at least 45 seconds to reach full coverage. So the peening duration is set up at 45 seconds to insure full coverage of all specimens. In the process, the distance between the nozzle and the rotating specimen was kept constant to control the uniform coverage of the specimen. The major parameters of peening setup are listed in Tab. 3.4. The key parameter to characterize the effect of SP is the peening intensity, which was gauged using Almen-stip A by determining the deformation of peened strip, i.e. the arch height of the bent strip. The corresponding Almen intensity achieved by the setups in the Tab. 3.4 was 0.22 mmA, which is moderate for Titanium alloys.

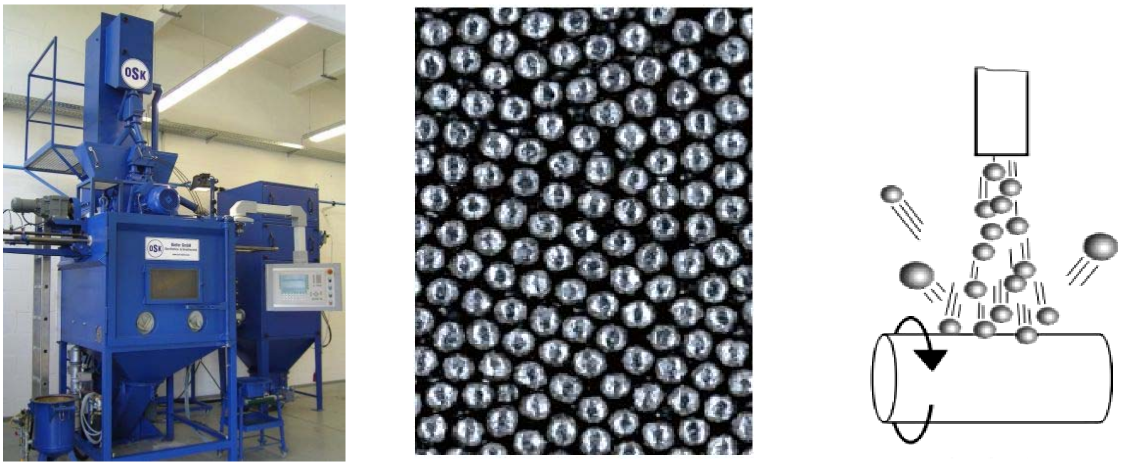

(a) (b) (c)

Figure 3.3 (a) Shot peening machine, (b) peening media SCCW, (c) peening process.

Table 3.4 Parameters of SP.

Peening media	Distance between nozzle and specimen	Specimen rotation	Peening pressure	Peening's time	Coverage	Almen Intensity
SCCW14	90 mm	0.5 /s	3.0 bar	45 s	100 %	0.22 mmA

3.3 Microstructure characterization

The specimen surfaces (9×9 mm^2) for microstructure examination were taken from the cross section of the thermo-mechanically treated specimens (9×9×60 mm^3) using SiC cutting wheel. The standard metallographical preparation was implemented to reveal the microstructures under optical microscope, including sectioning, mounting, grinding, polishing and etching. At first, two kinds of mounting methods were performed according to characters of microstructures. Aged specimens were supposed to be relatively stable, so it is possible to embed the probes into thermoplastic polymer at 180 ℃ without inducing changes in the phase constitutions and resultant microstructures. While for the unaged structures, cold mounting was preferred in order to avoid any possible influence of the heating process on microstructures during mounting. In details, mixed solution of 25 g epoxy resin and 5 g hardener was used to fix the specimens after 12 hours aging. Then Grinding was carried out manually on a series of SiC papers with different grits ranging from 500 to 2400, corresponding to particle diameters from 20 to 8 μm. Following polishing was done semi-automatically by Struers LaboForce machine. Specimens fixed in sample holder within the polisher were ground on rotating woven cloth plates and further polyester cloth using lubricants (e.g. soft soap) and diamond pastes having average grain sizes of 6, 3 μm sequentially. At last alkaline OP-S suspension with SiO_2 particles at the size of 1 μm was employed for the final polishing. Prior to etching, specimens were cleaned in ultrasonic bath for 30 seconds. Then the microstructures were revealed by etching the specimen surfaces with The Kroll's etchant which consists of 92 ml distilled water, 6 ml HNO_3 and 2 ml HF. The durations of immersing the studied probe into the etchant vary with respect to specific microstructures. Sufficient attention must be paid during the etching step in case the probes become over-etched. Afterwards, ultrasonic cleansing should be performed to peel off the etching resultants from the surface and fully disclose the microstructures beneath. Finally the etched probes were subjected to the observation under 'Axioplan 2' type optical microscope produced by Carl Zeiss AG. Micrographs were taken by suitable objectives with transmitted light to display the detailed features of the microstructures. Based on the micrographs, the area fractions of α_p were measured using automatic evaluation program within the facilities.

In order to exhibit the micro-textured zones i.e. macrozones, transmitted polarization light was also applied to determine the optical characteristics of the grains. Different colour contrast at specific phase components under the polarization light could demonstrate the variation of the crystallographic orientation.

3.4 Quantitative phase identification

Quantitative identification of phase constitutions were conducted using HESXD at beam line Petra III HEMS P07B station of German electron synchrotron center (HASYLAB/ DESY). High-energy synchrotron radiation was generated by forcing the fast moving high-energy electrons using undulators and/ or wigglers to travel along a curved path. Then the emitted high-energy radiation with relatively low wave length (X-ray) was further induced into measuring hutch as incident beam for diffraction analysis. The setup in the testing hutch was illustrated in Fig 3.4. The diffraction patterns (Debye-Scherrer rings) were detected with mar 345 image plate detector (CCD) with a maximum diameter of 345 mm. The photon energy applied was 87.3 keV, corresponding to a wave length of 0.142 Å. Diffraction tests with the beam size of 0.5×0.5 mm^2 over a rotating angle $\omega = 180°$ were done at least twice at different locations in each specimen ($4 \times 4 \times 20$ mm^3) to confirm the repeatability of the results. Twelve conditions of Ti-6246 were investigated, including all aged and unaged structures of β, D10 and PC. Noteworthy, a Ti-13 powder tube (purity: 99.9 %, grain size: 30 μm) was measured to gather the background and instrumental functions. The data interpretation was fulfilled using software FIT2D. Finally, quantitative phase analysis was done following Rietveld method with software Maud.

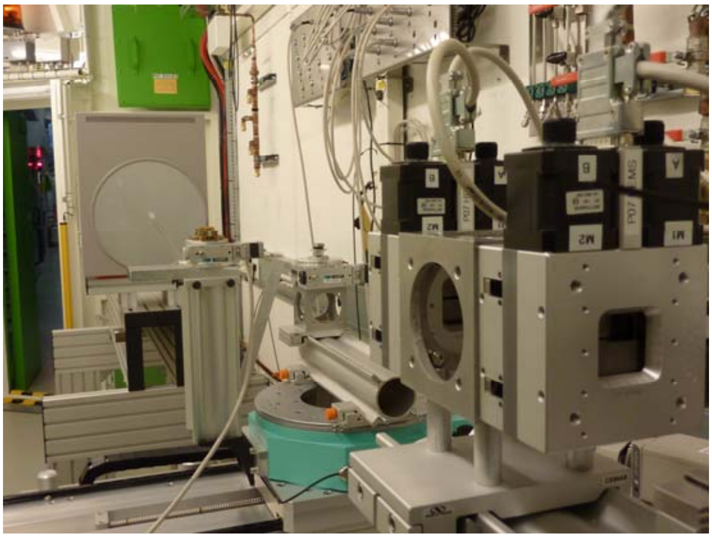

Figure 3.4 Setup of the phase measurement by HESXD in DESY.

3.5 Characterization of the surface layer

With the aim of improving the HCF performance SP was applied on the axial fatigue specimens. It leads to plastic deformation in near-surface regions which evidently affects the surface roughness and the dislocation density (degree of cold work). Owing to the local plastic deformation, macroscopic residual stresses are generated. Generally, SP modifies the surface properties in three aspects:

- surface roughness
- dislocation density (degree of cold work)
- residual stresses

The focus of this study is fatigue behaviour, as fatigue cracks usually nucleate at the surface in smooth-bar specimens, and the change in surface layer properties caused by mechanical surface treatments affects both the stage of crack nucleation at the surface and the initial surface crack growth or microcrack propagation. Therefore, characterizations on surface roughness were undertaken on both as peened and electrolytically polished flat specimens. Considering the later fatigue tests at elevated temperature, it is also necessary to identify the thermal stability of the cold work and residual stresses. Flat specimens will be first preheated in the fatigue furnace chamber to the testing temperature, cooled down in the air then measured again. The speculation about the cold work induced surface microstructure gradient at the testing temperature could not be ignored. Shot peened specimens which are then heat treated at elevated temperature for 60 h will be also subjected to metallographic examination.

3.5.1 Roughness

Profile roughness refers to the fine irregularities in the surface texture, usually including those resulting from production processes such as marks caused by machining or surface treatments, e.g. electro-polishing or SP. As the specimen surface finish plays an important role in fatigue crack initiation, it is very necessary to characterize the difference in roughness resulting from specific surface treatments. In this study roughness was measured by a stylus contact-type profilometer S8P produced by Perthen Mahr. The surfaces of the specimens are moved relative to the stylus. The height position of the stylus generates an analog signal which is converted to a digital signal stored, analyzed and displayed. This instrument provides graphs of surface topography and numerical indications of roughness in terms of R_a, R_{max} and R_z. R_a is the arithmetic average in the sampling span. R_{max} is the maximum peak-to-valley roughness height. R_z is the average distance between the five highest peaks and the five deepest valleys within the sampling length. That's also why it is called ten-point height. Every surface was measured three times to get mean values.

3.5.2 Microhardness-depth profile

Hardness is an important indication of a material's resistance to localized plastic deformation. Indentation hardness tests were used to demonstrate the hardness of materials, wherein a small indenter is forced into specimen surfaces, resulting in the formation of impressions or indentations. The depth or size of the indentation was a measure of the hardness index number. Microhardness obtained at lower indentation load is considered as a potent criterion to describe the local strength levels of the materials in microscopic scale.

Microhardness-depth profile was utilized to display the variation of cold work in the near surface region of the specimens treated in four conditions. The first is the as shot-peened (SP). Second is shot peened then preheated to 450 ℃ in 2.5 h then soaked for another 1.5 h using a three-heating stage furnace (Preheat), abbreviated as SP + Preheat. Following is the SP + Preheat specimens kept at 450 ℃ for another 1 h (SP + Preheat +450 ℃/1 h). At last SP + Preheat specimens kept at 450 ℃ for 55.6 h are also examined (SP + Preheat +450 ℃/55.6 h). With the above testing, the influence of SP on cold work and its thermal stability could be characterized. The affected zone by SP will be identified by depicting the microhardness-depth profile using Streuers Duramin microhardness tester. Vickers hardness tests (HV) were applied with a load of 981.2 mN (HV 0.1) in this study. A zigzag shaped route for microindentation was set up from the specimen surface to 1mm into the interior with a depth interval of 0.05 mm to attain a tendency profile of microhardness versus depth.

3.5.3 Residual stress

The residual stress vs. depth profile at the near surface region induced by SP in this study is measured by the hole-drilling strain-gage method. Namely, the test surface is bind hole drilled. The relaxation of the residual stress due to the material removal results in responsible change in strain, which could be detected by the strain sensors attached on the test surface. The principal stresses are calculated by measured strains through a series of equations using the Young's modulus and Poisson's ratio. Residual stress depth profiles of Ti-6246 after SP, SP + Preheat, SP + Preheat + 450 ℃/1 h and SP + Preheat +450 ℃/55.6 h were characterized. The setup of the residual stress measurement was illustrated in Fig 3.5. The measurement procedures standardized in ASTM E837 could be briefly summarized as the following steps:

- A three element strain gage rosette produced by Company Vishay is installed on the shot peened specimen surface (20×20 mm^2)
- The gage grids are wired and connected to a multi-channel static strain indicator Micromeasurements Model P3
- A precise drilling set is adjusted perpendicular to the specimen surface and accurately centred over a drilling target on the rosette.
- After calibration and zero-balancing the gage response, a small shallow hole with a diameter of 1.9 mm is drilled through the geometrical center of the rosette into the material. The drilling process proceeds with a depth increment of 0.02 mm, reaching 1.00 mm beneath the surface.
- Response of the relaxed strains at each depth of increment was acquired.
- According to special data-reduction relationships, the principal residual stress and the angular orientation are calculated from the measured strains.

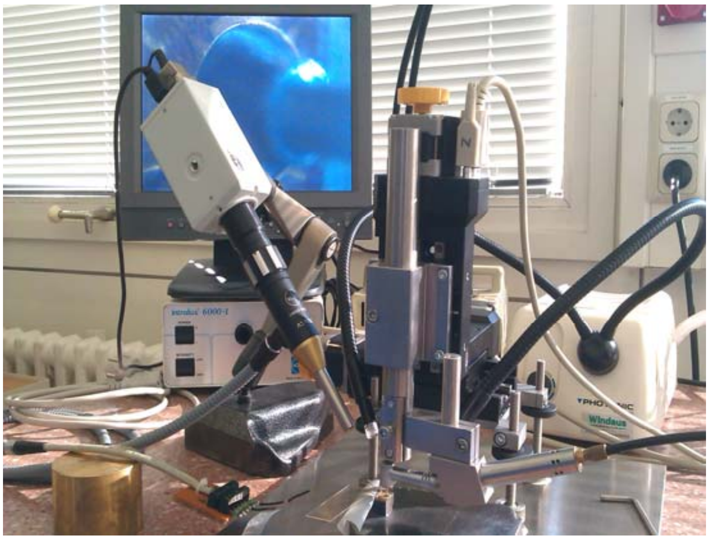

Figure 3.5 Experimental setup for residual strain measurement.

3.6 Examination of mechanical properties

3.6.1 Tensile test

All tensile specimens were turnd from the aged materials with the loading direction aligned to the transverse direction with respect to the rolling process. Tensile tests for both alloys were performed at room temperature (RT). Since Ti-6246 is especially designed for components applied at intermediate temperature up to 450 ℃, it is necessary to achieve the tensile behaviour of the alloy at 450 ℃. All tensile specimens share the same geometry (DIN 50125) with gauge lengths and diameters of 25 and 5 mm, respectively (Fig.3.6). Two specimens were tested for each condition to get a mean value. Tests at RT were carried out on Instron 5582 universal testing machine at the load of 50 kN, with straining speed of 1 mm/ min. Young’s moduli were measured by a strain gauge attached to the gauge lengths of the specimens. While Instron 4507 universal machine equipped with two-heating stage oven was utilized for the tests at 450 ℃. All specimens were first heat up to 450 ℃ within two hours, and then soaked for an hour to minimize the temperature gradient before starting the tests. The following tensile properties were examined (Due to the lack of strain gauge at elevated temperature, the Young's moduli of the specimens at 450 ℃ were missing).

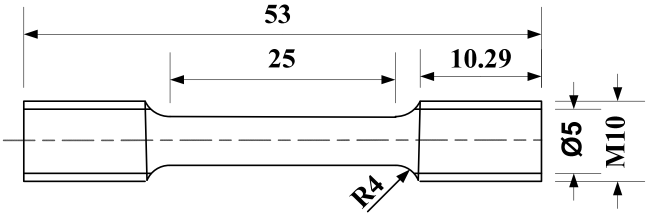

Figure 3.6: Geometry of tensile specimen.

E		[GPa]	Young's modulus
$\sigma_{0.2}$ (YS)	$= F_{0.2}/A_0$	[MPa]	Yield stress
σ_{max} (UTS)	$= F_{max}/A_0$	[MPa]	Ultimate tensile strength
EL	$= (L_F - L_0)/L_0 \times 100\%$	[%]	Fracture elongation
RA	$= (A_0 - A_F)/A_0 \times 100\%$	[%]	Reduction of area
ε_F	$= \ln(A_0/A_F)$		True fracture strain

3.6.2 High cycle fatigue test

In order to characterize the impacts of microstructure, loading mode, mean stress, environment and surface treatment a series of HCF tests regarding specific key parameters were organized.

At first, the microstructural optimization considering the content of α_p were implemented at rotary bending load (load ratio R = -1) on Rolls Royce rotating-beam fatigue machines at the frequency of 50 Hz at room temperature in laboratory air. For Ti-6246, β annealed, D10 and D30 were tested for comparison. In the case of TIMETAL-54M, FL, D15 and EQ were examined. The hourglass shaped specimens (Fig. 3.7.a) were used. Consequently, the optimal microstructures regarding HCF being characterized would be applied in the following fatigue investigations.

To elucidate the effect of loading mode on HCF behaviour, axial fatigue tests for both alloys at RT were carried out at R = -1 using threaded axial fatigue specimens (Fig. 3.7.b) on a power swing 100 resonance machine from by SincoTec Test Systems GmbH, as shown in Fig. 3.8.a. With the comparison between the HCF at axial load and rotary bending load, the impact of loading mode could be gathered.

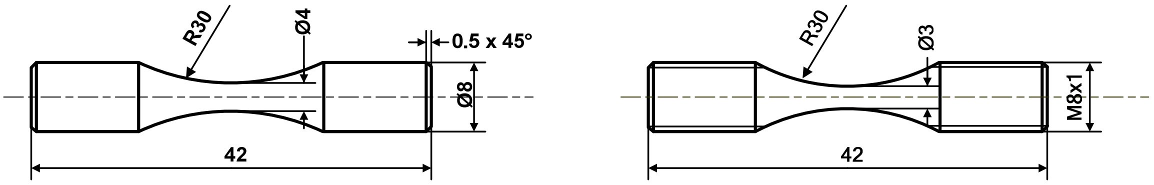

(a) Geometry of R-B fatigue specimens (b) Geometry of axial fatigue specimens

Figure 3.7 Geometry of different fatigue specimens.

Mean stress effect was revealed by displaying HCF at different load ratios. In this study axial fatigue tests on the two alloys at R = 0.1 were also done. For the test at RT, the above mentioned Resonance machine was utilized. Mean stress effect at elevated temperature for Ti-6246 can not be neglected, owing to its major application. Due to the concern about the impact of environment such as elevated temperature, axial fatigue tests at 450 ℃ were fulfilled at both R = -1 and 0.1 on an Instron 8801 Servohydraulic machine (Fig.3.8.b) which is facilitated with a three-heating stage furnace. The load alternating frequency was set at 50Hz.

Considering another important environmental element, atmosphere, HCF in vacuum condition was also examined at R = -1 on the resonance fatigue machine. The vacuum in the hermetical chamber was kept lower than 1×10^{-5} mbar during the tests.

(a) Power swing 100 resonance machine (b) Instron 8801 servohydraulic machine

Figure 3.8 Two types of axial fatigue machines

In order to exclude the machining effects on fatigue properties, before testing, all the specimen were first ground off about 100 μm by a series of SiC papers with grits ranging from 500~2400, then electrolytically polished for another 100 µm in a mixed solution of 290 ml Methanol and 180 ml 1-Butanol and 30 ml Perchloric acid. According to practical experience, the optimal polishing temperatures for Ti-6246 and TIMETAL-54M were around -30 and -20 ℃, respectively, by which a very smooth surface finish and processing efficiency could be achieved.

The effect of SP on HCF at both RT and 450 ℃ was characterized using peened axial fatigue specimens at R = -1 on the hydraulic fatigue machine. All the tests at 450 ℃ were started after preheat to eliminate the temperature gradient.

3.7 Fractographic study on fatigued specimens

All the fatigued specimens were first examined using digital camera for preliminary selection. Specimens with specific features were selected for profound investigation using scanning electron microscopy (SEM).

SEM is a type of electron microscope that generates images of specimens by scanning them with a focused beam of electrons. As incident electrons interact with atoms of the specimen surface, various signals could be produced, including secondary electrons, back-scattered electrons, characteristic X-rays, transmitted electrons et al. It is rare to detect all the possible signals within a single machine. The most common mode of detection is by secondary electrons emitted by atoms excited by the incident electrons. The intensity of the secondary electrons received by the detector is a function of the tilting angel of the surface. By scanning the sample and detecting secondary electrons, the topography with resolution up to the scale of 1 nm could be imaged. Besides, the signals of characteristic X-ray are also widely applied within SEM, as energy-dispersive X-ray spectroscopy (EDX). The incident beam may excite and eject an electron in an inner shell (low-energy shell), leaving an electron hole. An electron from an outer, higher-energy shell then fills the vacancy, while with emitting X-ray with wave length characteristic of different atomic structures. By means of this the element composition of the specimens could be measured. Both secondary electrons and EDX detection were employed in this study to reveal the local microstructures and element constitutions.

4. Experimental results and discussion

4.1 Microstructures

In this session microstructural analysis of various conditions of both Ti-6246 and TIMETAL-54M will be presented. For Ti-6246, alloy classification is one of the important issues that should be identified, detailed characterization of the microstructures appeared during the TMP will be carried out, especially concerning the cooling rate. Based on the results of optical microscope, the influence of TMP on microstructural evolution will be elucidated with emphasis on Ti-6246.

4.1.1 Microstructures in as-received conditions

A typical β-forged microstructure is observed in the as-received forged disks of T-6246, shown in Fig. 4.1.a. The obvious prior β grains exhibit morphology similar to pancakes with long dimensions (ranging 300~500 μm) aligning along the radial direction of the disks. Due to this similarity, β-forged microstructure is usually termed pancake structure (PC). More details of the PC could be found from the Fig. 4.1.b with higher magnification. The bulk comprises of a matrix of the basket-weave shaped (α + β) lamellae and the unevenly distributed equiaxed α_p with diameter around 10 μm. Unlike the continuous grain boundaries α (GB α) in common (α + β) Ti alloys such as Ti-64, the GB α in Ti-6246 is semi-continuous. Generally the microstructural configuration of the as-received condition is quite inhomogeneous. That is also one of the reasons to develop better defined microstructures using TMP.

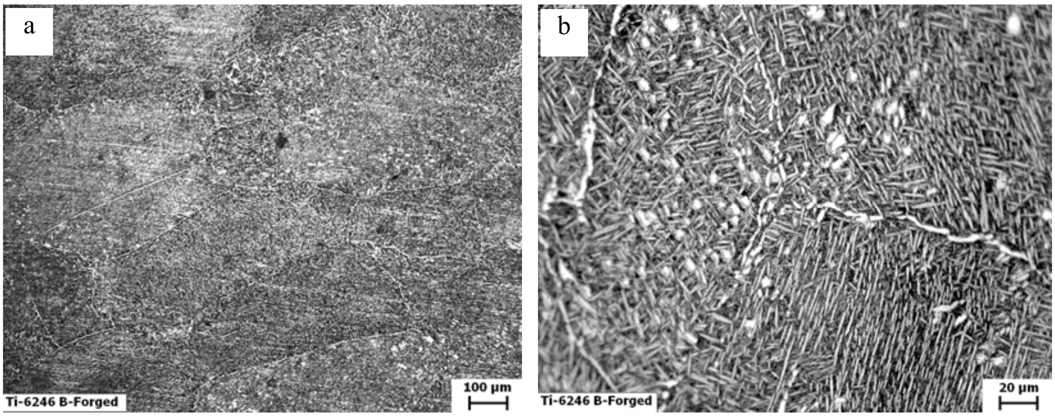

Figure 4.1 Micrographs of as-received Ti-6246.

Corresponding to the mill annealing process at lower level of (α + β) field before delivery, the micrograph of the as-received TIMETAL-54M (Fig. 4.2) reveals a duplex structure with high α_p area fraction up to 40 %. The grain size of is in the range of 15~20 μm.

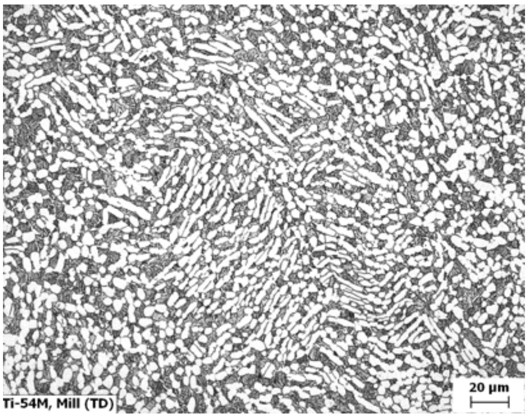

Figure 4.2 Micrograph of as-received TIMETAL-54M.

4.1.2 Effect of rolling temperature

During unidirectional rolling of Ti-6246, both 900 and 970 ℃ were applied for annealing the specimens in (α + β) and β phase field, respectively, to develop the duplex and pancake structures. The micrographs in Fig. 4.3 taken from the transverse direction of the specimen plate rolled at 900 ℃ exhibit a duplex structure with approximately 35 % α_p in a slightly prolonged nodular shape. In comparison with the as-received material (Fig. 4.1.b), microstructure is refined after rolling with a deformation degree φ of 1.4. Although GB α disappears, the prior β domains or macrozones in pancake shape remain, which are well presented in Fig. 4.3.a. It is noticeable that the previous (α + β) lamellar matrix is replaced by fine grains (Fig. 4.3.b). The hot rolling leaves a legacy in the microstructure as both macrozones and α_p have their long axis along the rolling direction which corresponds to the direction of material flow.

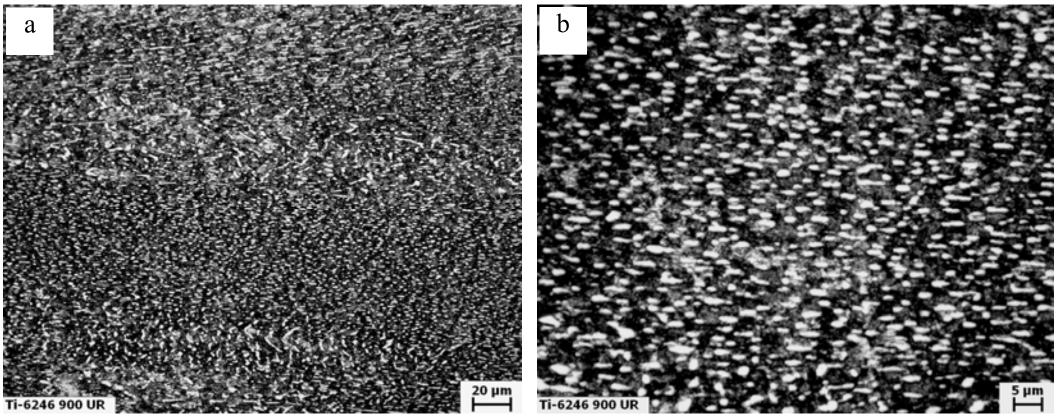

Figure 4.3 Micrographs of the material rolled at 900 ℃.

Fig. 4.4 shows the micrographs of the material rolled at 970 ℃, which is termed PC due to the shape of long and flat prior β grains surrounded by semi-continuous GB α. The long dimension of prior β grains is aligned with the rolling direction, same as that in material rolled 900 ℃ (Fig. 4.3), consistent with the material flow. 6 % α_p grains are present in the material in a plate shape instead of equaixed shape. Although the annealing is performed in β phase field, β annealed structure is not expected because of the drop of temperature during rolling process.

Comparing Fig. 4.3 and Fig. 4.4, it can be concluded that rolling temperature determines the structure type of materials, i.e. morphology of prior β zones, shape and fraction of α_p.

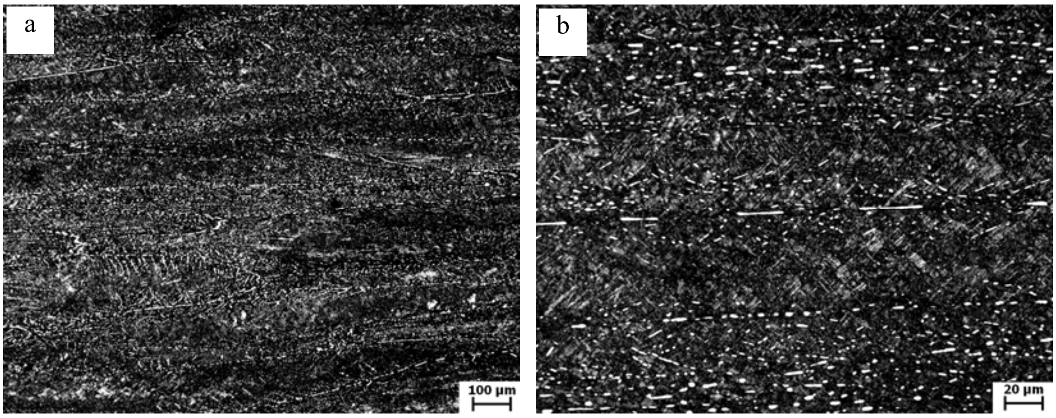

Figure 4.4 Micrographs of the material rolled at 970 ℃.

4.1.3 Effect of recrystallization temperature

The final aimed microstructures for later fatigue tests were compared to reveal the effect of the recrystallization temperature considering both Ti-6246 and TIMETAL-54M. For (α + β) rolled Ti-6246, three groups of recrystallization at 900, 920 and 990℃ were conducted on the material, respectively, followed by WQ and AC. The specimens were aged at 595 ℃ for 8 h. In spite of the difference in cooling rates, microstructures recrystallized at the same temperatures are similar each other after aging.

Micrographs of annealed specimens at 900 ℃ in Fig. 5.5.a and b reveal duplex structures consisting of approximately 30 % α_p embedded in fine particulate matrix (D30). In comparison with the as-rolled structure (Fig 4.3), it could be noticed that both grain growth and rounding occur. The previous prolonged α_p nodules change into equiaxed shape at the size about 3 μm. While slight agglomeration of α_p is observed, which might contribute to an effect of the grain size enlargement. Although the rolling was also at 900 ℃, the slightly variation in the α_p area fractions could be explained by the drop of temperature during rolling out of the furnace.

With the increase of the temperature to 920 ℃, the duplex structures remain. Meanwhile α_p fractions decrease to around 10 %. Appropriate resolutions of the micrographs offer a clearer insight. D10/ WQ (Fig. 4.5.c) shows a almost indiscernible structure in matrix, which is even finer than the particulate matrix in D10/ AC (Fig. 4.5.d). The lower α_p fractions lead to more discrete distribution of α_p, correspondently less grain agglomeration. The grain size is under 3 μm. Fig. 4.5.e is a demonstration of the retained pancake shaped prior β domains (macrozones) in D10/AC, although GB α is absent from the same location (Fig. 4.5.f).

For specimens recrystallized at 990 ℃, structures shown in Fig. 4.5.g and h comprise of fine needle-like α_s lamellae with width under 1μm. These are so-called β annealed structures, which are much finer than those fully lamellar ones in other (α + β) Ti alloys such as Ti-64. The prior β grains are ranging from 150 to 500 μm, with very fine GB. The slight difference between β/ WQ and β/ AC lies in the α_s concentration along the GB. Obviously, α_s precipitation along GB in β/ WQ is much denser than that in β/ AC. The existence of α_s precipitation and even denser distribution along GB is contrary to the findings of precipitation free zones in T. Krull's work [82].

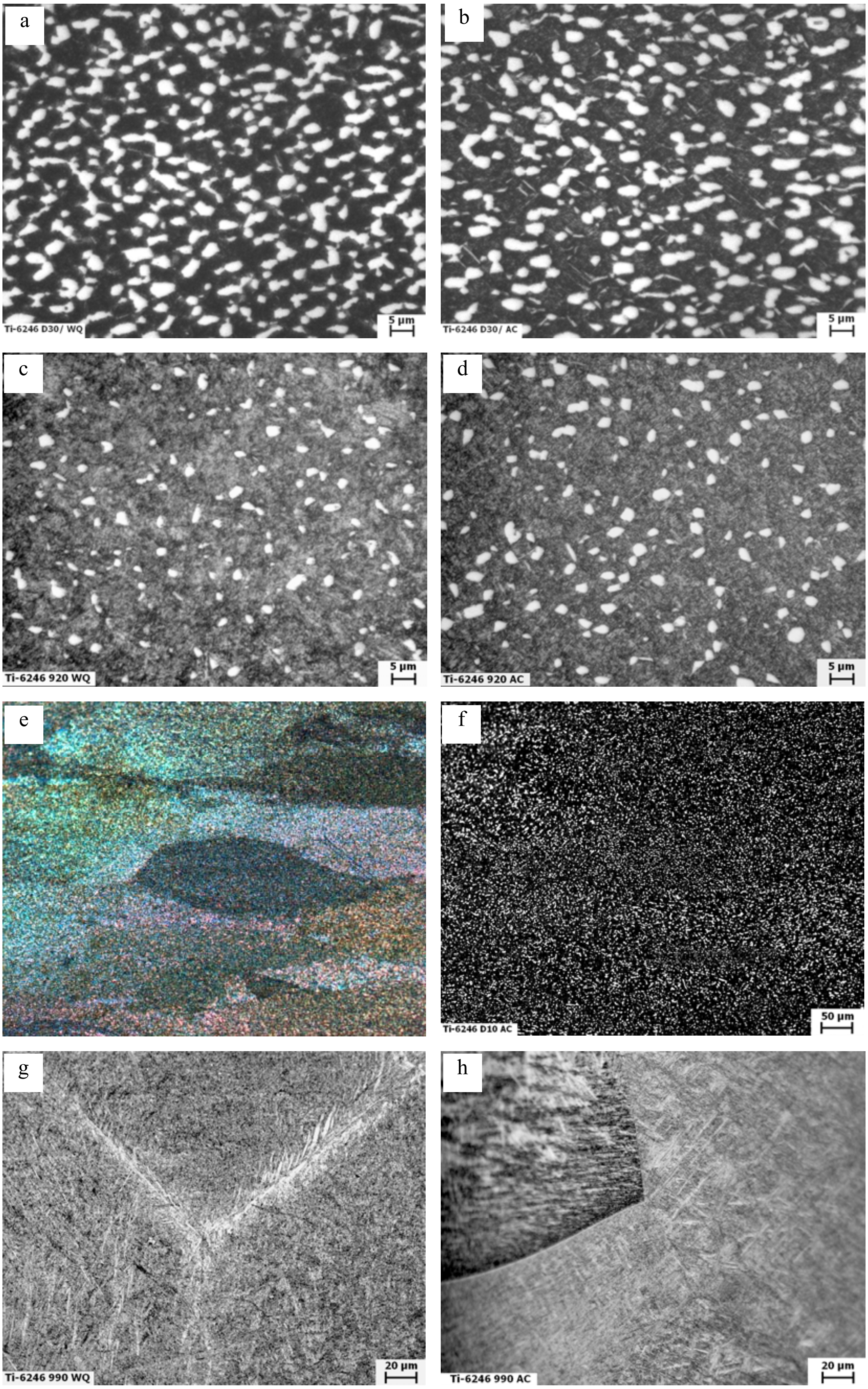

Figure 4.5 Microstructures of Ti-6246 aged specimens: (a) D30/ WQ, (b) D30/ AC, (c) D10/ WQ, (d) D10/ AC, (e) D10/ AC under polarized light, (f) location in (e), (g) β/ WQ, (h) β/ AC.

For β rolled (at 990 ℃) Ti-6246, a group of 920 ℃ recrystallized specimens reveal PC structures (Fig. 4.6). No much difference could be observed between the water quenched (PC/ WQ) and air cooled (PC/ AC). About 17 % lamellar shaped α_p with width at 1~2 μm is distributed in matrix possessing fairly indiscernible fine structures. Meanwhile a small portion of α_p turns out to be equiaxed, lying either along GB α or as GB α itself. Compared to the as-received condition in Fig. 4.1, the inhomogeneity is greatly reduced. The semi-continuous GB α remains, but are thicker in width (around 5 μm). This is presumably due to a grain growth process. The pancake-shaped prior β grains lie with long dimensions in the rolling direction. Under polarized light, an example of the prior β macrozone in the PC/ AC is convincingly exhibited in Fig. 4.6.c.

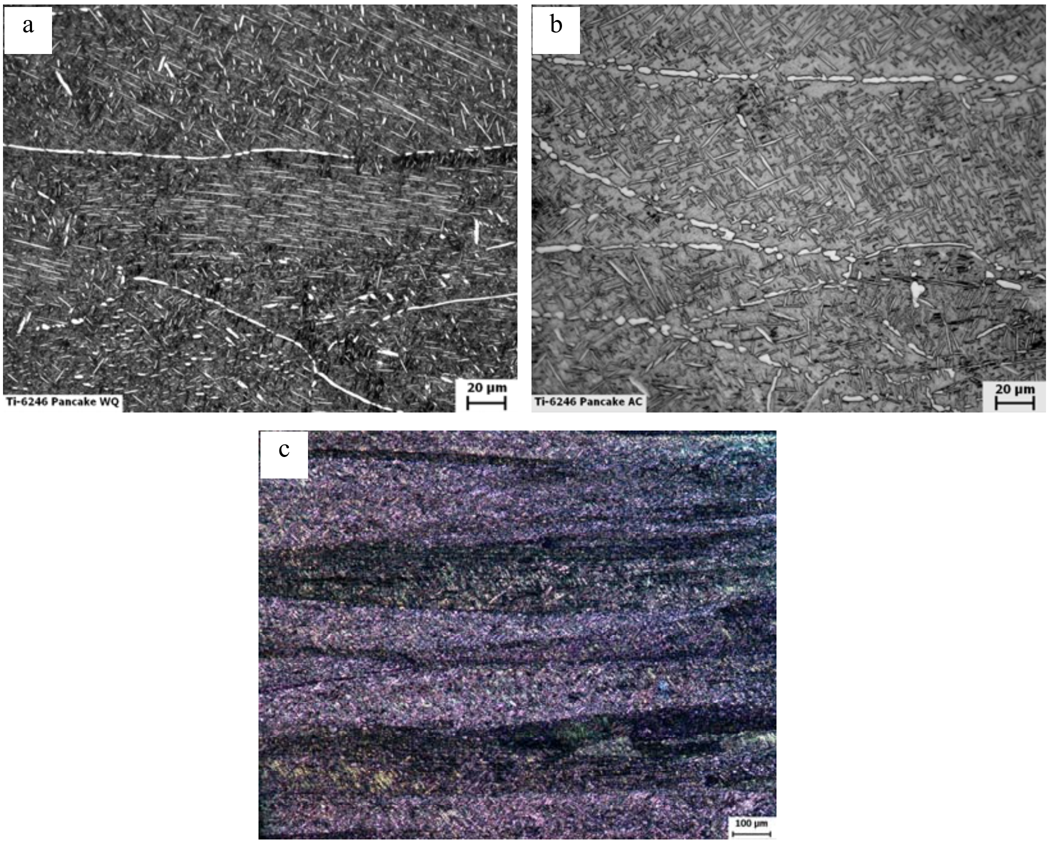

Figure 4.6 Microstructures of Ti-6246 aged specimens: (a) PC/ WQ, (b) PC/ AC, (c) PC/ AC under polarized light.

TIMETAL-54M was recrystallized at 800, 940 and 1010 ℃, respectively. Both WQ and AC were used to cool the specimens down from recrystallization temperature. Following aging was done at 500 ℃ for 24 h. Micrographs of recrystallized specimens at 800 ℃ reveal fine EQ structures. There is no much difference between EQ/ WQ (Fig. 4.7.a) and EQ/ AC (Fig. 4.7.b). Duplex with around 15 % α_p at the size of 6 μm and lamellar matrix were achieved in the specimens recrystallized at 940 ℃. The influence of cooling rate is displayed in the morphology of the matrix. Water quenched condition (D15/ WQ) shown in Fig. 4.7.c has lamellae with width under 1 μm, finer than that of air cooled (D15/ AC, Fig. 4.7.d). Similar difference was exhibited in the fully lamellar structures generated at 1010 ℃ (Fig. 4.7.e and f). As a variation of Ti-6Al-4V, TIMETAL-54 is a common (α + β) Ti alloy. WQ causes the β-matrix to undergo martensitic phase transformation while AC leads to a fully lamellar matrix due to a nucleation and growth process.

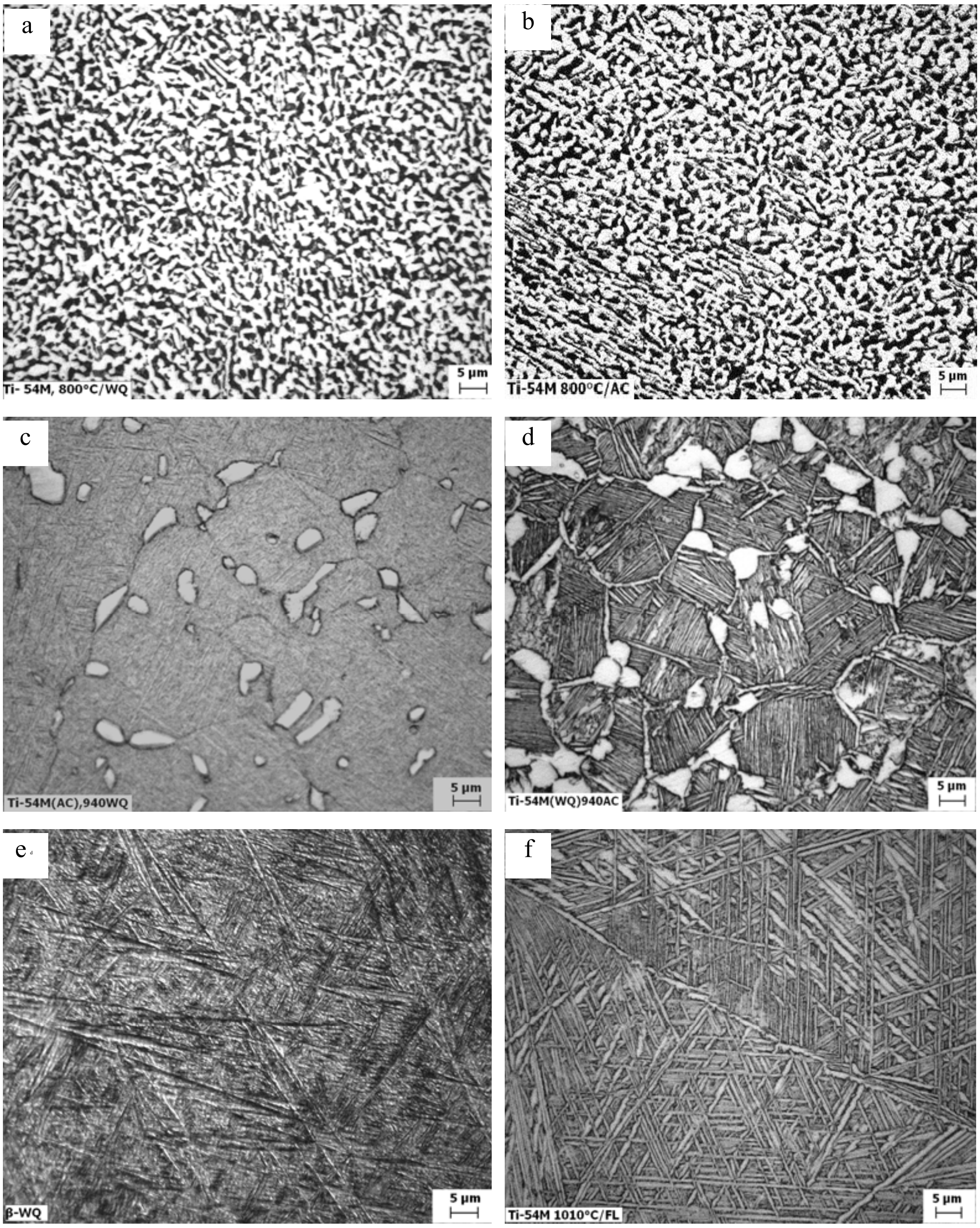

Figure 4.7 Microstructures of TIMETAL-54M aged specimens: (a) EQ/ WQ, (b) EQ/ AC, (c) D15/ WQ, (d) D15/ AC, (e) FL/ WQ, (f) FL/ AC.

4.1.4 Effect of cooling rate from recrystallization

As the influence of cooling rate on the microstructures of Ti-6246 could not be evidently demonstrated in the final aged conditions, unaged D10, PC and β annealed specimens were selected for comparison. Both D10/ WQ and PC/ WQ unaged (Fig. 4.8.a and c) exhibit indiscernible structure as matrix, different from the correspondent aged ones (Fig. 4.8.b and d) which consists of fine particulates. The micrograph of β/ WQ shows lath morphology similar to the martensite observed by S. Bein [6]. In contrast β/ AC (Fig. 3. b) consists of very fine lamellae. So it is clear that WQ brings out significant difference in microstructural components which might suggest variation in phase constitutions.

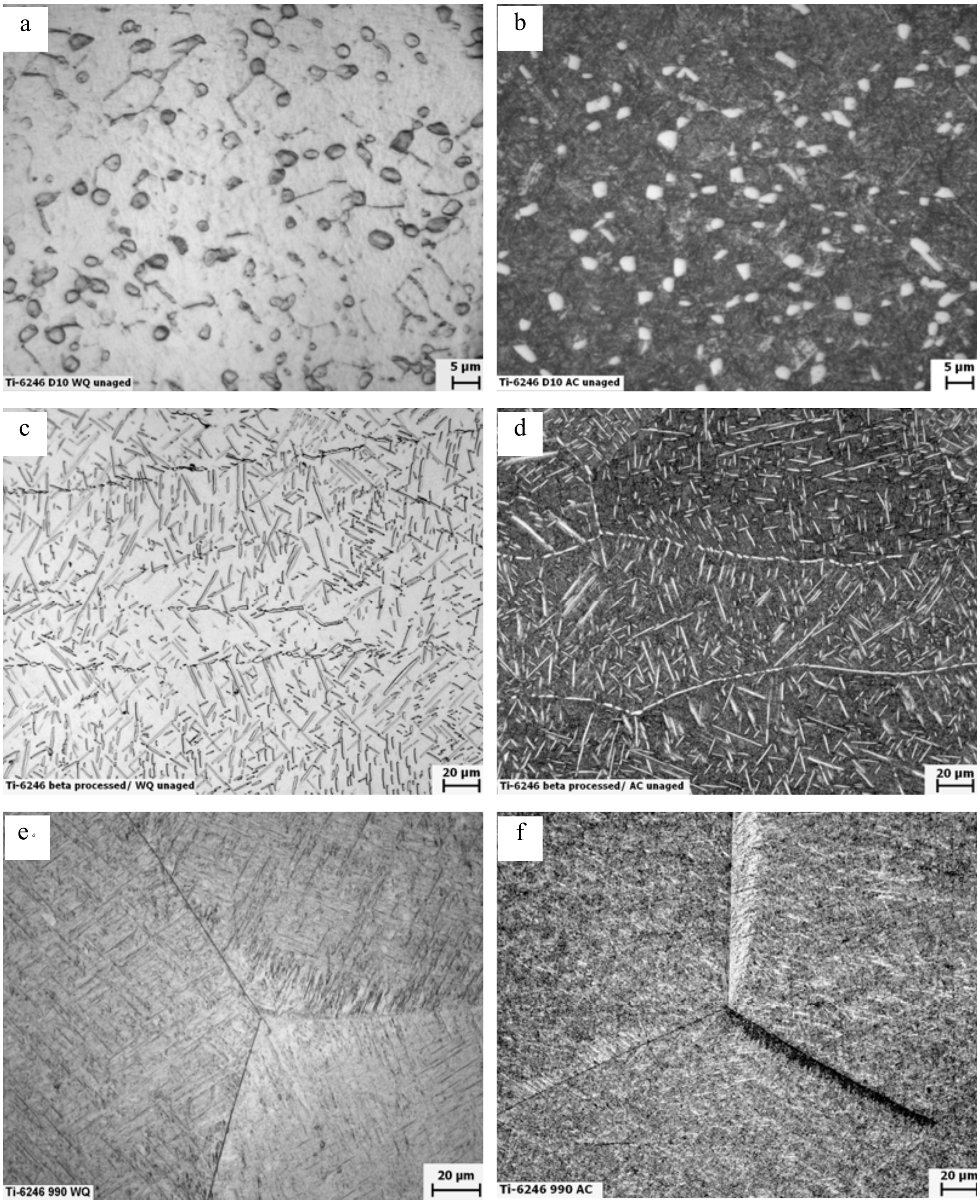

Figure 4.8 Microstructures of Ti-6246 unaged specimens: (a) D10/ WQ, (b) D10/ AC, (c) PC/ WQ, (d) PC/ AC, (e) β/ WQ, (f) β/ AC.

4.1.5 Effect of aging

Comparing Fig. 4.5 and Fig. 4.8, it is not difficult to recognize that aging results in the elimination of the change of microstructures deriving from different cooling rates. The indiscernible microstructure components in the water quenched conditions finally turn into the ones similar to the air cooled.

4.2 Phase constitution

4.2.1 Effect of cooling rate

Following the unfolded effect of both fast cooling from recrystallization and aging, the supposed variation in phase compositions could be identified through HESXRD.

The refined diffraction patterns of the unaged β/ WQ and D10/ WQ presented in Fig. 4.9.a and c, respectively, exhibit evident α″, characteristic of the 5 major peaks ranging from 3.0 to 4.0°. These easily differentiate α″ from the combination of (α + β), as appeared in the unaged β/ AC and D10/ AC (Fig. 4.9.b and d). β/ WQ unaged is composed of pure α″, indicating that the full β achieved during recrystallization at 990 ℃ thoroughly turns into α″ during WQ ($\beta \rightarrow \alpha''$). β/ AC unaged is made up of 37.5 wt. % β and 62.5 wt. % lamellar shaped α_s, which is precipitated through a transformation $\beta \rightarrow \alpha_s$ during AC. The different constitutions resulting from cooling rate correspond to the variation in the hardness described above. Hence it could be ascertained that WQ does induce martensitic transformation in Ti-6246. It should be reasonably classified as an (α + β) alloy.

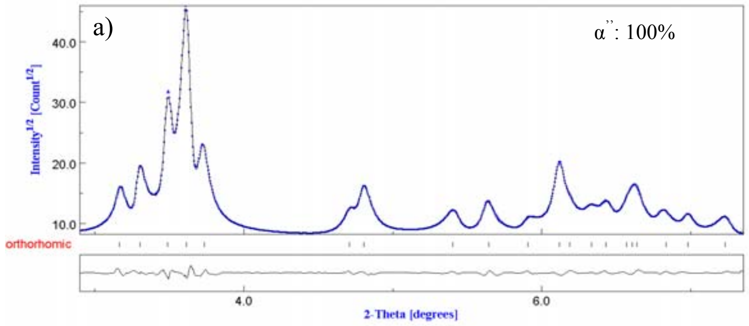

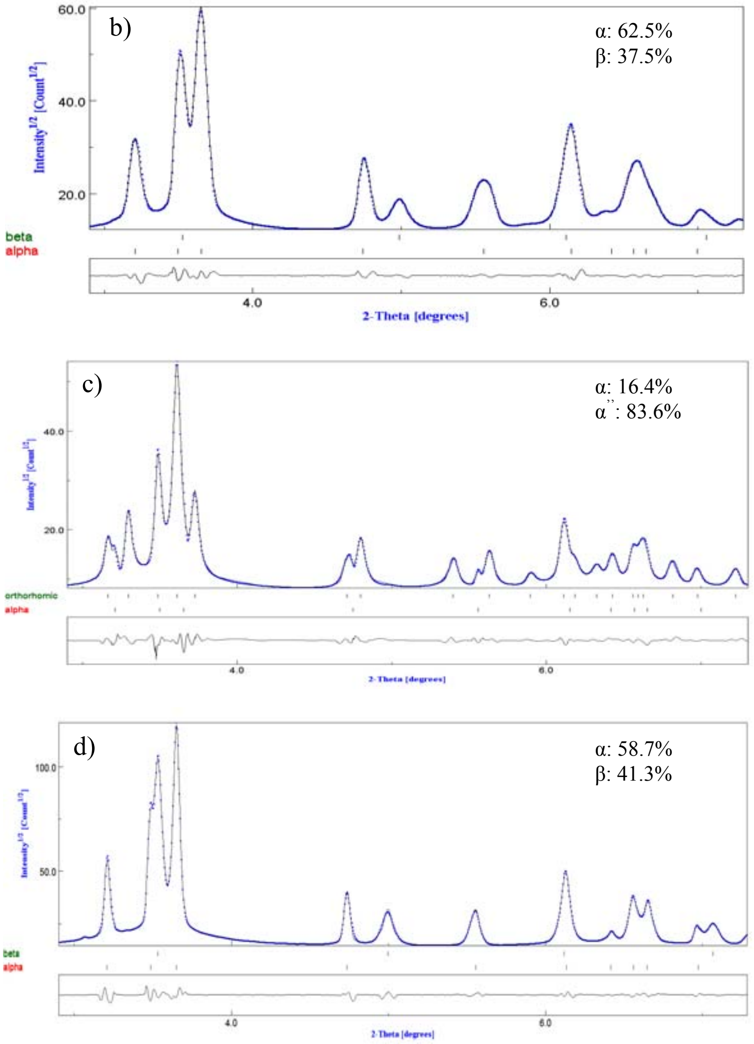

Figure 4.9 Refined diffraction patterns and phase contents of the unaged conditions: (a) β/ WQ, (b) β/ AC, (c) D10/ WQ and (d) D10/ AC.

4.2.2 Effect of recrystallization temperature

While with the decrease in recrystallization temperature to 920 ℃, α turns up in D10/ WQ unaged (Fig. 4. 9.c). Most of the characteristic α peaks are completely overlapped with those of α″, except for two discernible ones at 3.20 and 5.56°. In order to specify the weak diffraction pattern of α, parts of the Debye-Scherrer Rings of the both directly water quenched conditions in the range of 3.0 ~ 4.0° are illustrated. In comparison with the β/ WQ unaged (Fig. 4.10.a), it is obvious that the inner ring of D10/ WQ unaged (Fig. 4.10.b) is actually made up of two close ones, corresponding to the (110) of α″ and (100) of α from interior to outer, respectively, although the two peaks seem still partially overlapped with each other in Fig. 4.9.c. Quantitative phase analysis demonstrates 16.4 % α within the rest α″ in D10/ WQ unaged. As the recrystallization temperature maintains in (α + β) field, α_p forms in the β matrix first. With the instant quenching in water, the β matrix transforms into α'' completely, accounting for the rest 83.6 wt. % components as the indiscernible matrix in Fig. 5.8.a. With respect to D10/ AC (Fig. 4.9.d), besides β, much more α could be obtained, mounting to 58.7 wt. %. Since the contents of α_p should be consistent, the extra 42.3 wt. % compared to D10/ WQ unaged could be attributed to α_s precipitated from β during AC, which displays a fine particulate morphology in the matrix (Fig. 4.8.b). Based on its higher hardness in contrast to D10/ WQ, it could be concluded that α_s precipitation could lead to much more prominent hardening effect than martensitic transformation.

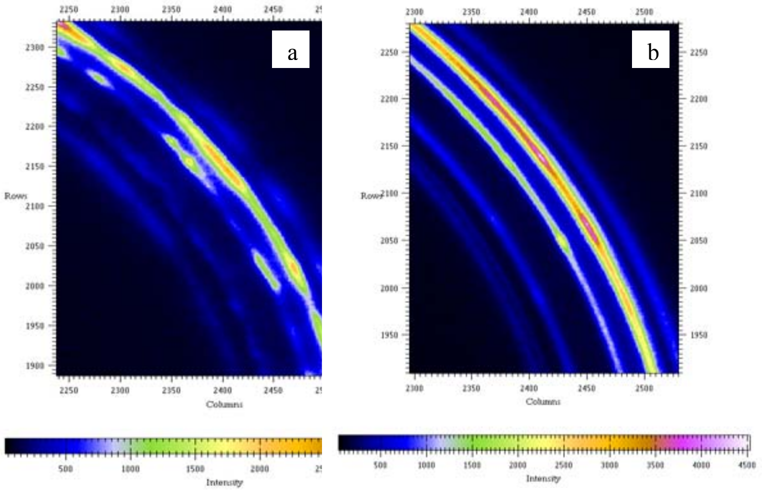

Figure 4.10 Parts of the Debye-Scherrer rings: (a) β/ WQ unaged, (b) D10/ WQ unaged.

4.2.3 Effect of aging

However, α'' achieved by WQ is proved to be metastable. After aging at 595 ℃ for 8 h, α'' in D10/ WQ (Fig. 4.11.a) disappeared completely, while with the occurrence of 22.2 wt. % β and a dramatic increase in α to 77.8 wt. %. The promotion in α fraction by 61.4 wt. % could be only owing to the α_s formation as the generation of α_p merely occurs during recrystallization. This suggests that aging results to the decomposition of α'' into α_s and β ($\alpha'' \rightarrow \alpha_s + \beta$). Considering the change in microstructures, the fine particulate matrix in Fig. 5.5.c should be a mixture of α_s and β, which is different from the well-known lamellar shaped matrix in other common (α + β) alloys. However there exists only quantitative change in D10/ AC aged (Fig. 4.11.b) induced by aging, as the duplex phase remains, only the proportion of α arises, accompanied by the drop in the β content. So a different mechanism of α_s formation could be confirmed during aging via a $\beta \rightarrow \alpha_s$ transformation. Generally less α_s could be harvested in D10/ AC aged than in D10/ WQ aged.

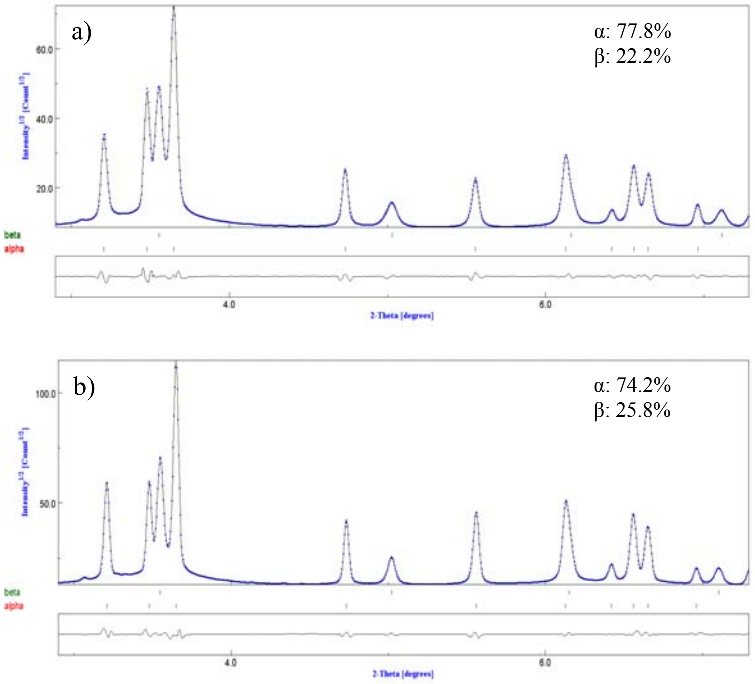

Figure 4.11 Refined diffraction patterns and phase contents of the aged conditions: (a) D10/ WQ and (b) D10/ AC.

4.3 Surface properties

4.3.1 Roughness

Surface profiles and roughness of D10/ WQ and D10/ AC after EP and SP are compared in Fig. 4.12. Both electro-polished surfaces of the two conditions are relatively smooth, and will be served as reference free from surface defects. The roughness of shot peened conditions increases in comparison with EP reference. SP brings about a deterioration of the surface finishing because of the plastic deformation. Meanwhile, it could be observed that D10/ WQ displays slightly lower roughness than D10/ AC after SP. This might be attributed to the difference in strength levels of the two, which results in variation in resistance to plastic deformation.

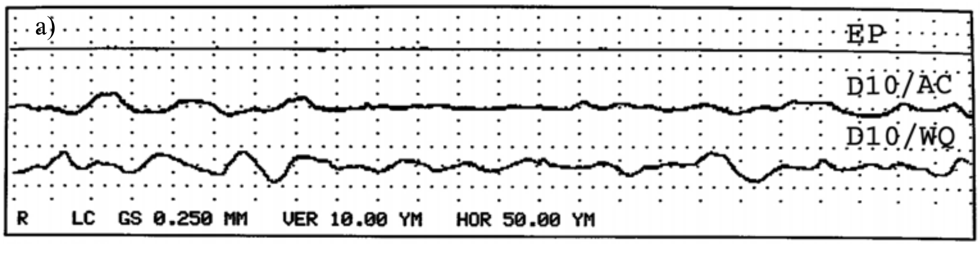

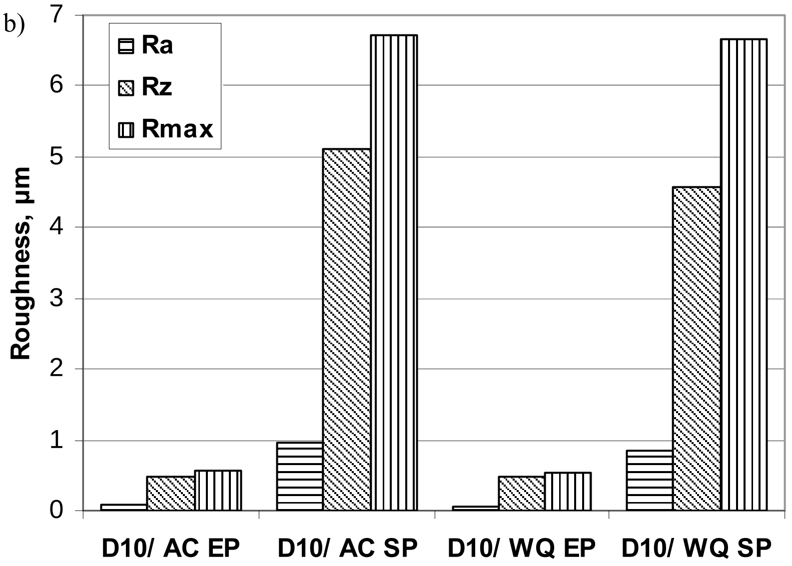

Figure 4.12 Surface finish of D10/ WQ and D10/ AC after EP and SP: (a) surface profiles, (b) roughness.

4.3.2 Microhardness-depth profile

The microhardness-depth profiles of D10 peened and heat-treated were presented in Fig. 4.13. In the near surface region, the as peened ones exhibit enhancement in microhardness, which could confirm the SP-induced work-hardening effect due to the increase in dislocation density. Both D10/ WQ and D10/ AC are hardened to similar levels, reaching maximal values around 490 HV at the surfaces. However, the influenced zone of D10/ WQ in Fig. 4.13.a spans to 0.4 mm, shallower than that of D10/ AC (Fig. 4.13.b), which arrives at the depth of 0.6 mm. Beneath the respective influenced zones, the bulk statuses reveal the original hardnesses of the unpeened conditions, around 460 and 445 HV for D10/ WQ and D10/ AC, respectively. In view of the lower original hardness of D10/ AC, maximum increase in hardness in D10/ AC resulting from SP reaches 10 %, more prominent than that in WQ by 7 %. This suggests that the degree of cold work in D10/ AC is higher than that in D10/ WQ. Based on the depth of affected zone and the amount of enhancement in hardness, it could be inferred that the air cooled condition displays higher work-hardenability than the water quenched. This could be understood that the basic structure of D10/ WQ is already strengthened to a higher level than that of D10/ AC, due to the promoted α_s precipitation from decomposition of martensite in the former, compared to the β-transformation induced α_s in D10/ AC. Correspondently, the work-hardenability of WQ is less pronounced than the air cooled condition (referred to 4.2.3).

After preheating the peened specimens to 450 ℃, both maximum microhardnesses at the surfaces in two microstructures decrease to around 480 HV. Meanwhile, the influenced zones shrink evidently. It suggests that cold work is partially recovered as a response to the thermal exposure. Additional soaking at 450 ℃ for 1 h leads to further drop of the hardness to about 460 HV and shrinkage of the affected zone (~0.2 mm) in D10/ AC. However, for D10/ WQ, the hardness at the near surface region almost restores to the bulk status. In other word, cold work in D10/ WQ is fully recovered, no work-hardening resulting from SP could be preserved after preheat plus 1 h soaking at 450 ℃. This is also confirmed by the results after 55.6 h soaking. The two profiles converge. The same phenomenon also shows up for D10/ AC, as no much reduction of hardness could be observed after keeping at 450 ℃ for 55.6 h. Thus it could be concluded that the thermal stability of cold work in D10/ AC is better than that of D10/ WQ, part of the work-hardening effect in D10/ AC could be still retained after exposure at 450 ℃ for 55.6 h.

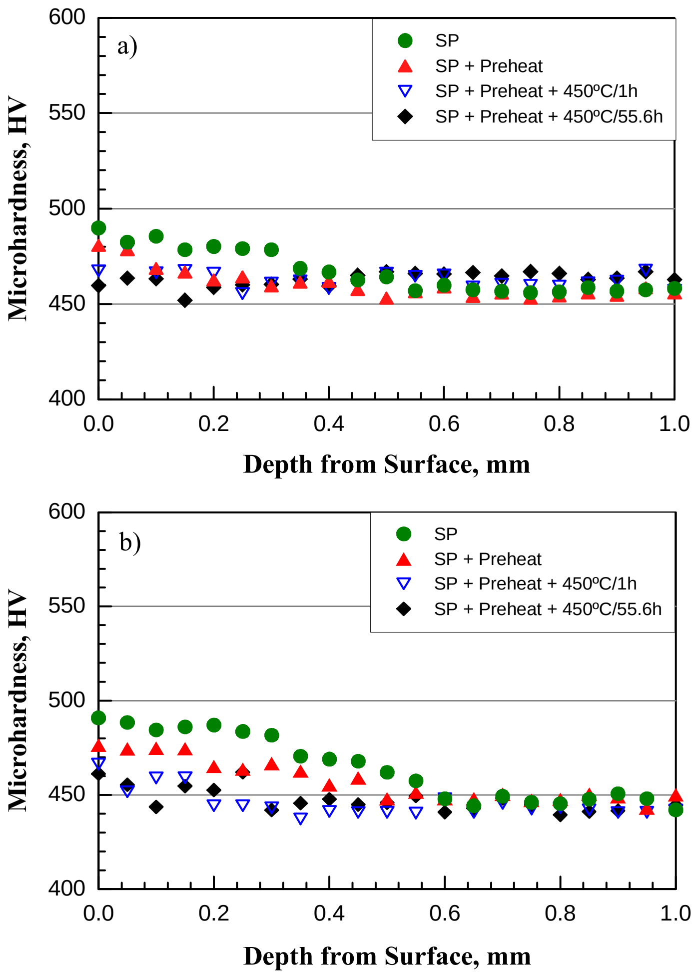

Figure 4.13 Microhardness-depth profiles of the as-peened the thermal-exposed: (a) D10/ WQ, (b) D10/ AC.

4.3.3 Residual stress

Fig. 4.14 displays the residual stress profiles of D10 specimens after SP and thermal exposure. For the as-peened ones, the maximum residual compressive stresses of around 970 MPa in D10/ WQ and 910 MPa in D10/ AC are produced at 20 µm beneath the surface. With the increase of depth from the surface, the residual stress profiles show drastic declining gradients, ending up with around -180 MPa at 200 µm beneath the surfaces. These areas should be considered as the main effective zones of the residual compressive stresses. Beyond these zones, residual stresses gradually approach zero.

After preheat, residual compressive stresses relax. The retained maximum stresses at specimen surface are reduced to -490 and -535 MPa in D10/ WQ (-40 µm) and D10/ AC (-20 µm), respectively. The thermal relaxation of maximum residual stresses corresponds to 50 % and 41 % for the D10/ WQ and D10/ AC. This might be related to the higher thermal stability of cold work in air cooled one as discussed in 4.3.2. The effective zones lie in the same area as that of the peened profiles, down to 200 µm under the surface. The stresses at the turning points of the gradient profile in both conditions are around 110 MPa. SP + preheat + 450 ℃/1 h results in only slight drop in both stress profiles. The maximum stresses hardly decreases compared to that of SP + preheat. Further prolongation of heat-treatment duration to 55.6 h barely causes stress relaxation in D10/ AC. The maximum residual stress keeps still at 520 MPa. While, residual compressive stress in D10/ WQ is lowered, with maximum value of 450 MPa still at 40 µm below the surface. So it is obvious that the thermal stability of residual compressive stress in AC is higher than in WQ, which is in agreement with the tendency of cold work in these two microstructures.

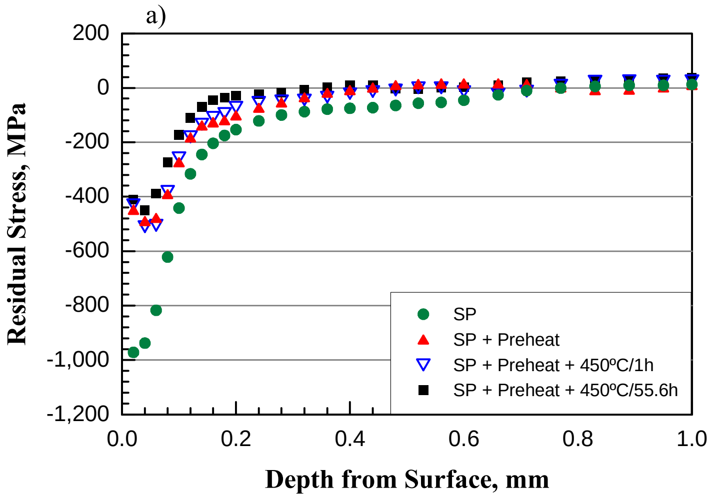

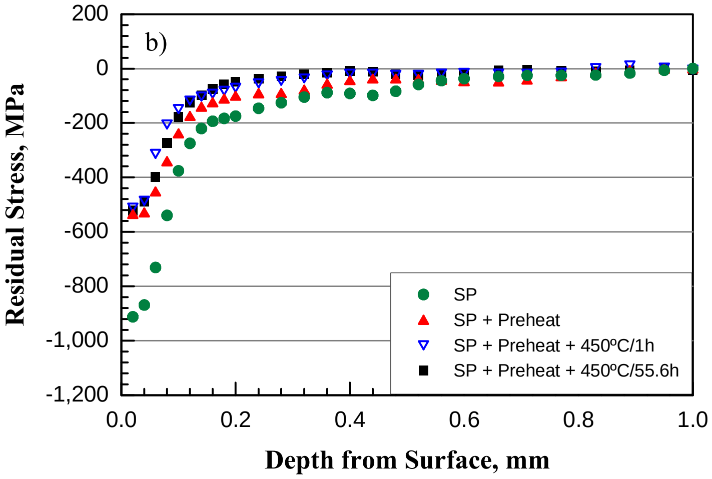

Figure 4.14 Residual stress-depth profiles of the as-peened and the thermal-exposed: (a) D10/ WQ, (b) D10/ AC.

4.3.4 Microstructure

As the later fatigue tests are also implemented at 450 ℃, although this temperature is beneath the effective recrystallization temperature of Ti-6246, it is still necessary to take the influence of SP-induced cold work at the near surface regions into account, because the recrystallization temperature decreases with the increase in dislocation density. And relevant alternation of the surface microstructures of T-6242 and Beta-C has been confirmed after SP and ball burnishing using selective surface heat treatment, which leads to improvement in HCF strength [83, 84]. The microstructure of a shot-peened fatigue specimen (D10/ WQ as an instance) treated in the fatigue chamber at 450 ℃ for 60 h is shown in Fig. 4.15. No change in the microstructure at the surface region could be observed. So it could be assured that the SP does not influence the microstructure on matter at RT or at 450 ℃.

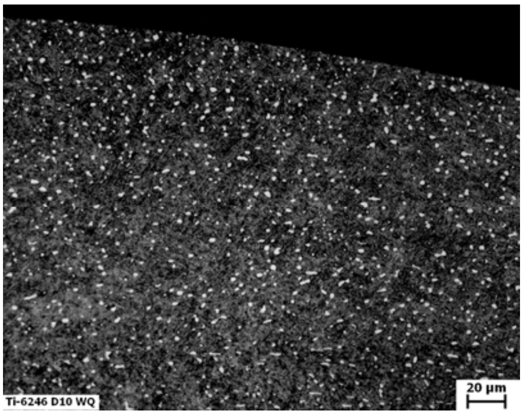

Figure 4.15 Microstructure of an as-peened D10/ WQ treated at 450 ℃ for 60 h.

4.4 Tensile properties

Tensile strength levels of the typical microstructures of the two alloys are described in form of yield stress (YS), ultimate tensile strength (UTS). Ductility is characterized by the fracture elongation EL, reduction of area RA and true strain ε_F. Ti-6246 is tested at both RT and 450 ℃, because of its oriented application for elevated temperature components in aero engine compressors. Except three unachieved conditions PC/ WQ and PC/ AC at 450 ℃, detailed data are presented in Tab. 4.1.

Table 4.1 Tensile properties of Ti-6246.

		YS (MPa)	**UTS (MPa)**	**El (%)**	**RA (%)**	**ε_F = ln (A_0/A_F)**
As-received	**RT**	1050	1155	10.5	15.8	0.17
	450 ℃	690	885	11.8	29.9	0.35
D10 AC	**RT**	1315	1375	6.9	12.9	0.14
	450 ℃	975	1110	7.2	17.3	0.19
D10 WQ	**RT**	1585	1600	1.8	2.3	0.02
	450 ℃	1170	1300	2.7	2.8	0.03
PC/ AC	**RT**	1275	1365	5.8	12.7	0.13
	450 ℃	Failed at test due to fracture threads or necks				
PC/ WQ	**RT**					
	450 ℃					

Compared to the as-received conditions, great improvement in strength could be achieved in D10 through TMP, as shown in Fig. 4.16. Meanwhile the cooling rate from the recrystallization temperature plays a significant role in the strength levels. At both RT and 450 ℃, D10/ WQ provides superior YS and UTS compared to D10/ AC. Considering the difference in phase constitutions of the two, D10/ WQ has total an α fraction of 77.8 %, which means that there exists more α_s in it than in D10/ AC by 3 % (referring to 4.2.3). On the other hand, with respect to the different phase formation mechanisms during TMP, conclusion could be made that the strengthening effect by means of α_s precipitation through α'' decomposition in the water quenched is more remarkable than that caused by the β-transformation induced α_s in D10/ AC. In short, the martensite-involved transformation in this study offers more prominent strengthening effect than normal. But it is still early to ascribe the inherent reason to the quantitative difference in the precipitation. The Proposition about the influence of α_s particulates morphology such as grain size effect should also be taken into account. Worth mentioning, common (α + β) alloys such as Ti-64 have lamellar shaped α_s in the matrix. The mechanical properties have great dependence on lamellae-related slip lengths. Ti-6246 is different, as the matrix in our processed microstructure is based on particle shaped α_s and β. The normal relationship concluded concerning slip lengths might be not applicable for Ti-6246. Comparing Fig. 4.16.a and b, it is evident that with the increase in the testing temperature, tensile strengths deteriorate, correspondently ductilities get improved.

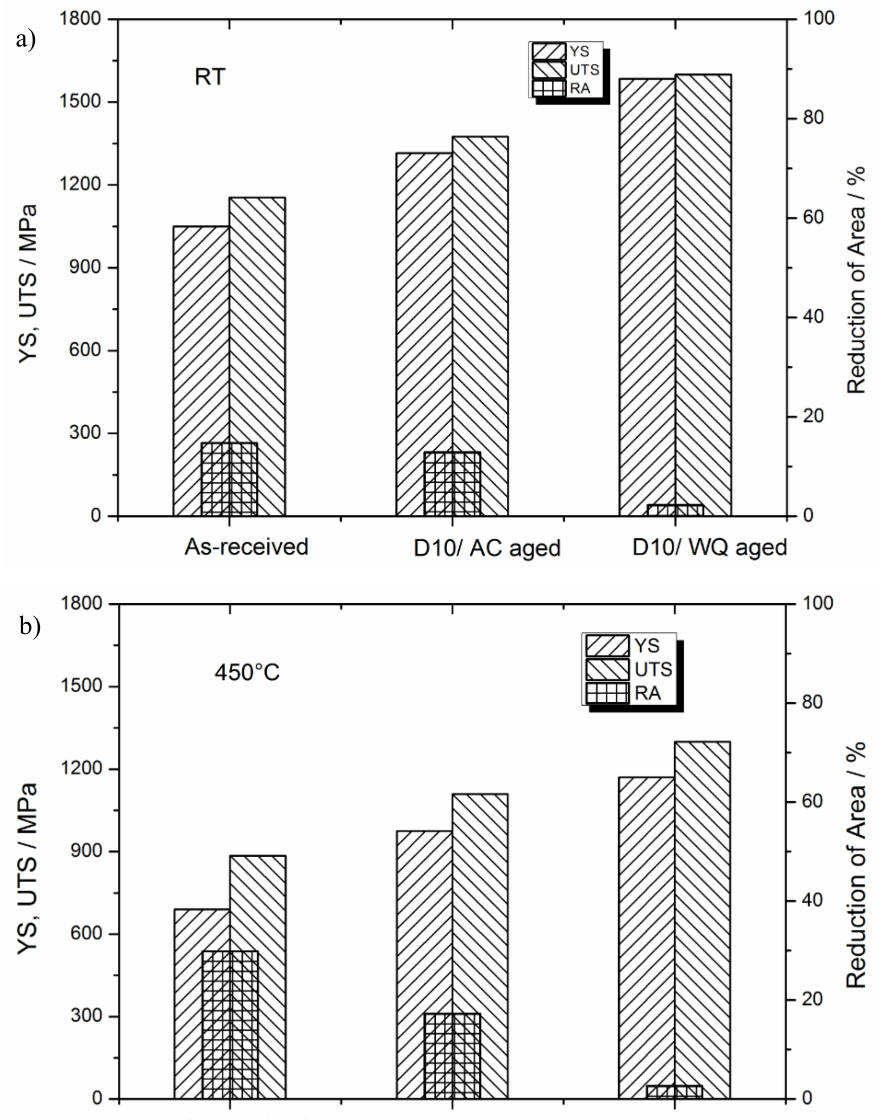

Figure 4.16 Comparison of the D10 to the as-received: (a) at RT, (b) at 450 ℃.

Tensile properties of different microstructural conditions of TIMETAL-54M are listed in the Table 4.2. The impact of cooling rate on yield stress and tensile strength is very prominent in both β-annealed and duplex structures. With the increase of α_p percentage, the cooling rate effect deceases and finally vanishes in EQ. The strength levels of β and D15 are comparable, higher than that of EQ. The tensile ductility values are poorest in β-annealed conditions and highest in EQ with values in D15 in between. The increase in ductility with an increase in α_p volume fraction can be interpreted by a reduction in ($\alpha + \beta$) colony size and decreasing slip length [35].

Table 4.2 Tensile properties of TIMETAL-54M.

		YS (MPa)	**UTS (MPa)**	**El (%)**	**RA (%)**	**$\varepsilon_F = \ln(A_0/A_F)$**
β	**WQ**	1215	1310	1.5	5.1	0.06
	AC	1020	1100	8.9	13.8	0.15
D15	**WQ**	1245	1315	8.1	28.8	0.35
	AC	1055	1110	15.4	39.4	0.49
EQ	**WQ**	1145	1145	12.6	46.0	0.62
	AC	1135	1145	15.5	52.4	0.72

4.5 High cycle fatigue behaviour

4.5.1 Microstructural optimization regarding HCF

The HCF performances of the developed various microstructures were characterized and assessed under rotary-bending load at RT using electrolytically polished specimens. S-N curves of various microstructures of TIMETAL-54M are also illustrated in Fig. 4.17, according to two categories, WQ and AC respectively. Difference in cooling rates hardly brings out influence in EQ. With the decrease of α_p, namely increase of martensite produced during WQ, the improvement in fatigue limit resulting from fast cooling rate is presented in both D15 and β structures, especially the latter. β/ WQ excels among the three types. EQ ends up with the lowest strength level, with D15/ WQ in between. In view of the air cooled ones, a competing mechanism between alloy element partitioning effect (AEPE) and α colony size effect decides the fatigue behaviour. For structures such as D15/ AC and β/ AC, the negative influence of AEPE on HCF overwhelms α colony size effect, thus β/ AC is superior to D15. But for EQ which is consisted of fully α_p, is hardly influenced by either AEPE or α colony size due to its special structure, therefore, an excellent performance is expected.

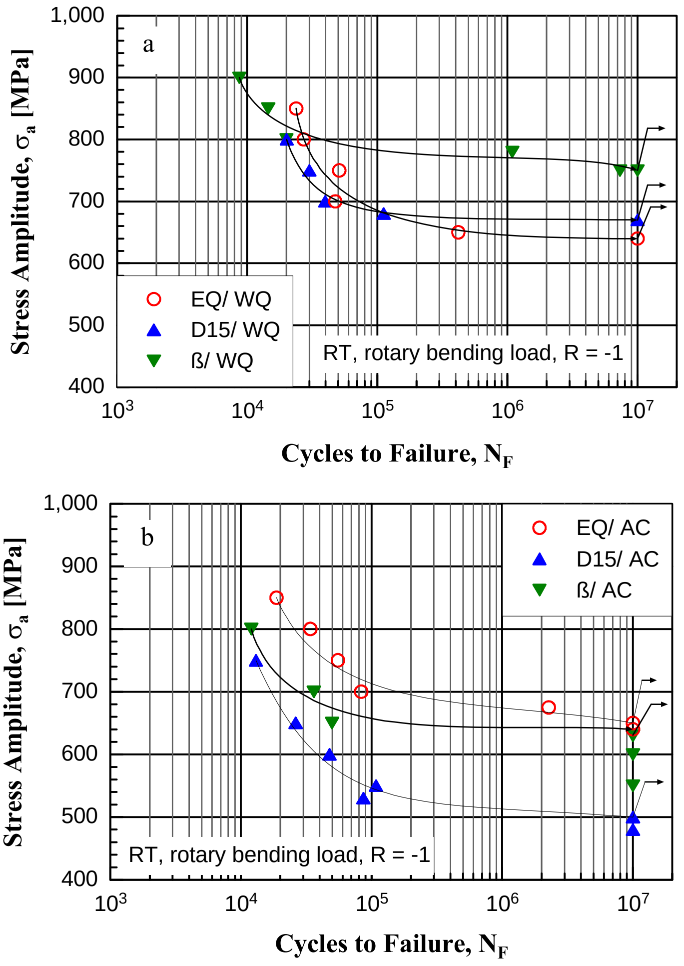

Figure 4.17, HCF performance of various microstructural conditions in TIMETAL-54M at R-B load: (a) WQ, (b) AC.

For Ti-6246, D30, D10, β and the as-received are compared with each other in both WQ and AC conditions, respectively shown in Fig. 4.18.a and b. At first, the contrast between the two graphs below considering the cooling rates reveals significant advantages resulting from WQ. The resultant improvements in fatigue strengths compared to the air cooled ones are brought out to be 50, 75, and 100 MPa in D30, D10 and β annealed structure, respectively. This increasing tendency corresponds to the decrease of α_p fraction in these three structures. The less α_p there is, the more martensite will be induced during WQ, furthermore the stronger α_s strengthening effect as stated in session 4.4. The poorest is D30, but it still has better performance than the as-received. D10 shows optimal fatigue strengths of 825 and 750 MPa in WQ and AC, respectively, which are higher than those of β annealed structure. So with respect to HCF, D10 with relatively less α_p fraction stands out in three types of microstructures owing to its superior strength levels. The influence of microstructure on HCF in Ti-6246 is not consistent with the effect of competing mechanism between AEPE and α colony size effect, which leads to fatigue strength of β annealed structure higher than D15 in

TIMETAL-54M. With respect to the microstructures of these two alloys in Fig. 4.5 and Fig. 4.7, evident difference could be noticed that duplex structures in Ti-6246 have fine particle shaped matrix, unlike the lamellar matrix in those of TIMETAL-54M. In other word, there is no α colony. Namely, only the AEPE is critical in duplex of Ti-6246, and α colony size effect depending on α lamellar length is not valid in duplex structures. While it still functions in the β annealed condition, because it has lamellar structure. These imply that D10 with fine matrix eludes the harmful influence on HCF, and probably brings about a strengthening effect due to the grain refinement in matrix in contrast to β annealed. With only influence of AEPE, it is reasonable for D10 to show a better HCF performance than D30, as the detrimental AEPE effect is more serious in the latter.

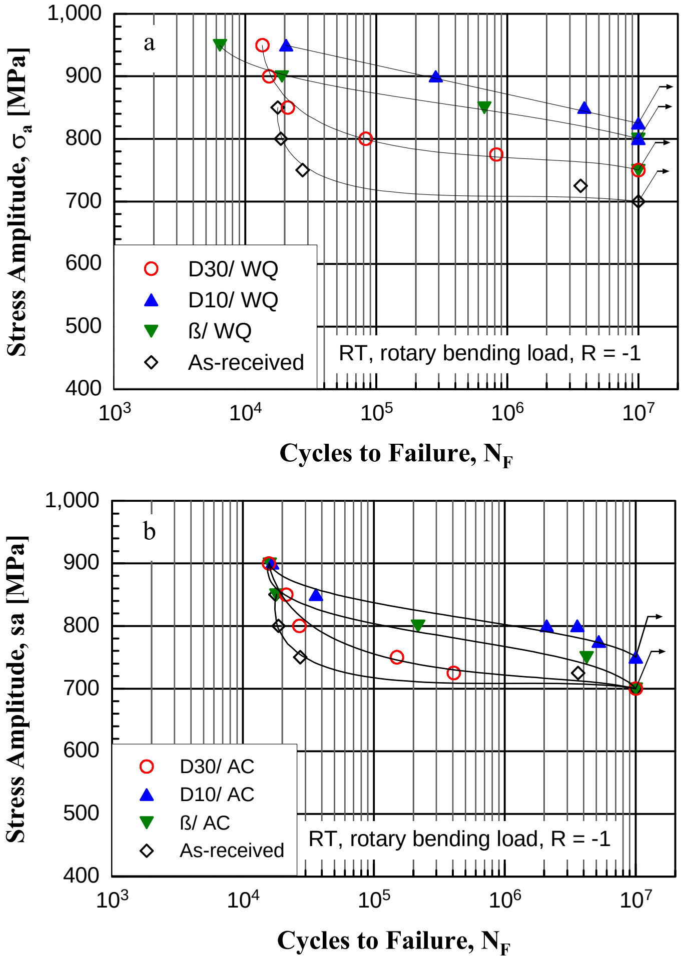

Figure 4.18, HCF performance of various microstructural conditions in Ti-6246 at R-B load: (a) WQ, (b) AC.

4.5.2 Influence of loading mode

The fatigue behaviour at R = 0.1 has been characterized at axial load. This involves the variant of loading mode into consideration. Cautions need be taken to determine whether axial load or R-B should be chosen for the comparison with the axial fatigue tests at R = 0.1. The S-N curves of representative microstructures such as D10/ WQ, PC/ WQ, as-received of Ti-6246 and TIMETAL-54M D15/ WQ at axial load (R = -1) are presented in Fig. 4.19, in contrast to those tested at R-B. Fatigue strengths at R-B distinguish themselves with advantages against axial load by even more then 200 MPa. As R at both types of loading are fixed at -1, the potential impact factor resulting to the huge distinction could be only attributed to the difference in stress distribution across the specimens' cross sections. Under R-B, the maximal applied stress would be always at a certain point on surface, and decrease gradually with increase of depth from the specimen surface to the interior, finally reaching zero at the geometrical centre. Axial load enables an even stress distribution simultaneously at all points at cross sections, suggesting a whole cross section functions as the control volume. In comparison, the control volume at R-B load is only the region at the surface layer, which is much smaller than that at axial load. It implies higher probability of cumulative damage resulting from surface or bulk discontinuities in axial load than in R-B. That is why all materials tested in this study demonstrate much degraded performance at axial load. This influence is also confirmed by M. Nakajima [53] in a high strength carbon chromium steels that under axial load fatigue limit is much lower.

Based on these results, it could be concluded that the loading mode does have significant influence on HCF in both Ti-6246 and TIMETAL-54M, and the aimed mean stress effect investigation should be based on the results gathered at the same load, i.e. axial load here.

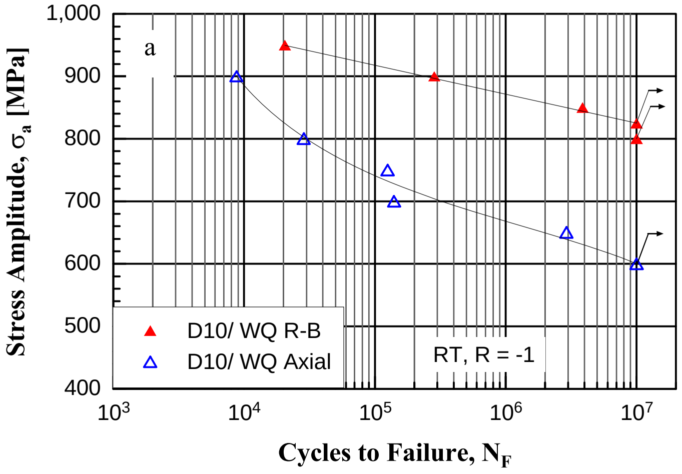

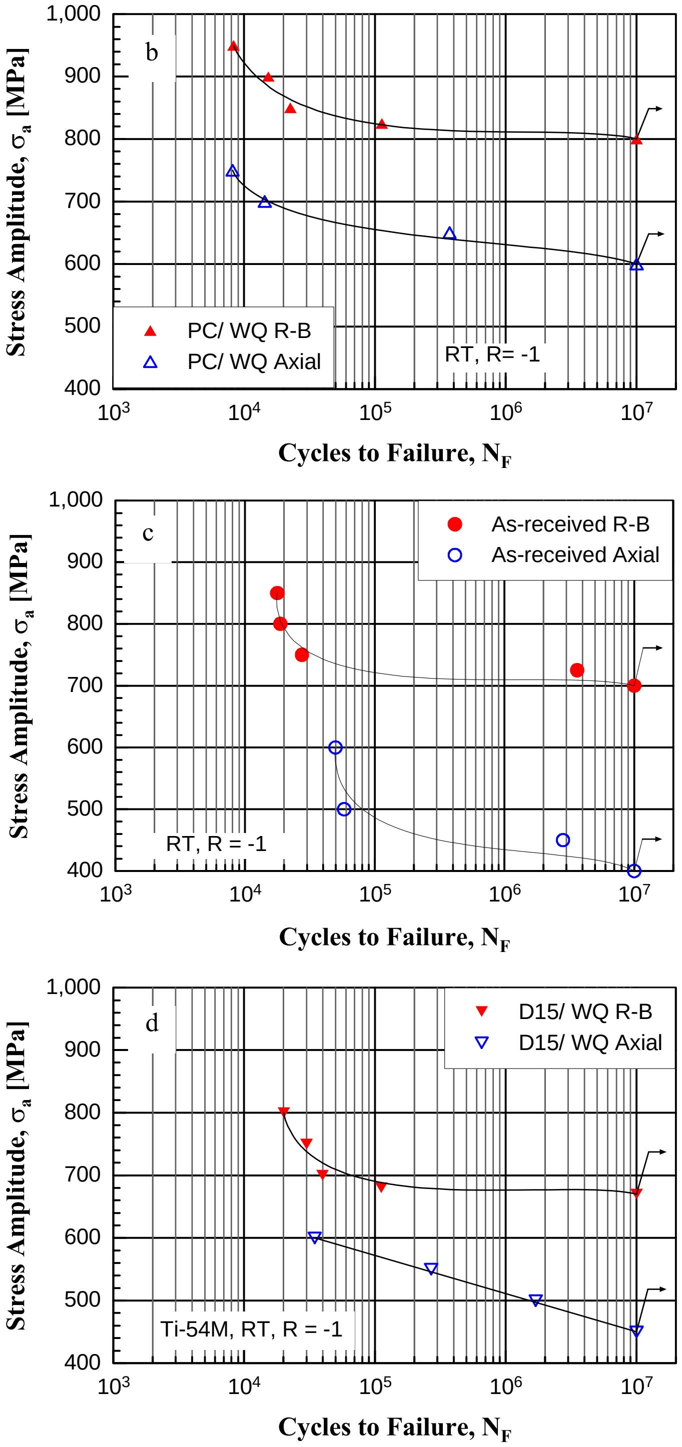

Figure 4.19, HCF performance of various microstructural conditions at both rotary bending load and axial load: (a) Ti-6246 D10/ WQ, (b) Ti-6246 PC/ WQ, (c) Ti-6246 as-received, (d) Ti-54M D15/ WQ.

4.5.3 Influence of temperature

Only Ti-6246 would be covered in the discussion about the influence of temperature, excluding TIMETAL-54M, due to specific application of Ti-6246 under elevated temperature.

Axial HCF tests at R = 0.1 and -1 were performed at both RT and 450 ℃. Both D10 and PC structures were characterized to reveal the response of HCF performance to the increase of temperature, as showed in Fig. 4.20. In S-N curves of each microstructural condition, the upper two curves describe the fatigue behaviour at R = 0.1, the lower two correspond to fatigue at R = -1. At a certain R, with the increase of testing temperature, the fatigue strengths of most microstructural conditions are slightly impaired by maximum 50 MPa. In Fig. 4.20.a and b the S-N curves of both D10/ WQ and D10/ AC even converge no matter at R = 0.1 or R = -1, only slightly deviate at the high cycle regime. The elevation of temperature to 450 ℃ does not incur marked degradation. This suggests that Ti-6246 has a rather acceptable thermal stability.

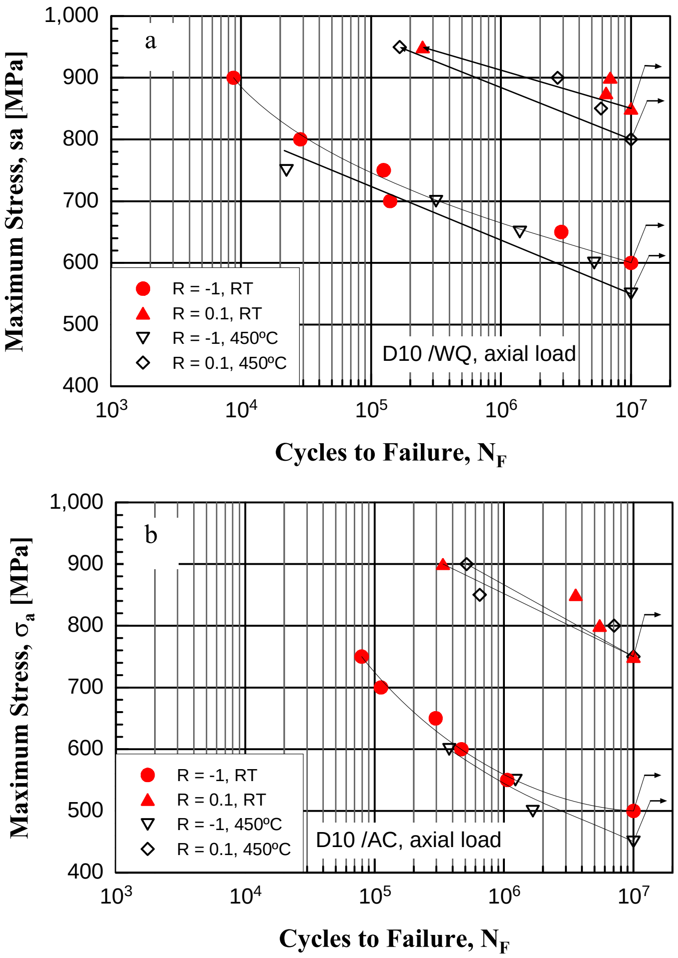

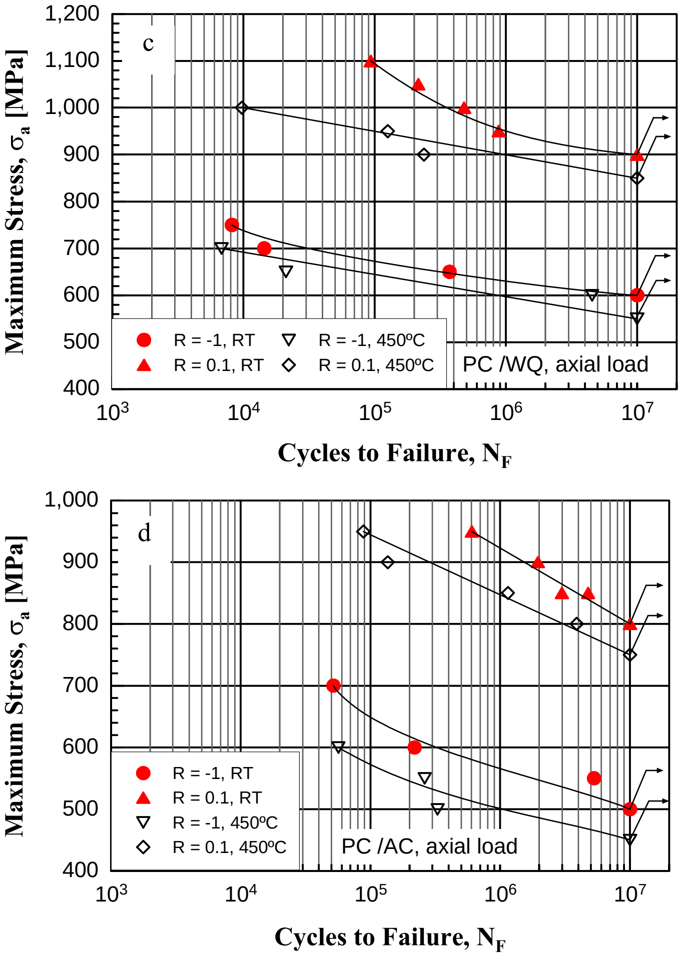

Figure 4.20, HCF performance of various microstructural conditions in Ti-6246 at both RT and 450 ℃: (a) D10/ WQ, (b) D10/ AC, (c) PC/ WQ, (d) PC/ AC.

The slight degradation of HCF at 450 ℃ is related to the increase of temperature. The stacking fault energy of the material is enhanced at elevated temperature. Thus dislocation motion is correspondently more active. Meanwhile oxidation at the slip steps is exacerbated. The combination of intensified of dislocation and oxidation result in acceleration in both crack nucleation and propagation.

4.5.4 Mean stress sensitivity

As shown in Fig. 20, at a certain temperature, there exists significant variation in fatigue limits at R = 0.1 and -1, displayed as great gaps between the two groups of S-N curves in each graph. Most gaps reach even over 200 MPa. The mean stress level plays an important role in fatigue behaviour. Generally it is evident that fatigue strength rises as increasing the load ratio at a given stress level. For TIMETAL-54M, according to the modified Goodman relation, the correlation between UTS (referred to Tab. 4.2), mean stress and fatigue limit at R = 0.1 and -1 could be presented in terms of Smith diagrams. In Fig. 4.21.a three coordinate points (σ_{max}, σ_m) of D15/ WQ at R= -1, 0.1 and 1 are linked with two dashed lines sequentially. The point $(\sigma_{max}, \sigma_m)_{R = 0.1}$ which symbolizes the experimentally determined fatigue limit at R = 0.1, is locating very near the value estimated from the intercept of the linear connection between $(\sigma_{max}, \sigma_m)_{R = -1}$ and $(\sigma_{max}, \sigma_m)_{R = 1}$ on R = 0.1 line. For TIMETAL-54M D15/ AC (Fig. 4.21.b), the three points are aligning linear, namely the experimental limit at R = 0.1 is superimposed with the estimated value. The mean stress effects of TIMETAL-54M are normal in both D15/ WQ and D15/ AC.

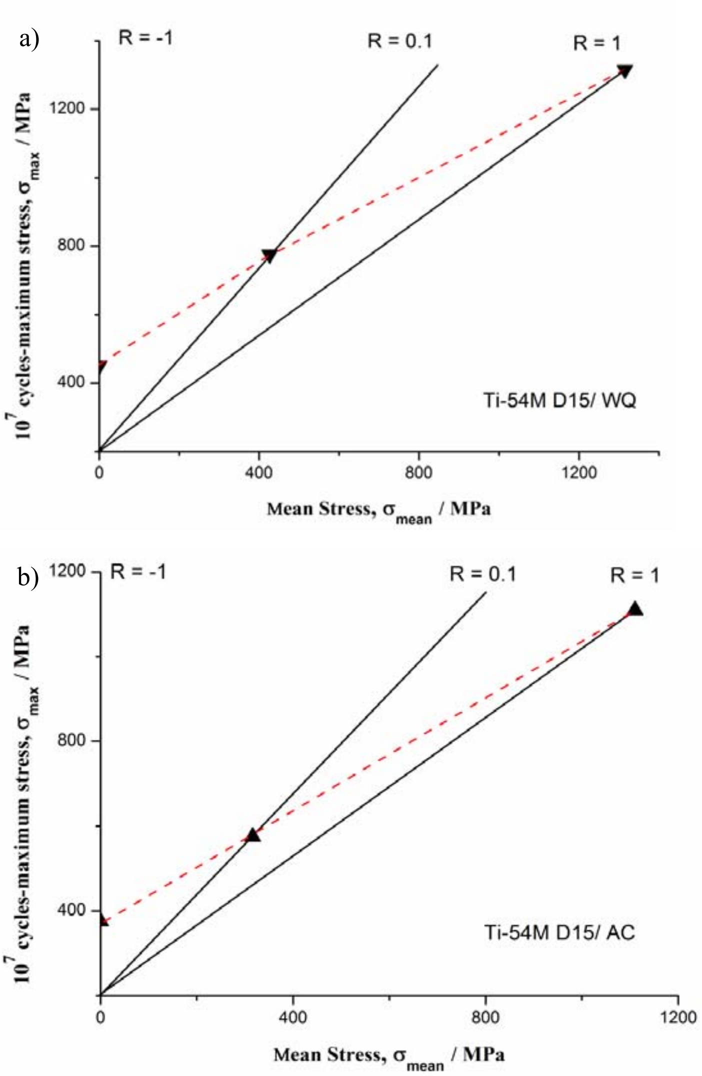

Figure 4.21, Smith diagrams of various conditions: (a) TIMETAL-54M D15/ WQ, (b) TIMETAL-D15/ AC.

For Ti-6246, mean stress effects were denoted in Fig. 4.22 regarding different cooling rates. For both D10/ WQ and AC at RT, the connected three coordinates with dashed lines exhibit fatigue limits at R = 0.1 very close to those estimated. With the increase of temperature to 450

℃, the strength levels at all three R slide down, respectively, corresponding to the slight decrease of fatigue limits as the testing temperature goes higher (Fig. 4.20). However Smith diagrams still display quite agreeable estimation of strength limit at R = 0.1 to those detected by experiments. So normal mean stress effects were displayed in both D10/ WQ and AC.

The mean stress effects in all duplex structures of both TIMETAL-54M and Ti-6246 are shown in this study to be normal, regardless of the cooling rate. This is contrary to the results of J. Lindemann [56]. As they found the anomalous mean stress effect (AMSS) in air cooled duplex, but normal in water quenched condition. They attributed the reason to the variation in strength levels of α_p and the matrix in the air cooled condition. While the matrix in water quenched condition could be strengthened to a comparable level to that of α_p, due to the martensitic transformation, thus higher fatigue limit could be expected, and overcomes the AMSS. Worth mentioned, their conclusions are based on the fatigue limits at R = 0.1 at axial load and R = -1 at R-B. The impact of loading modes is not excluded while analyzing the mean stress effect. As confirmed in 4.5.2, the loading mode does have great influence on HCF behaviour of both T-6246 and TIMETAL-54M. So it is not precise to draw the conclusion of AMSS in spite of impact of loading mode.

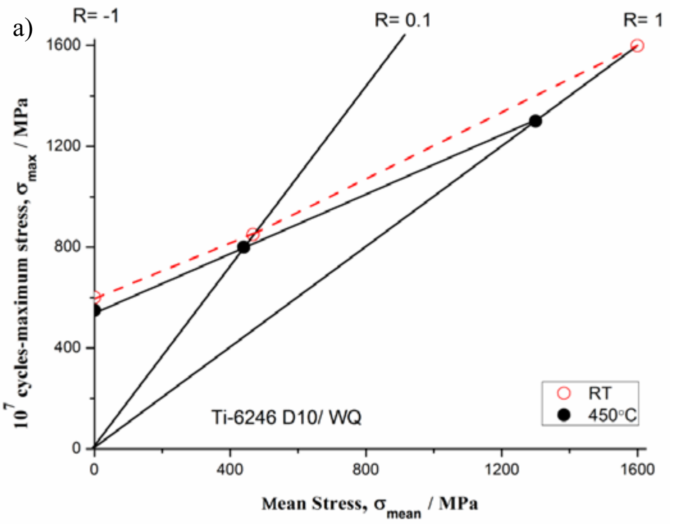

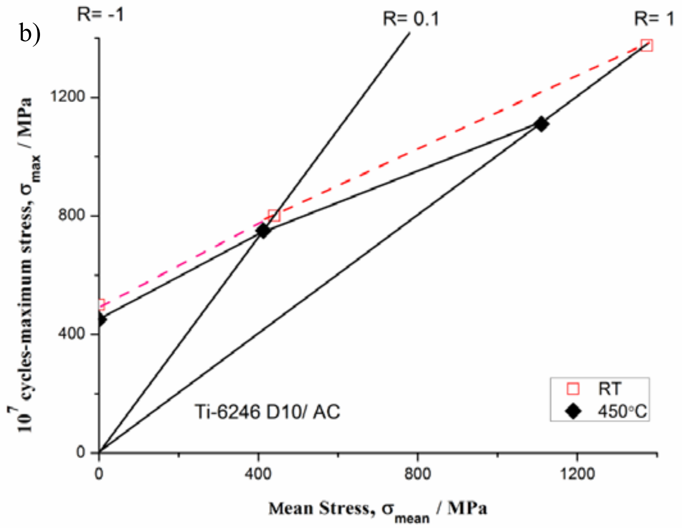

Figure 4.22, Smith diagrams of various conditions: (a) Ti-6246 D10/ WQ, (b) Ti-6246 D10/ AC.

4.5.5 Influence of atmosphere

The influence of atmosphere could be demonstrated by comparing the HCF performances of the alloys in vacuum ($<1\times10^{-5}$ mbar) to those tested in lab air at axial load (R = -1). Three microstructural conditions are shown as representatives in Fig. 4.23. For both Ti-6246 and TIMETAL-54M, the vacuum environment leads to significant enhancements in both fatigue endurance and lifetimes of all types of microstructures, compared to lab air. Specifically, the improvement in fatigue limits due to the change of atmosphere from lab air to vacuum reach 200 and 125 MPa for Ti-6246 D10/ WQ and PC/ WQ, respectively, and even 250 MPa for TIMETAL-54M D15/ WQ.

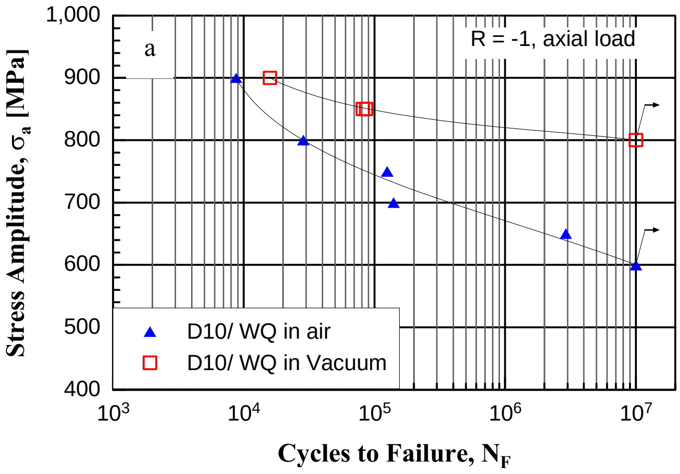

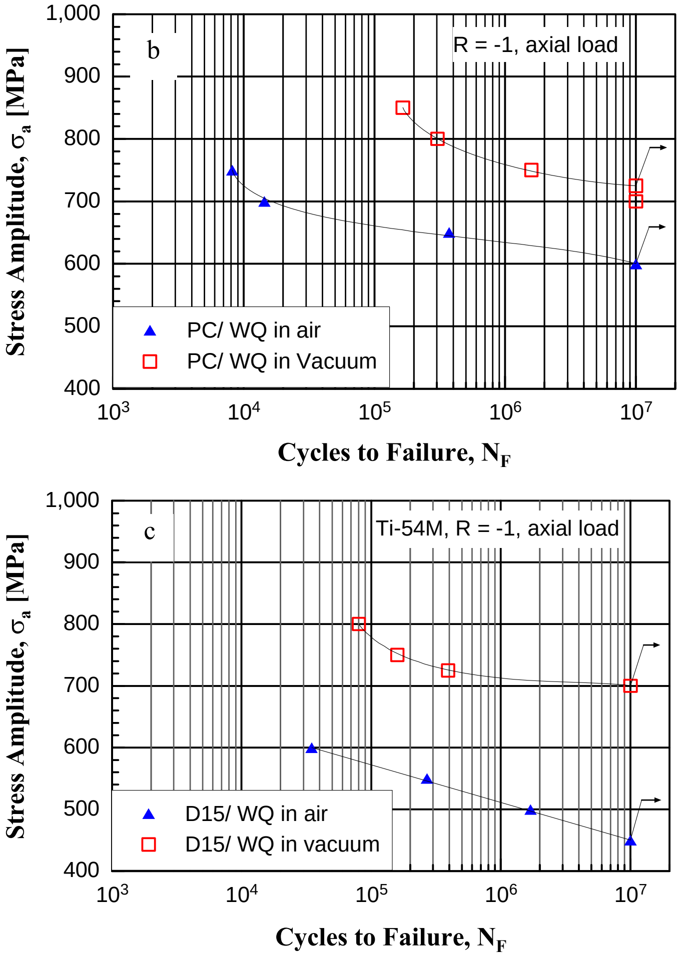

Figure 4.23, HCF performance in vacuum compared vs. in air: (a) Ti-6246 D10/ WQ, (b) Ti-6246 PC/ WQ, (c) TIMETAL-54M D15/ WQ.

The higher fatigue endurance and life time in vacuum could be interpreted from two aspects, i.e. oxidation and internal heating. The development of oxidized films at the slip steps in air would constitute a source of irreversibility in cyclic deformation on the slip bands and therefore enhance microcrack formation. Re-welding of the crack flanks in vacuum can also be regarded as a mechanistic process to account for the high fatigue lives observed in such an environment [85]. The lack of oxidation in vacuum could validate reversible slip along the original slip bands. Without the protective role from the oxidized film formed on the crack face in air, the fatigue striations which may have existed initially in vacuum will be suppressed by such friction processes and the crack propagation rate will be reduced. So vacuum retards the crack propagation and results in longer fatigue life [67].

On the other hand, titanium alloys shows high chemical affinity with oxygen and low thermal conductivity. The latter causes internal heating under cyclic stressing [86]. Especially in vacuum, the internal heating could be critical. Slip activities are enhanced in vacuum due to the internal heating, because the heat generated in a specimen ought to heat up the specimen itself without conducting heat away into ambient atmosphere, since the thermal conductivity of titanium is low. This makes both slip and spread of plastic zone around a main crack easier, i.e. raising up the plastic deformability, causing crack tip blunting. Thus stress intensity at crack tip will decease and crack growth will slow down. It was reported by E.D. Levine [87] that in titanium, the rise of 30K above RT would reduce 30% in the critical resolved shear stress (CRSS) on the basal slip plane, and it would increase the activation volume for prismatic slip. Sugano [88] and Z.N. Ismarrubie [89] have also reported the internal heating greater than 20 K above RT in vacuum (<10 Pa) and a consequent spread of plastic zone. It is inferred that the fatigue life improvement in vacuum results from the slow down of crack growth rate, which is caused by crack tip blunting contributed by the enhanced slip activity due to the internal heating (anelastic energy losses i.e. damping).

4.5.6 SP effect

The HCF behaviour of shot peened Ti-6246 was characterized at both RT and 450 ℃ with the concern about the influence of thermal exposure during testing at elevated temperature. The fatigue results of the shot peened specimens are presented and contrasted to electro-polished ones which serve as references.

As shown in Fig. 4.24, generally speaking SP could enhance the HCF performance of all microstructures at RT. Moderate increase by 50 MPa in endurance limits and prolongation of fatigue lifetimes could be observed. Referring to the results about surface properties after SP presented in 4.3.2 and 4.3.3, SP builds up cold-worked zone at the surface layer (~ 400 and ~600 µm for D10/ WQ and D10/ AC, respectively). Besides, residual compressive stresses are produced, with maximum values more than 900 MPa at the surface. It could be inferred that the improvement of HCF behaviour could be ascribed to SP induced-working hardening and residual compressive stresses, as the increased cold work and compressive residual stresses are proved to be able to retard the fatigue crack initiation and decelerate crack growth.

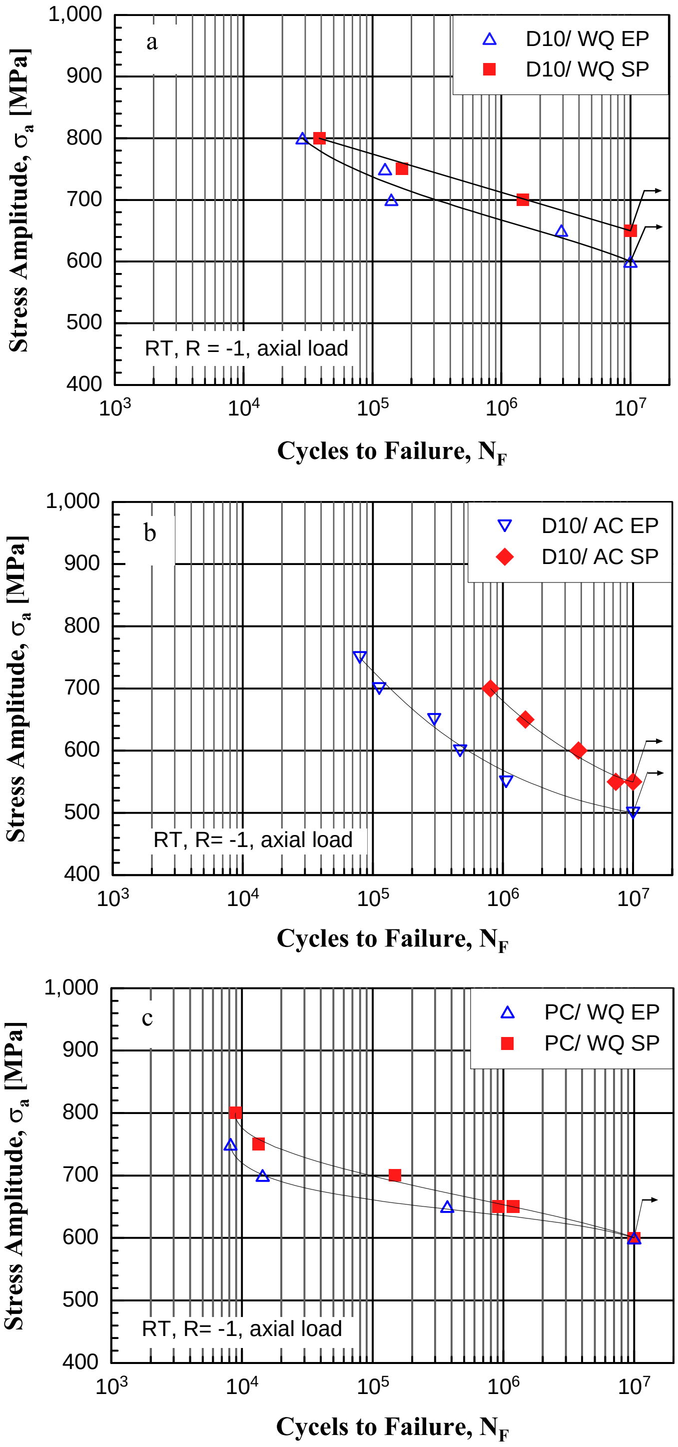
a
D10/ WQ EP
D10/ WQ SP
RT, R = -1, axial load
Stress Amplitude, σ_a [MPa]
1,000
900
800
700
600
500
400
10^3
10^4
10^5
10^6
10^7
Cycles to Failure, N_F
b
D10/ AC EP
D10/ AC SP
RT, R= -1, axial load
Stress Amplitude, σ_a [MPa]
1,000
900
800
700
600
500
400
10^3
10^4
10^5
10^6
10^7
Cycles to Failure, N_F
c
PC/ WQ EP
PC/ WQ SP
RT, R= -1, axial load
Stress Amplitude, σ_a [MPa]
1,000
900
800
700
600
500
400
10^3
10^4
10^5
10^6
10^7
Cycels to Failure, N_F

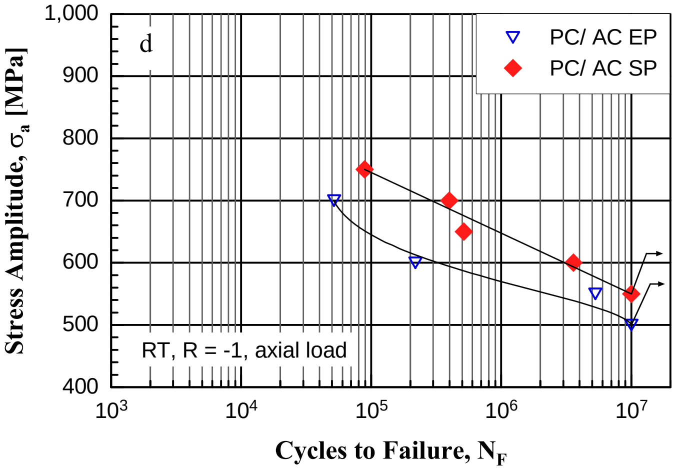

Figure 4.24, HCF performance of Ti-6246 at RT, SP vs. EP: (a) D10/ WQ, (b) D10/ AC, (c) PC/ WQ and (d) PC/ AC.

Moreover, comparing those water quenched to air cooled ones, it is observed that the positive response of HCF to SP in WQ is less significant than that in AC. This might be corresponding to the aforementioned cooling rate effect on the work-hardenability of different microstructures. Although residual compressive stresses of D10/ WQ and D10/ AC are comparable (Fig. 4.14), the SP-induced work hardening effect in AC is more pronounced than that in WQ due to the higher work-hardenability of the former. Therefore greater improvement could be produced in air cooled conditions.

In the case of subsurface crack nucleation in axial load, residual compressive stresses are not so important as for R-B load, since the cracks can easily propagate deeper into the material [90], exceeding the compressive stress field. It is argued that residual tensile stress balancing the outer compressive stresses also lead to early crack nucleation in this area [91].

With the increase of test temperature to 450 ℃, the fatigue performances of shot-peened ones turn inferior to EP (Fig. 4.25). At high cycle regime, the S-N curves of SP conditions almost converge with EP. Meanwhile reduction of fatigue lifetimes at low cycle regime (~ 10^5 cycles) occurs. The life times of fatigued specimens are within 0.56 h. According to the measured microhardness (Fig. 4.13), it could be approximated that the retained work-hardening for both D10/ WQ and D10/ AC is rather minor. No much cold work resulting from SP could be preserved after preheat plus the cycling stressing at 450 ℃. The residual compressive stresses retained after preheat could be estimated from Fig. 4.14 to account for no less than 50 %. Besides, most SP specimens failing at 450 ℃ within the low cycle regime fatigue from surface cracks regardless of the residual compressive stresses retained at the surface layers, as the surface is roughened due to SP (Fig. 4.12). Therefore, it is evident that at

450 ℃ the detrimental influence of increased surface roughness due to SP overwhelms the benefits of residual compressive stresses, accelerating the crack nucleation and shortening lifetimes.

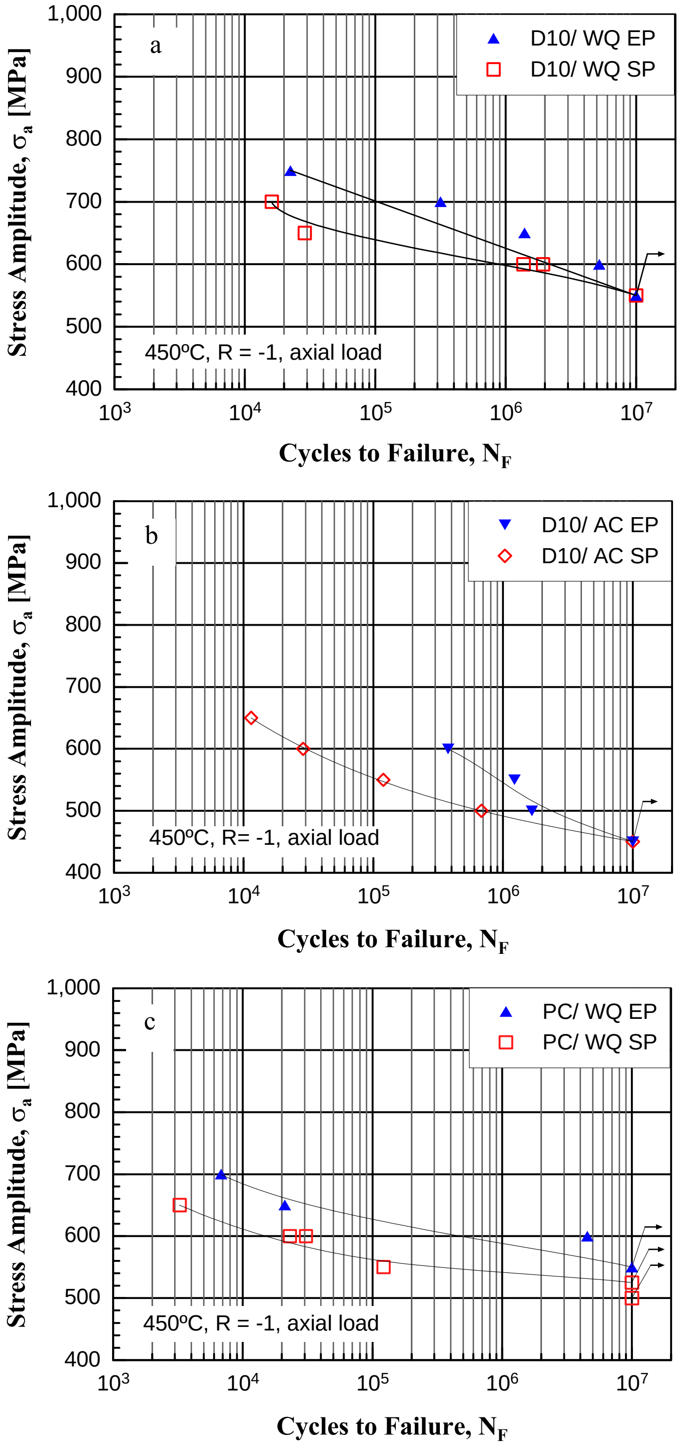

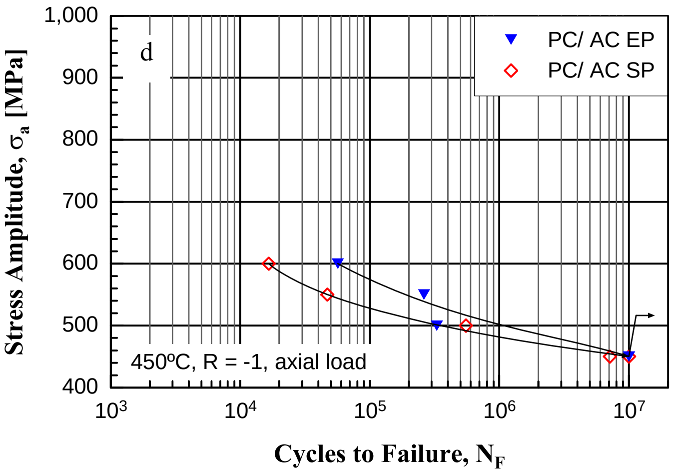

Figure 4.25, HCF performance of Ti-6246 at 450 ℃, SP vs. EP: (a) D10/ WQ, (b) D10/ AC, (c) PC/ WQ and (d) PC/ AC.

4.6 Fractography

The fracture surfaces of all fatigued specimens in this study were examined with SEM in details. TIMETAL-54M in the electro-polished reference shows a simple behaviour of crack development, merely surface cracking in spite of loading modes and microstructures et al.. While various fatigue crack nucleation (FCN) and crack propagation (FCP) modes are disclosed to operate in both electro-polished and shot peened fatigue specimens of Ti-6246, such as surface, subsurface FCN, fish eye, FCP modes transition et al. Thus following discussion in depth will be mainly focused on Ti-6246.

4.6.1 Effect of loading mode

It is observed that the loading mode has significant influence on the FCN sites. For the electro-polished specimens failing at R-B, all cracks in various microstructures are found to nucleate at the surface, which are accordant to the observation reported by C. Sauer et al [56, 92, 93] upon Ti-6246 and other titanium alloys. In Fig. 4.26 a representative fracture surface at R-B illustrates the surface initiating crack as marked by the arrows. A part of fracture debris indicates a series of slip lines at the crack nucleus. Therefore, it could be concluded that the crack nucleates by a slip band mechanism. Unfortunately the exact location of the slip bands in terms of microstructural components and crystallographic aspect can not be identified here only with SEM. A detail worth mentioning is the fan shaped region around the crack initiation site, whose boundary shows a clear morphological transition. With respect to the stress gradient at the cross section of specimen under R-B, preference in surface FCN could be expected due to the presence of maximum applied stress always at the surface. For smooth bars fatigued under R-B, surface FCN dominates in titanium alloys. But only one exception was documented by K. Tokaji et al [94] in Ti-15Mo-5Zr-3Al resulting from strain localization at GB due to dislocation pileup and/ or stress concentration.

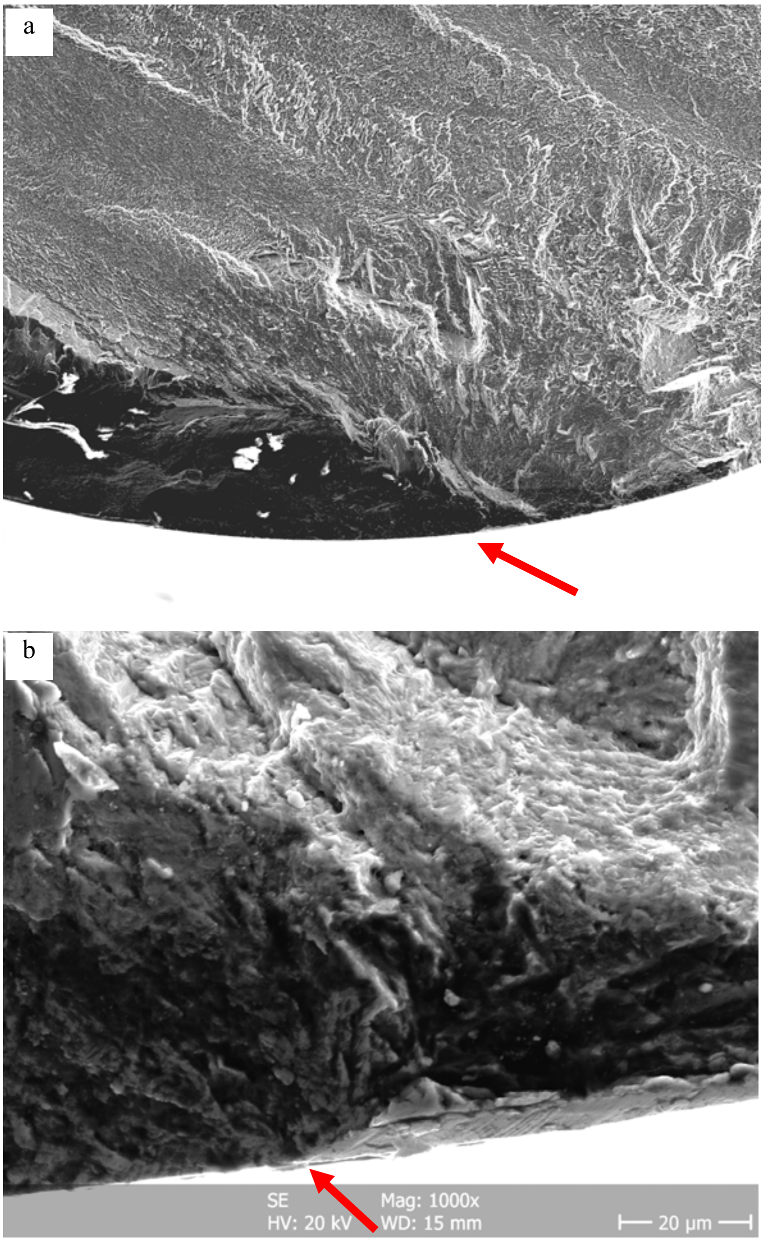

Figure 4.26, surface initiating crack of PC/ WQ, $\sigma_a = 825$ MPa at R-B with debris of fractured slip bands.

For smooth bars under axial load, the fatigue cracks appear both at the specimen surface and subsurface in all microstructural conditions independent of testing temperature and load ratio R. Typical fracture surfaces of D10 are taken as examples in Fig. 4.27. Moreover it is obvious that a fish eye is present in the Fig. 4.27.b. While a fracture surface of D10/ AC failed at 450

℃ (Fig. 4.27.c) has a subsurface initiation crack without fish eye. Thus, a conclusion could be drawn that presence of fish eye does not necessarily coexist with subsurface FCN. With regard to the fan shaped region (Fig. 4.26.a) mentioned in 4.6.1 at R-B, there is similarity in between. Both coexist with the crack nucleation sites, and symbolize transition of crack growth morphology resulting from shift of crack propagation mode. It is supposed that the fan shaped zone of the surface initiating crack is only a variant of normal circular fish eye as the crack could not grow radially. It could be taken as a half fish eye. One issue differentiating the two lies in the atmosphere where these critical zones are built up. The fan-shaped zone is formed in ambient air as the crack nucleates at the surface. However, the formation of circular fish eye takes place in vacuum as the crack initiates under the surface where air is not involved. If identity of the fan shaped zone could be proved to be identical to fish eye, the above discussion could imply that the atmosphere might not be a decisive factor for the generation of fish eye. Namely neither atmosphere nor loading mode is responsible for the shift of crack growth mode. Further discussion about fish eye will be continued later.

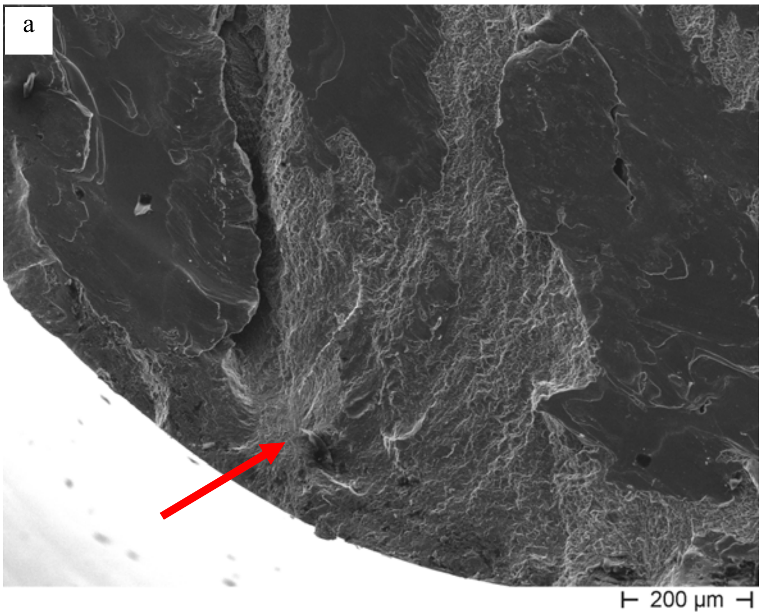

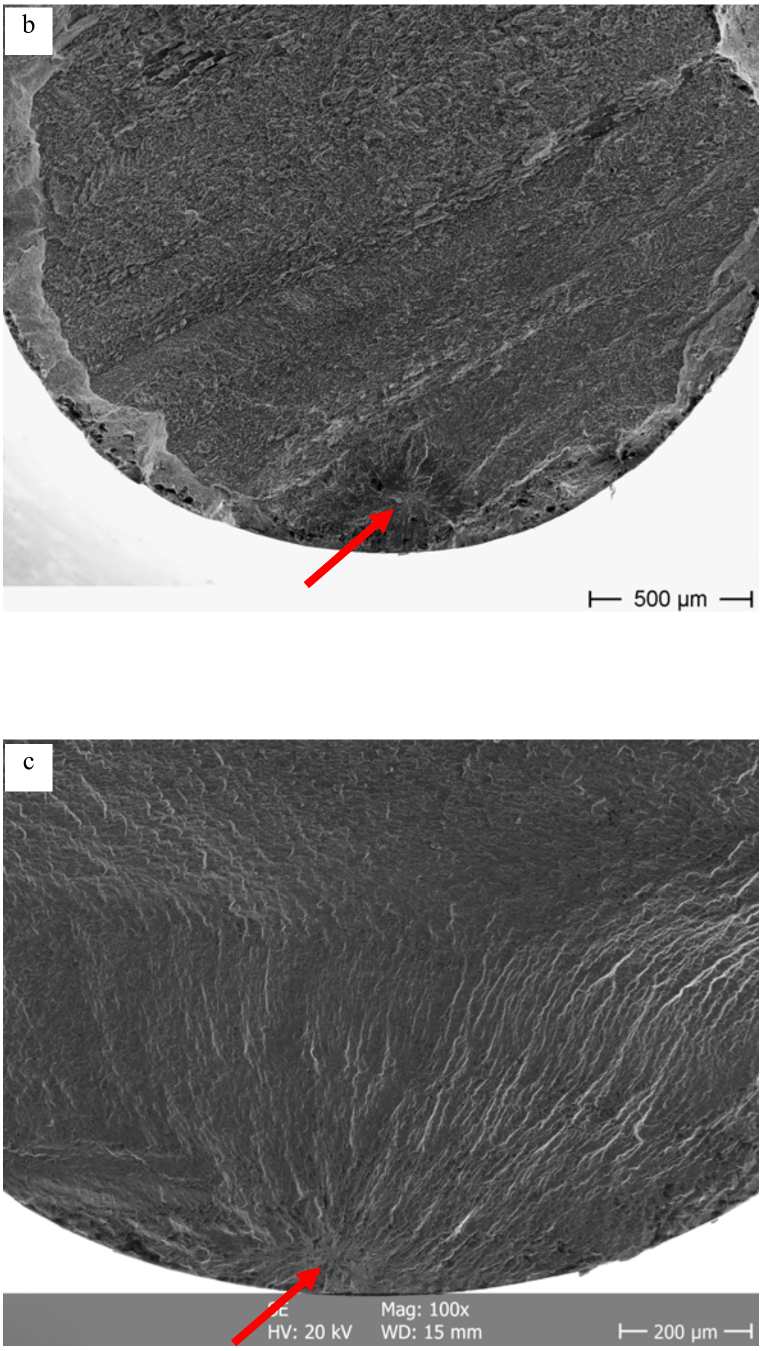

Figure 4.27 Subsurface FCN, a) D10/ WQ, $\sigma_a = 650$ MPa RT at R = -1, b) D10/ WQ, $\sigma_a = 900$ MPa, 450 ℃ at R = 0.1, c) D10/ AC, $\sigma_a = 500$ MPa, 450 ℃ at R = -1.

The depths of FCN from the surface are ranging from 100 to 600 µm. The distribution of fatigue lifetime versus depths of crack nuclei is illustrated in Fig. 4.28. There is no evident relationship between the life time and depth of crack initiation sites.

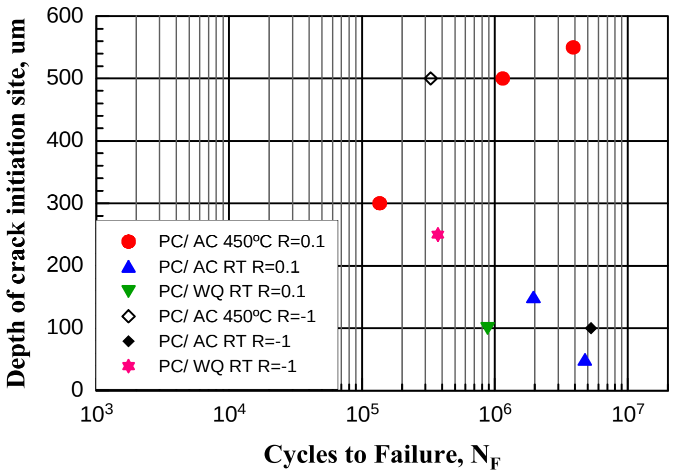

Fig. 4.28 Fatigue lifetime vs. depths of crack nuclei below the specimens surfaces in PC.

The surface FCN which usually prevails in plenty of materials fatigued at axial load could be understood as the micro-plasticity can occur more easily in grains at the materials surface because the surrounding material is present at one side only, suggesting lower restraint for the cyclic slips at the surface [42].

However, subsurface crack initiation is not common in smooth-bar fatigue failure. Usually it has been reported in high strength steels [95] and Nickel-base super alloys [96–98] at both fully reversed and none fully revered load and especially in very high cycle fatigue regime ($>10^7$). The cause is attributed to the non-metallic, intermetallic inclusion or pores which act as micro-notches and generate crack nuclei in the bulk of materials. While these presumptions could not be applied to Titanium alloys. As they are relatively pure, defects as inclusions and pores are not observed. For smooth bars at axial load, subsurface FCN and fish eyes are frequently encountered at none fully reversed load in every category of titanium alloys. In a mechanical manner, S. Adachi [99] concluded the main cause to be the formation of residual compressive stresses due to the preferential deformation at the surface under the applied tension-tension load. Whereas at load ratio R = -1, the above reason seems sceptical. Hitherto subsurface FCN and fish eyes are not intensively investigated in titanium alloys due to its rare presence in smooth fatigue bars. Limited occurrences are only documented by G. Jago [100] and J. Mendez [101]. Unfortunately the mechanisms are not fully interpreted. Regarding the applied stress amplitudes, subsurface FCN is observed to occur more frequently at lower stress levels in this study. The likelihood of the presence of subsurface FCN increases as the stress level decreases. This is confirmed by S. K. Jha in Ti-6246 [102]. As well known, crack nuclei could be more easily induced at high stress levels, because the crack threshold is less significant, it can be easily overcome. But at lower strength levels, FCN is more problematic.

It is indeed a threshold problem, and more sensitive to microstructures. Thus it is presumed that the subsurface FCN might be also related to local microstructures [103].

4.6.2 Effect of microstructure

The nucleation modes of subsurface cracks vary from each other regarding microstructures. The cooling rate seems not to have marked influence on the crack nucleation.

In D10 it is observed that two types of subsurface FCN mechanisms are operative. Fig. 4.29.a displays the first type of nucleation mode, i.e. transgranular faceting through a cluster of isolated α_p grains. It is suspected that an associated facet-formation process resulting from fracture in α_p grains along crystallographic planes favourable for slip leads to the FCN. Unfortunately neither the exact faceting angles nor the relationship between the facet planes and crystallographic planes of the hcp α phase could have been determined by the facilities available in this study. But a visualized difference presented by the grains is still discernible. Grains with typical facet angles to the load direction are numbered. Grain 1 with an angle dominant in this group of facets is approximately perpendicular to the load axis. Meanwhile it should be noticed that grain 1 is above the average size of α_p (3 µm). The less popular faceting angles are given by grain 2 and 3. It is suspected that in this region most of the grains might share similar orientation to that of grain 1, i.e. they probably belong to a same macrozone which derives from a prior β grain. Slip is prone to accumulate in this textured region. C.J. Szczepansk [104] has also reported that subsurface FCN in duplex structure of Ti-6246 (at R = 0.5) is favoured at clusters of individual α_p grains. These grains fracture by a basal <a> type slip which are oriented with a low angle between its normal and the load direction (low angle facets). M. R. Bache et al. [105] have found similar groups of facets in duplex structure of IMI685 (at R = 0.1) having a near basal orientation and aligning normal to the applied stress. It is clear that these planes at not favourably oriented for slip. They argue that slip bands in neighboring grains adjacent to the poorly oriented basal planes might induce the required resolved shear stress (RSS). Low angle α_p facets in duplex structure of Ti-64 (R = 0.1) were verified by J.L. Gilbert [106] to form by a prevalent slip in pyramidal planes of α_p grains. It is attributed to the more pronounced damage accumulation and/ or stress concentration from dislocation interactions, such as pile up resulting from slip in both <c + a > ($[11\bar{2}3]$) and <a> ($[11\bar{2}0]$) direction. In addition, high angle facets at about 44° to the loading axis as crack nucleation sites have also been reported in duplex structure of Ti-6246 to have a near basal orientation [107]. In this case FCN mechanism could be easily interpreted that basal plane are oriented for high RSS, thus basal slip can be preferentially activated.

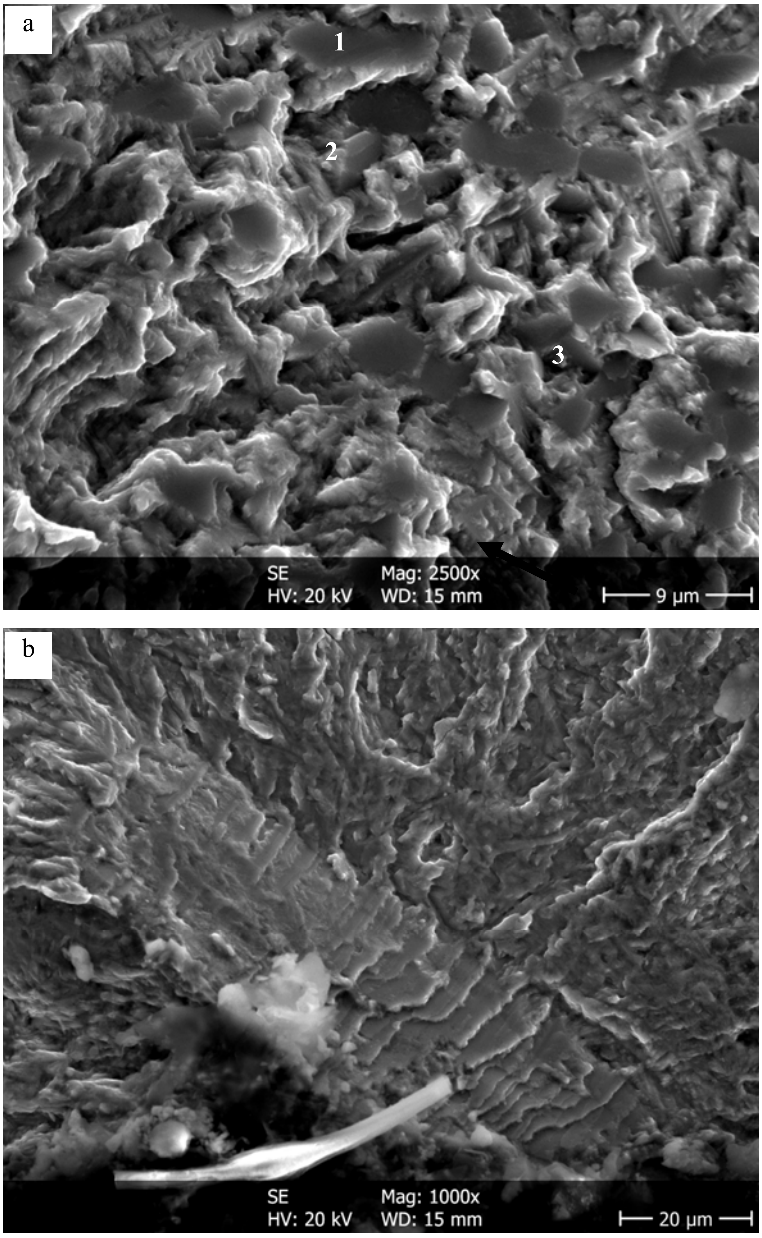

Figure 4.29 various subsurface FCN modes in D10: (a) D10/ AC, R = 0.1, σ_a= 800 MPa at RT, group faceting through clusters of α_p, (b) D10/ WQ, R = 0.1, σ_a= 950 MPa, 450 ℃, stepwise facets.

The second type of FCN could be described as stepwise facets, as demonstrated in Fig. 4.29.b. A series of facets with the width around 20 µm are aligned layer by layer, and normal to the load axis. With the assistance of EDX, the composition of the facets are determined to be similar to that of α_p grains shown in Fig. 29.a, which consists of approximately 90 wt. % Ti and 2 wt. % Mb. (although the content of the Al, Sn and Zr decrease too, but not so drastic as

Mb). As the geometry could not correspond to rational α component in D10 structures, it is supposed that these facets might belong to some local inhomogeneous α entity. This type of FCN is in agreement with the proposition of A. Pilchak [108] for fully lamellar structure of Ti-64 at R = 0.1. V. Sinha [109,110] also proposed that the facets or steps have basal or ‘‘near” basal orientation. This means that the <c> direction ([0001]) in the hcp crystal is either parallel or nearly parallel to the facet normal direction. Terraces or steps interlinking the facets are suggested to be prismatic planes. As shown schematically in Fig. 4.30 [108], the low angle facets parallel to the basal plane are not favorably oriented for slip, but these still allow for low Schmidt-Factors. The series of steps produce a fracture plane that deviates from the basal plane.

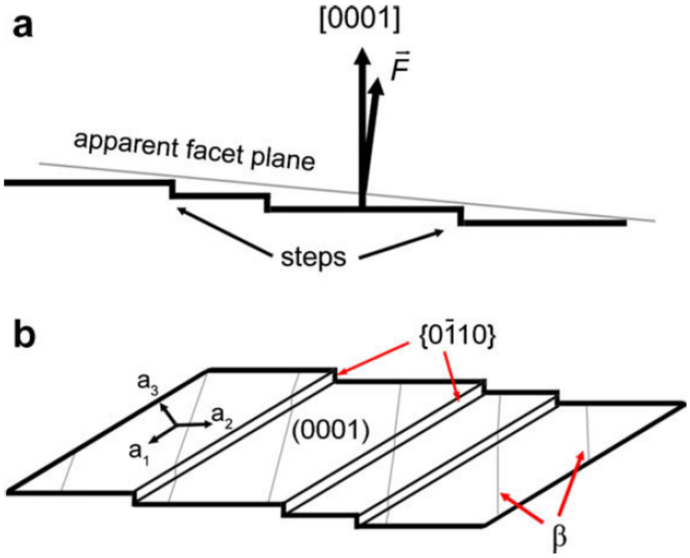

Figure 4.30 A schematic of stepwise facets (a) Basal plane normal and load direction normal to the facet plane are designated by [0001] and $\bar{F}$, respectively, (b) Steps are generally parallel to one of the <a> slip directions.

The PC structures show a variety of subsurface initiating cracks. Fig. 4.31.a displays the first type of initiation site with an array of similarly oriented lamellae-shaped grooves. The widths of the groove are around 1 µm, corresponding to the width of α_p plates. EDX measurement confirmed an elemental composition in the grooves consistent with the bulk material. This infers that the grooves are built up by tearing out the array of α_p plates from the transformed β matrix. In another word, the crack originates at the interface between α_p and transformed β matrix. The cracking is thought to be accomplished by prismatic slip ($[10\bar{1}0]$) which is parallel to the interface [111,112]. The second type of crack initiation is illustrated in Fig.

4.31.b. A transgranularly fractured layer marked by the arrow is located at the center of the initiation site. The width of the layer at around 5 μm is accordant to that of GB α. As reported, the GB α is softer and weaker in strength than the transformed β matrix [92]. Dislocation tends to pile up at GB α, and causes stress concentration, which results in early crack nucleation. Another noticeable feature of the crack nucleation site of PC structure is the presence of large facets at the size around 100 μm (Fig. 4.31.c). Similar subsurface initiating crack characteristics are found by K. Tokaji [59] in Ti-15Mo-Zr-3Al at R = 0. These kind of large facets appear to be associated with GB α. As aforementioned, the weak GB α is more vulnerable to crack nucleation.

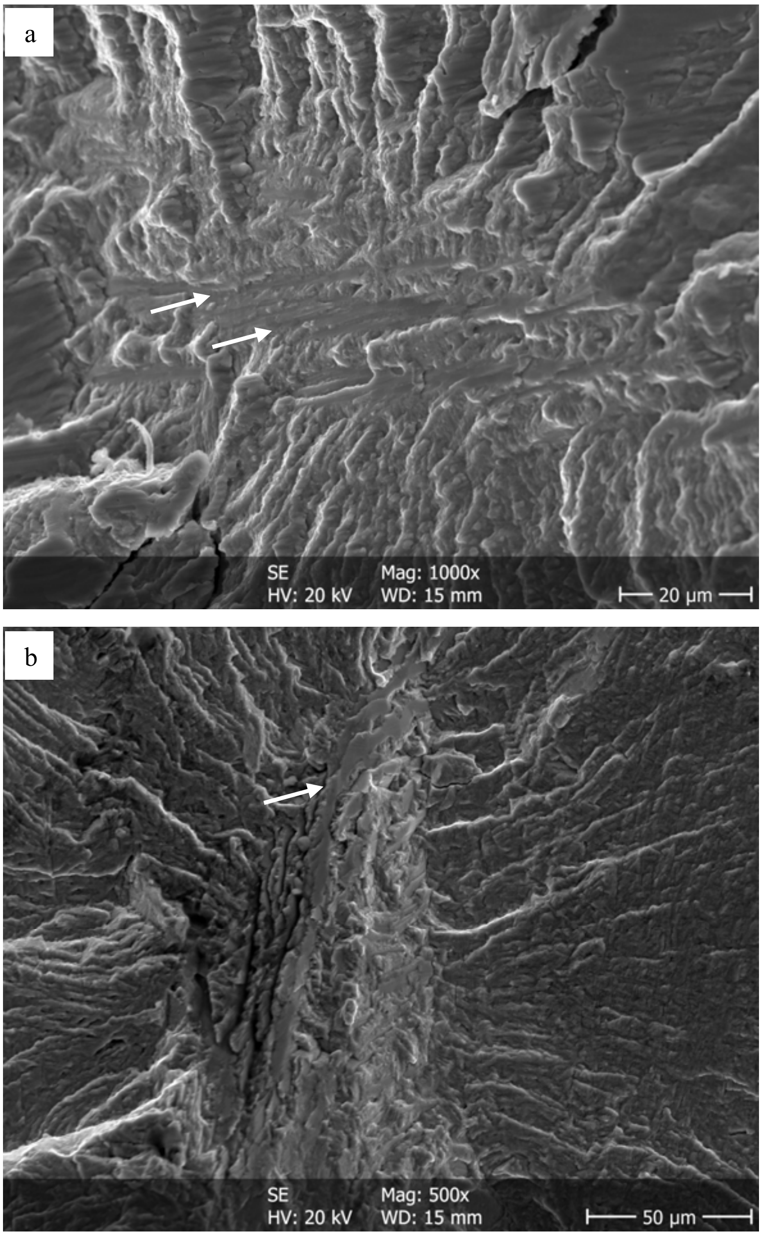

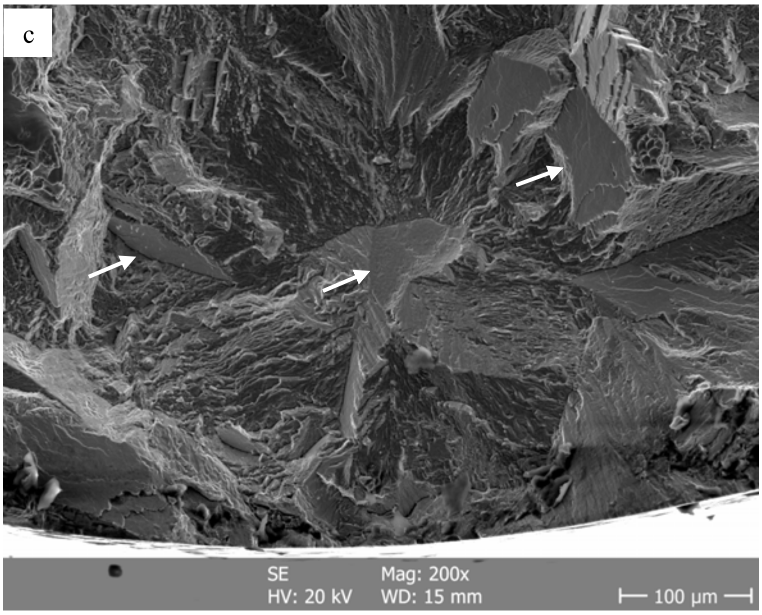

Figure 4.31 various subsurface FCN modes in PC: (a) PC/ AC, 450 ℃, R = -1, 500 MPa, (b) PC/ AC, 450 ℃, R = 0.1, σ_{max} = 850 MPa, (c) Ti-6246 PC/ WQ, RT, R = -1, σ_a = 650 MPa.

In addition, an example of fracture with multi-subsurface initiating cracks is shown in Fig. 4.32. The nucleus of the fatal crack (Fig. 4.32.b) in the form a large facet is similar to those in 4.31.c. They are supposed to be produced by GB α cracking. The secondary crack in Fig. 4.32.c has a stepwise morphology resembling Fig. 4.29.b. for D10. The contents of Ti and Mb at the facets are identified using EDX as 88 % and 3 %, respectively. This could help confirm that the facets originate from transgranular fracture in α_p grains. Various structural components compete in crack initiation and propagation. It is obvious that a multi-competing FCN is operative. This seems an outcome of more complex structures of PC in comparison with D10, since it includes not only α_p and transformed matrix but also GB α.

Generally, FCN demonstrates prominent dependence on local microstructures. PC structures show more variants in nucleation modes than D10. This might be owed to its more complicated structural components in PC, such as the GB α which is absent in D10.

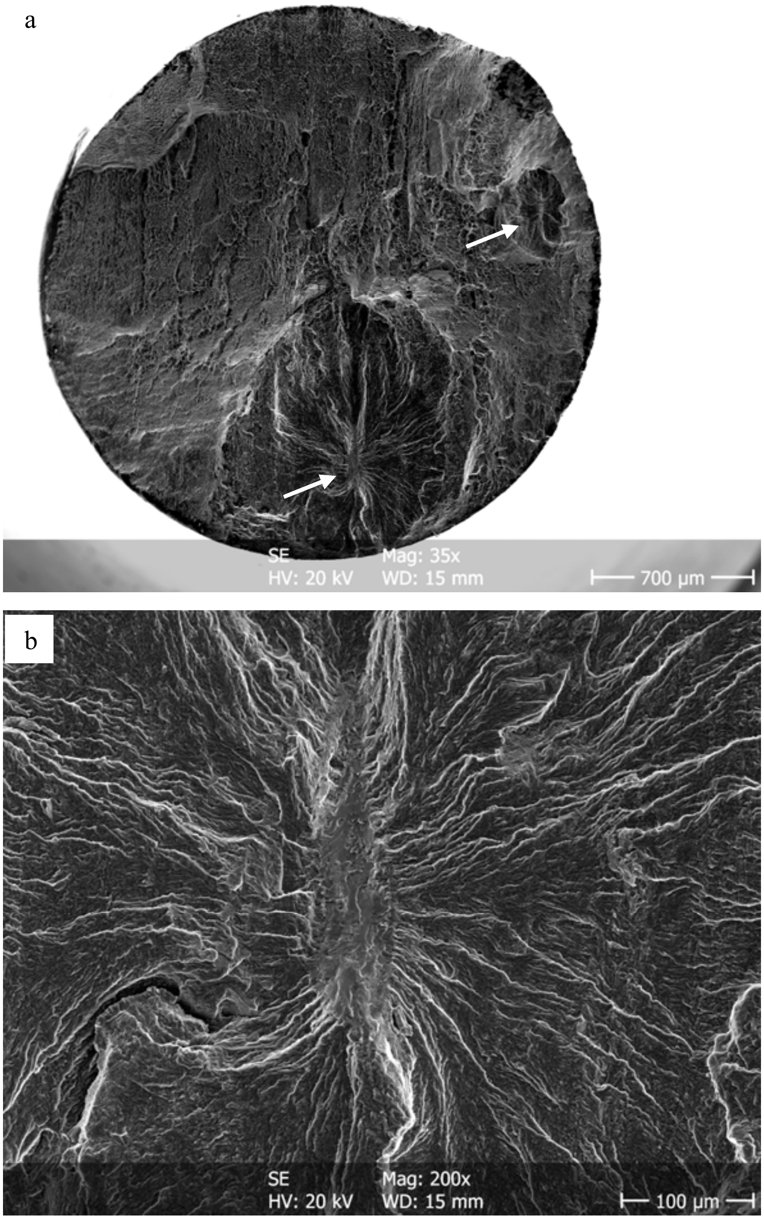
a
SE
Mag: 35x
HV: 20 kV
WD: 15 mm
700 µm
b
SE
Mag: 200x
HV: 20 kV
WD: 15 mm
100 µm

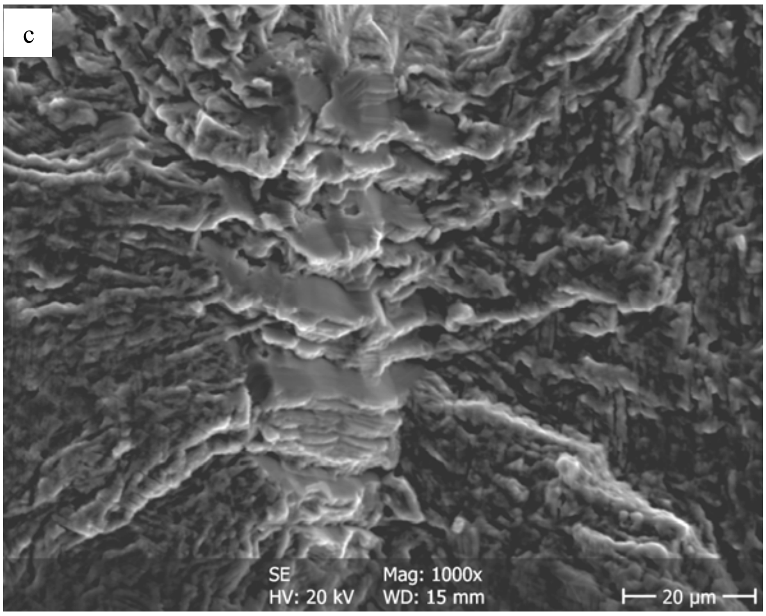

Figure 4.32 Multi-competing FCN in Ti-6246 PC/ AC, 450 ℃, R = 0.1, $\sigma_a = 900$ MPa: (a) two nucleation sites both with long axis parallel to strips in the fatal fracture region, (b) the fatal crack, (c) the secondary crack.

4.6.3 Effect of SP

For peened specimens fatigued at RT, subsurface initiating cracks are widely found at the whole stress amplitude regime, unlike those of unpeened ones with presence only at lower stress regime. It is evident that surface crack initiation is suppressed due to the maximum residual compressive stress at the surface induced by SP, although the surface roughness increases after SP. The crack nucleation site is shifted to the interior of the material where retardation effect of residual compressive stress on microcrack propagation is less significant due to decrease of the residual stress as the depth increases.

A fracture surface of D10/ AC fatigued at 600 MPa was presented in Fig. 4.33. The depth of the crack nucleus beneath the surface was measured to be approximately 270 μm. Regarding to the residual stress-depth profile of D10/ AC in Fig. 4.14.b and its life cycles of 3815063 (Fig. 4.24.b), the residual stress could be estimated around -120 MPa. The crack nucleates at the compressive residual stress range. Consequently, a doubt could be raised why the crack does not appear beyond the residual compressive stress zone where residual tensile stress is present, as it could promote crack nucleation. In fact, this presumption is not supported by the results of fractographic study. No crack nucleus deeper than 400 μm was observed. This might be elucidated by superposition of residual stress and applied stress on a certain crystallographic plane favourable for slip.

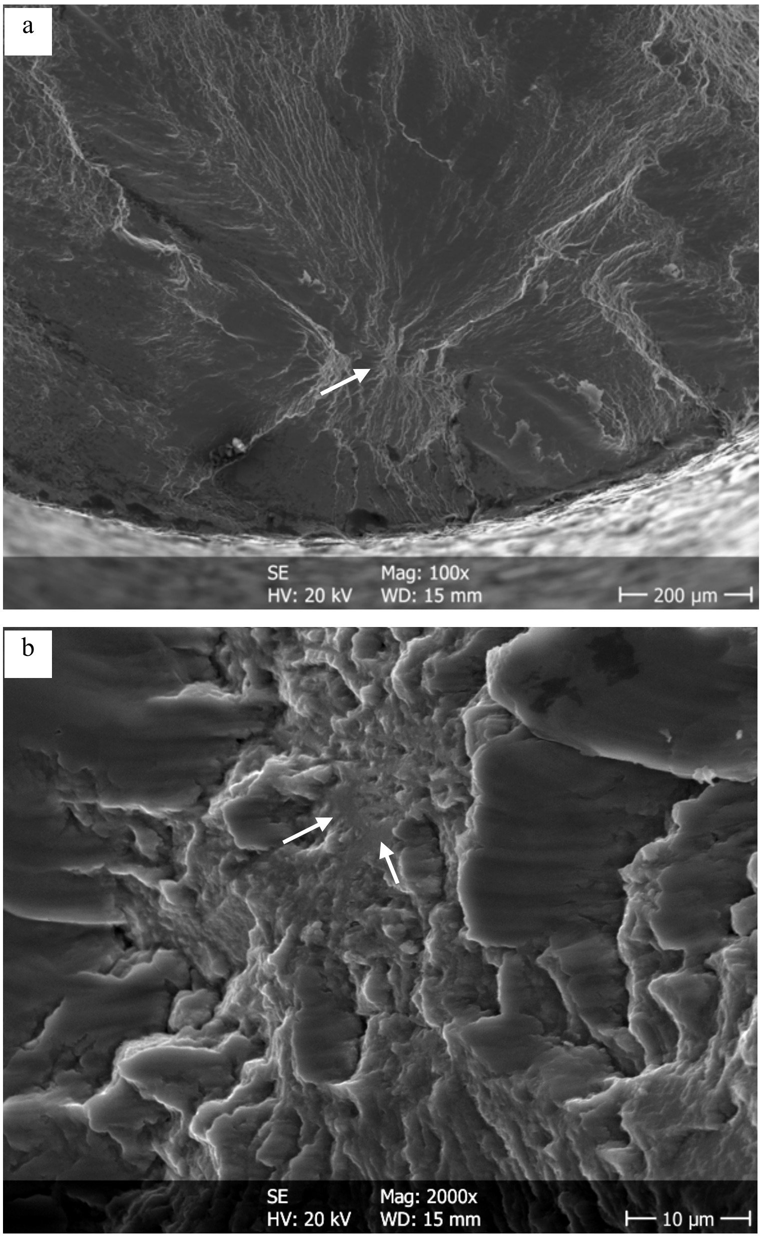

Figure 4.33 Fracture surface of peened D10/ AC, R = -1, σ_a= 600 MPa, RT. (a) crack location, (b) crack nucleus at a small scale α_p agglomerate.

Fig. 4.33.b presents a micrograph of the crack nucleus with high magnification. The origin of crack marked by the arrows resembles α_p present in Fig. 4.29.a. It comprises of two agglomerated α_p. EDX analysis confirmed its identity as α_p agglomerate with 88.3 wt. % Ti and 2.4 wt. % Mo. So the crack originates within α_p grains. This kind of agglomerate could be viewed an α_p grain with over average grain size. From the micrograph, it also could be seen that these two α_p gains share similar faceting angles. Its over average size contributes to an increase in slip length which could result to higher mobility of the associated slip systems. This could also be included into the ‘supergrain’ concept, which is composed of clusters of

similarly oriented grains. ‘Supergrains’ are reported to be more susceptible to fatigue crack initiation because localized deformation in one grain could be more easily accommodated in adjacent grains owing to their similar crystallographic orientation [113,114].

With the increase of testing temperature to 450 ℃, subsurface FCN is seldom observed. Cracks incline to initiate at the surface, although half of the maximum residual compressive stresses are preserved at peened surfaces even after thermal exposure for 55.6 h (Fig. 4.14). The shift of crack initiation sites from subsurface region at RT to surface at elevated 450 ℃ involves concern about the influence of the other surface properties changed by SP, such as roughness. As seen from Fig. 4.12, SP incurred an increase in roughness values, which suggested a higher probability of surface crack occurrence due to micro-notch and stress concentration effect at the notch roots. The rare occurrence of subsurface cracks indicates an overwhelming influence of the increased roughness in acceleration of crack nucleation at the surface. It is supposed that there may exist a competition between the effect of roughness and residual stress. At RT, residual stress excels. While at elevated temperature, benefit of half relaxed residual compressive stresses is no more influential than the deteriorated surface finish.

4.6.4 Fish eye effect

As mentioned in 4.6.1 fish eyes appear in company with internally initiating fatigue cracks, but subsurface FCN does not necessarily coexist with fish eye. The essence of fish eye is the transition of crack growth morphology resulting from shift in crack propagation modes. A fracture surface of a specimen that failed from subsurface initiating crack is presented in Fig. 4.34.a. An ellipsoidal fish eye occurs at the fracture surface. The crack nucleus is located 520 μm beneath the specimen surface. The long axis of the ellipsoid is aligned with the rolling direction of the specimen. This special shape is probably related to texture which might result in a higher crack growth rate along the rolling direction. High magnification image of position 1 at the fish eye boundary in Fig. 4.34.a is presented in Fig. 4.34.b. The dashed line defines the border of the fish eye. Within the fish eye (left side of the dashed line), fine dimples and protuberant bulbs show up with size at around 3 μm, correspondent to that of α_p. Hence, it could be concluded that crack grows intergranularly within fish eye. After the crack reaches the specimen surface, the fracture surface turns agglomerate which appears much coarser than in the fish eye. But the growth mode is not clearly identified. Fig. 4.34.c shows the location 2 in Fig. 3.34.a. The morphology of crack growth in fish eye (below the dashed lines in Fig. 3.34.c) is intergranular. After the crack arrives at the specimen surface, faceted fracture surface turns up outside of the fish eye. The crack growth shifts to transgranular mode. A prerequisite has to be mentioned that the crack proceeds from the nucleus in each direction simultaneously. So each point at the fish eye boundary (i.e. the transition of crack growth mode) arises at the same time.

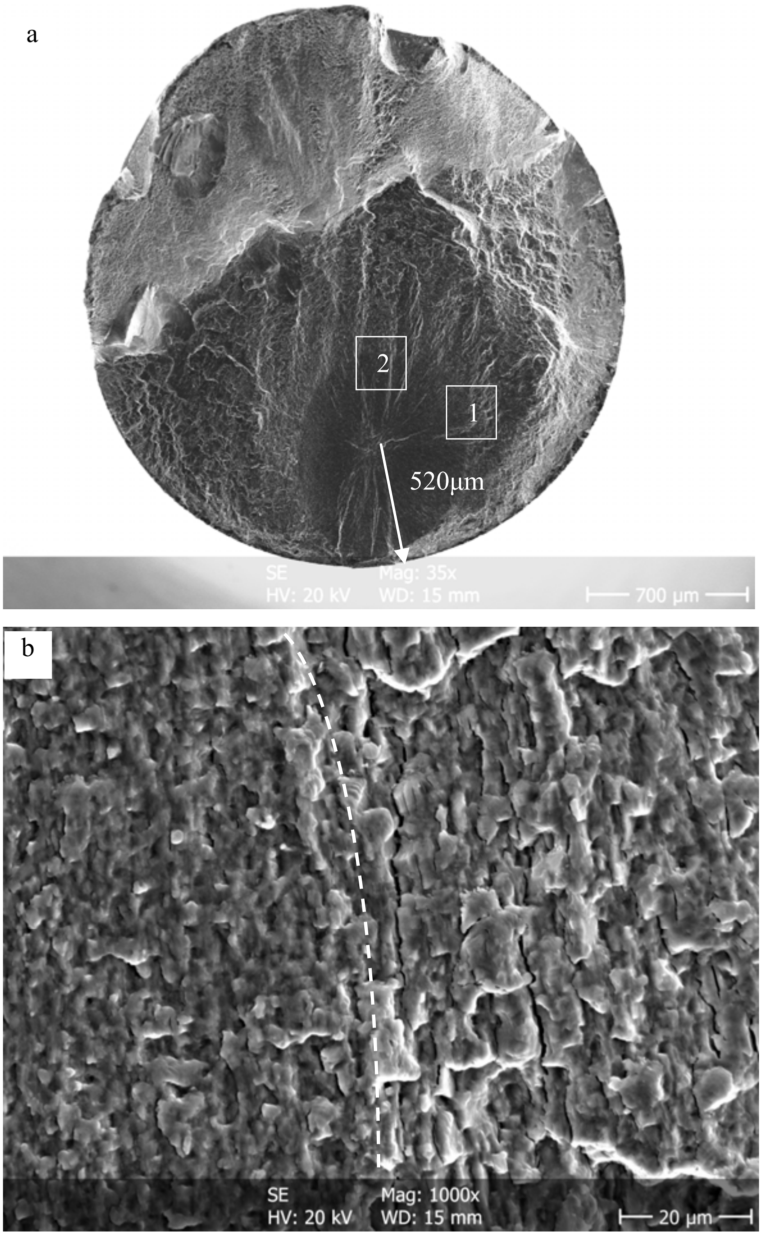

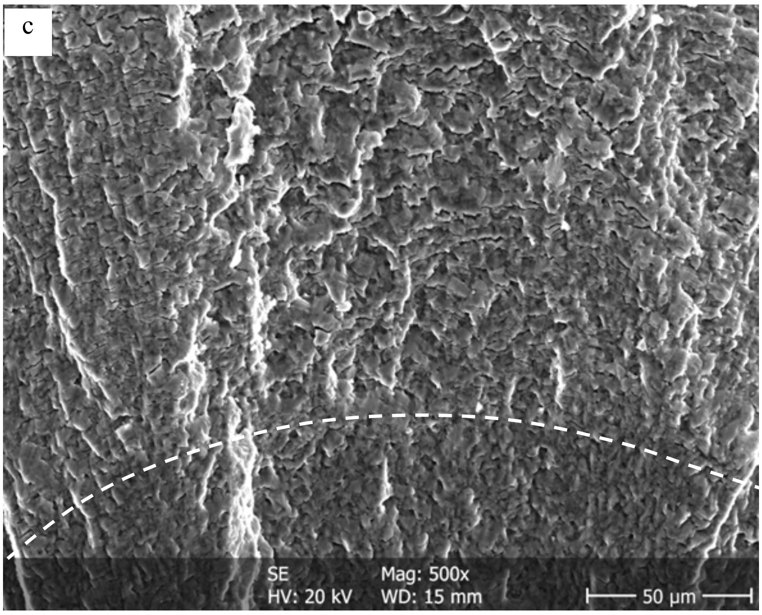

Figure 4.34 (a) Fracture surface of D10/ AC EP, R = -1, σ_a = 600 MPa, 450 ℃, N_F = 377039. (b) high magnification image of fish eye boundary at position 1, (c) high magnification image of fish eye boundary at position 2.

Whereas M.J. Caton [96] observed reversed transition mode of fish eye in Ni-base super alloy IN100, they reported that once the crack front is exposed to air, the fractography indicates an immediate shift from transgranular crack growth mode to fully intergranular mode. The reason for the transition is attributed to environmentally assisted embrittlement of grain boundaries. They proposed that exposure to air after the crack reached specimen surface could lead to the formation of brittle species along the grain boundary such as Nb-oxides layers. Thus brittle decohesion along the grain boundary results in the intergranular fracture with higher crack growth rate outside of the fish eye.

Although there have been limited studies on the mechanism of fish eye in Ti alloys, some observation about fish eye at different environmental or loading conditions could help exclude some influence factors and narrow searching window for possible causes. J. Mendez et al. [101] found undefined fish eye features at the fracture surface of low cycle fatigued Ti-6246 in vacuum (~5×10^{-4} Pa), where crack growth is not exposed to air at all. In addition, an evident half fish eye (fan shaped zone) was observed by G. Jago [100] at a fracture surface failed from a surface initiating crack. Both of two cases do not involve environmental variation while crack propagates. Therefore, a conclusion could be drawn that the mechanisms of fish eye and the shift of crack initiation site from the surface to the bulk in Ti-6246 are not related to environment. It is presumed that unbalance in load distribution due to reduction in effective load-carrying area of specimen during crack propagation might have an impact on crack growth mode transition. However it is still difficult to explain why fish eye does not accompany each crack. The explanation might be found through more investigation in depth about the local damage mechanisms.

5. Conclusions

1. By means of TMP, various microstructures are generated. The phase evolution of Ti-6246 during different cooling rate (WQ and AC) from crystallization and final aging was investigated. Martensitic transformation occurs during WQ from 920 ℃, resulting in α″. AC leads to a partial transformation from β to α. After aging, in comparison to AC condition, WQ condition shows a higher α_s percentage via decomposition of α″. This indicates a more significant precipitation in WQ than AC condition during aging.
2. For TIMETAL-54M, EQ structure shows highest fatigue strength among the air cooled conditions due to the competing mechanism between AEPE and α colony size effect. While among different structures of Ti-6246, D10 exhibits higher fatigue strengths than D30 and β annealed. Based on the as-received condition, the increases of strengths reach 50 and 125 MPa in AC and WQ conditions, respectively. The cause derives from the absence of α colony size effect in duplex structures of Ti-6246, because the matrix are fine particulates, which could even lead to improvement in strength due to grain refinement. Besides, most of the WQ conditions display advantages in both tensile strengths and HCF, comparing to the correspondent AC structures. The reason could be interpreted by the more prominent α_s precipitation hardening resulting from decomposition of α″ in WQ conditions.
3. Two alloys are highly sensitive to loading mode. Fatigue strengths at axial load are around 200 MPa lower than those at R-B load. Owing to the stress gradient in the specimens at R-B load, the control volume at this mode is only the region at the surface layer, much smaller than that at axial load, which covers the whole cross section. It implies higher probability of cumulative damage resulting from both surface and bulk structural discontinuities in axial load than in R-B.
4. Means stress sensitivities of the two alloys are proven to be normal, regardless of temperature. Fatigue limits at $R = 0.1$ is markedly higher than those at $R = -1$.
5. Increase in testing temperature from RT to 450 ℃ results in maximum 50 MPa decrease in HCF strengths of Ti-6246. The thermal stability of Ti-6246 in HCF is satisfactory.
6. The material shows greatly enhanced HCF performance in vacuum, comparing to that in laboratory air. The enhancement in vacuum could be attributed to the validation of reversible slip along slip bands and the internal heating, both of which slow down crack propagation rate.

7. SP induces deterioration in surface finish and a mild work hardening effect. The work-hardenability of AC condition is more prominent than WQ condition, because the latter is highly strengthened during the TMP by virtue of stronger α_s precipitation. SP-induced residual compressive stresses reach maximum 970 MPa in D10/ WQ and 910 MPa in D10/ AC at 20 μm beneath the surfaces. D10/ AC shows higher stability than D10/ WQ in both cold work and residual stress. After preheat to 450 ℃, the relaxation of residual compressive stresses are 50 % and 41 % for D10/ WQ and D10/ AC, respectively. Residual stress relaxation stops after preheat plus 1 h soaking at 450 ℃. Afterwards, the maximum residual compressive stresses are stabilized at 520 MPa in D10/ AC and 450 MPa in D10/ WQ. The thermal stability of residual compressive stress is higher in AC than in WQ, which is in agreement with the tendency of cold work in these two microstructures.
8. Generally SP could introduce an improvement of 50 MPa in HCF at RT, resulting from the promotion in resistance to crack initiation and propagation due to SP-induced residual compressive stresses at surface layers of specimens. At 450 ℃, fatigue behavior of SP deteriorated at high stress amplitude regime, probably due to the overwhelming negative effect of the increased roughness against the partially relaxed residual compressive stresses.
9. FCN at subsurface region in EP condition is commonly observed within conventional fatigue (~10^7 cycles) at axial load, despite of load ratio, temperature and atmosphere. The likelihood of subsurface crack nucleation was found to increase with the decrease of stress levels. Multi-competing crack nucleation mechanisms were confirmed operative in different microstructures. Crack nucleation was strongly dependent of local microstructural configurations. Four crack nucleation modes were identified, including transgranular initiation by synergistic faceting across clusters (macrozones), agglomerates of primary alpha grains, prior beta grain boundary alpha and intergranular nucleation along the interface between α_p and matrix.
10. Fish eyes effect is present in Ti-6246. It is observed that there is a transition of FCP mode from intergranular within fish eye to transgranular outside of it. Mechanism of fish eye in Ti-6246 is not related to environment. It is presumed that unbalance in load distribution due to reduction in effective load-carrying area of specimen during crack propagation might have an impact on FCP mode transition. More in depth investigation is needed.

References

[1] W.J. Kroll, How commercial titanium and zirconium were born, Journal of the Franklin Institute 260 (1955) 169–192.

[2] H.B. Bomberger, F.H. Froes, P.H. Morton, Titanium Technology: Present status and future trends, 1985, p. 3.

[3] G. Lüterjing, J.C. Williams, Titanium, Springer, 2003.

[4] C. Leyens, M. Peters, Titanium and titanium alloys: Fundamentals and applications, WILEY-VCH; John Wiley, Weinheim, 2003.

[5] I. Bhavan, C. Lines, Indian minerals yearbook 2011 (Part II) 50^{th} Edition Ilmenite & Rutile, 2012.

[6] S. Fox, K.-O. Yu, Recent changes and developments in Titanium extraction, in: L. Zhou, H. Chang, Y. Lu, D. Xu (Eds.), Ti-2011, Titanium science and technology, Science Press Beijing, 2012, pp. 65–70.

[7] G.M. Bedinger, 2011 minerals Yearbook, Titanium. (U.S. Department of interior and U.S. Geological survey (USGS), 2013.

[8] J. Geiger, Titanium mineral feedstocks history and future trends, in: Titanium 2010 Proceedings, 2010.

[9] U.S. Department of interior and U.S. Geological survey (USGS), Mineral commodity summaries 2012, 2012, pp. 172–175.

[10] P. Dewhurst, Titanium sponge supply, past, present and future, in: Titanium 2013, Oct. 2013.

[11] L. Zhou, H. Chang, X. Wang, Recent progress of titanium industry, research and development in China, in: L. Zhou, H. Chang, Y. Lu, D. Xu (Eds.), Ti-2011, Titanium science and technology, Science Press Beijing, 2012, pp. 56–61.

[12] G.M. Bedinger, Mineral Industry Surveys, Titanium in the second quarter 2013. U.S. Geological Survey, 2013.

[13] G. Welsch, R. Boyer, E. Collings, Materials properties handbook: titanium alloys, ASM International, 1994.

[14] Y. Kosaka, J. Fanning, S. Fox, Development of low cost high strength alpha/beta titanium alloy with superior machinablility, in: 10th World Conference on Titanium Ti-2003, 2003, pp. 102–108.

[15] Y. Kosaka, S.P. Fox, Influences of alloy chemistry and microstructure on the machinability of titanium alloys, in: Cost Affordable Titanium, TMS, 2004, pp. 169–176.

[16] M. Armendia, A. Garay, L.-M. Iriarte, P.-J. Arrazola, Comparison of the machinabilities of Ti6Al4V and TIMETAL® 54M using uncoated WC–Co tools, Journal of Materials Processing Technology 210 (2010) 197–203.

[17] V. Venkatesh, Y. Kosaka, J. Fanning, S. Nyakana, Processing and Properties of TIMET-54M, in: M. Niinomi (Ed.), Ti-2007 science and technology: proceedings of the 11th world conference on tianium (JIMIC5), Japan Institute of Metals, 2007, pp. 713–716.

[18] M.J. Donachie, Titanium: A Technical Guide, ASM International, 1998.

[19] J.C. Williams, B.S. Hickman, Tempering behaviour of orthorhombic martensite in titanium alloys, Metallurgical Transaction 1 (1970) 2648–2650.

[20] R.A. Spurling, C.G. Rhodes, J.C. Williams, The microstructure of Ti alloys as influenced by thin-foil artifacts, Metallurgical Transactions 5 (1974) 2597–2600.

[21] M. Young, E. Levine, H. Margolin, The aging behaviour of orthorhombic martensite in Ti-6-2-4-6, Metallurgical Transactions 5 (1974) 1891–1898.

[22] S. Bein and J. Bechet, Phase transformation kinetics and mechanisms in titanium alloys Ti-6.2.4.6, β-CEZ and Ti-10.2.3, Journal de Physique IV, Collogue C1, supplement au Journal de Physique III 6 (1996) 99–108.

[23] W.J. Evans, Optimising mechanical properties in alpha + beta titanium alloys, Materials Science and Engineering A 243 (1998) 89–96.

[24] S. Nischijima, K. Kanazawa, Stepwise S-N curve and fish-eye failure in gigacycle fatigue, Fatigue Fract Engng Mater Struct. 22 (1999) 601-607.

[25] C.J. Mchargue, The crystallography of the titanium transformation, Acta Cryst. 6 (1953) 529–530.

[26] H.W. Rosenberger, The science, Technology and Application of Titanium, Pergamon Press, 1970.

[27] G. Lütjering, J. Albrecht, C. Sauer, T. Krull, The influence of soft, precipitate-free zones at grain boundaries in Ti and Al alloys on their fatigue and fracture behavior, Materials Science and Engineering: A 468-470 (2007) 201–209.

[28] W.D. Callister, D.G. Rethwisch, Fundamentals of materials science and engineering: An integrated approach, 4th ed., Wiley, Hoboken, N.J, 2012.

[29] P.G. Partridge, The crystallography and deformation modes of hexagonal close-packed metals, Metallurgical Reviews 12 (1967) 169–194.

[30] M.H. Yoo, Slip, twinning, and fracture in hexagonal close-packed metals, Metallurgical Transactions A 12A (1981) 409–418.

[31] R.I. Jaffee, H.M. Burte, Titanium Science and Technology, Springer, New York, USA, 1973.

[32] I. Jones, W. Hutchinson, Stress-state dependence of slip in Ti-6Al-4V and other H.C.P. metals, Acta Metallurgica 29 (1981) 951–968.

[33] N.E. Paton, R.G. Baggerly, J.C. Williams, Deformation behavior of HCP Ti-Al alloy single crystals. Report, Metallurgical and Materials Transactions A 33 (2002) 837–850.

[34] W. Pearson, Handbook of lattice spacings and structures of metals and alloys, Pergamon Press, London, UK, 1958.

[35] G. Lütjering, Influence of processing on microstructure and mechanical properties of (α + β) titanium alloys, Materials Science and Engineering: A 243 (1998) 32–45.

[36] G. Lütjering, Property optimization through microstructural control in titanium and aluminum alloys, Materials Science and Engineering: A 263 (1999) 117–126.

[37] T. Ahmed, H. Rack, Phase transformations during cooling in α + β titanium alloys, Materials Science and Engineering: A 243 (1998) 206–211.

[38] F. Gil, J. Manero, M. Ginebra, J. Planell, The effect of cooling rate on the cyclic deformation of β-annealed Ti–6Al–4V, Materials Science and Engineering: A 349 (2003) 150–155.

[39] G. Lüterjing, J. Albrech, O.M. Ivasishin, Microstructure/ property relationship of titanium alloys, TMS, Warrendale, PA, 1994.

[40] S. Yang, Z. Wu, K. Zay, Y. Kosaka, L. Wagner, Effects of thermo-mechanical treatments on microstructures and mechanical properties: TIMETAL 54M vs. Ti-6Al-4V, in: L. Zhou, H. Chang, Y. Lu, D. Xu (Eds.), Ti-2011, Titanium science and technology, Science Press Beijing, 2012, pp. 984–988.

[41] R.K. Nalla, B.L. Boyce, J.P. Campbell, J.O. Peters, R.O. Ritchie, Influence of microstructure on high-cycle fatigue of Ti64: bimodal vs. lamellar structure, Metallurgical and Materials Transactions A 33 (2002) 899–918.

[42] J. Schijve, Fatigue of structures and materials, 2nd ed., Springer, Dordrecht, London, 2008.

[43] Y. Murakami, M. Endo, Effects of defects, inclusions and inhomogeneities on fatigue strength, International Journal of Fatigue 16 (1994) 163–182.

[44] M. Torres, An evaluation of shot peening, residual stress and stress relaxation on the fatigue life of AISI 4340 steel, International Journal of Fatigue 24 (2002) 877–886.

[45] H. Itoga, Effect of surface roughness on step-wise S–N characteristics in high strength steel, International Journal of Fatigue 25 (2003) 379–385.

[46] J. Zhang, S. Li, Z. Yang, G. Li, W. Hui, Y. Weng, Influence of inclusion size on fatigue behavior of high strength steels in the gigacycle fatigue regime, International Journal of Fatigue 29 (2007) 765–771.

[47] K. Shiozawa, Y. Morii, S. Nishino, L. Lu, Subsurface crack initiation and propagation mechanism in high-strength steel in a very high cycle fatigue regime, International Journal of Fatigue 28 (2006) 1521–1532.

[48] Y. Liu, Z. Yang, Y. Li, S. Chen, S. Li, W. Hui, Y. Weng, On the formation of GBF of high-strength steels in the very high cycle fatigue regime, Materials Science and Engineering: A 497 (2008) 408–415.

[49] J.M. Hyzak, M. Bernstein, The effect of defects on the fatigue crack initiation process in two P/ M superalloys: Part II. Surface-subsurface transition, Metallurgical Transactions A 13 (A) 45–52.

[50] M.M. Shenoy, Constitutive modelling and life prediction in Ni-base superalloys, PhD thesis, Georgia Institute of Technology, Atlanta, USA, 2006.

[51] J. Miao, Very high cycle fatigue behaviour of nickel-based superalloy Rene 88DT, PhD thesis, University of Michigan, Ann Arbor, USA, 2010.

[52] X.-F. Ma, Z. Duan, H.-J. Shi, Fatigue and fracture behaviour of nickel-based superalloys Inconel 718 up to very high cycle regime, Journal of Zhejiang University Science A 11 (2010) 727–737.

[53] M. Nakajima, K. Tokaji, H. Itoga, T. Shimizu, Effect of loading condition on very high cycle fatigue behavior in a high strength steel, International Journal of Fatigue 32 (2010) 475–480.

[54] Y. Murakami, S. Kodama, S. Konuma, Quantitative evaluation of effects of non-metallic inclusions on fatigue strength of high strength steels. I: Basic fatigue mechanism and evaluation of correlation between the fatigue fracture stress and the size and location of non-metallic inclusions, International Journal of Fatigue 11 (1989) 291–298.

[55] Y. Murakami, N.N. Yokoyama, J. Nagata, Mechanism of fatigue failure in ultralong life regime, Fatigue Fract Engng Mater Struct. 25 (2002) 735–746.

[56] J. Lindemann, Mechanische Eigenschaften von Lamellar- und Duplexgefügen der Hochtemperaturtitanlegierung TIMETAL 1100. PhD thesis, BTU-Cottbus, Cottbus, Germany, 1998.

[57] L. Susmel, R. Tovo, P. Lazzarin, The mean stress effect on the high-cycle fatigue strength from a multiaxial fatigue point of view, International Journal of Fatigue 27 (2005) 928–943.

[58] S. Adachi, L. Wagner, G. Lütjering, Influence of mean stress on fatigue strength of Ti-6Al-4V, in: Proceedings of the 7th International Conference on the Strength of Metals and Alloys (ICSMA 7), 1986, pp. 2117–2122.

[59] K. Tokaji, H. Kariya, Mean stress dependence of fatigue strength and subsurface crack initiation in Ti–15Mo–5Zr–3Al alloy, Materials Science and Engineering: A 281 (2000) 268–274.

[60] S. Suresh, Fatigue of materials, Cambridge university press, New York, 2004.

[61] S. Adachi, L. Wagner, G. Lüterjing, Influence of mean stress on fatigue crack nucleation in (alpha + beta) Ti-alloys, in: Proceedings of international conference on fatigue of engineering materials and structures, 1986.

[62] Lindemann,,J., L. Wagner, Mean stress sensitivity in fatigue of α, (α + β) and β titanium alloys, Materials Science and Engineering: A 234-236 (1997) 1118–1121.

[63] L. Lindemann, A. Berg, L. Wagner, Mean Stress Sensitivity of the HCF Strength in TIMETAl 1100: Microstructural Effects, in: G. Lütjering, H. Nowack (Eds.), Fatigue '96: Proceedings of the Sixth International Fatigue Congress, 6-10 May 1996, Berlin, Germany, Pergamon, Tarrytown, N.Y, 1996.

[64] L. Rémy, A. Pineau, B. Thomas, Temperature dependence of stacking fault energy in close-packed metals and alloys, Materials Science and Engineering 36 (1978) 47–63.

[65] D.J. Duquette, Environmental effects I: General fatigue resistance and crack nucleation in metals and alloys, Fatigue and Microstructure (1979) 335–363.

[66] T.K. Heckel, H.-J. Christ, Isothermal and thermomechanical fatigue of titanium alloys, Procedia Engineering 2 (2010) 845–854.

[67] J. Zuo, Z. Wang, E.H. Han, Fatigue Behaviour of Ti-6Al-4V Alloy in vacuum and at low Temperature, AMR 41-42 (2008) 83–90.

[68] C. Sarrazin-Baudoux, J. Petit, Environmental effects on near-threshold fatigue crack propagation on a Ti6246 alloy at 500 ℃, European Structural Integrity Society 29 (2002) 227–236.

[69] S. Biker, Shot peening: a dynamic application and its future, MFN-Metal Finishing News, 2006.

[70] P. Hutmann, The application of mechanical surface treatment in passenger car industry, in: L. Wagner (Ed.), Shot peening, WILEY-VCH, Weinheim, 2003, pp. 3–12.

[71] L. Wagner, Mechanical surface treatments on Titanium alloys: Fundamental mechanisms, in: J.K. Gregory, H.J. Rack, D. Eylon (Eds.), Surface performance of titanium: Proceedings of a Symposium on Surface Performance of Titanium, Minerals, Metals & Materials Society, Warrendale, Pa, 1996, pp. 199--215.

[72] J. Hack, G. Leverant, Influence of compressive residual stress on the crack-opening behaviour of part-through fatigue cracks, in: Residual stress effects in fatigue, ASTM, Philadelphia, 1982, pp. 204–223.

[73] J. Hack, G. Leverant, Fatigue microcrack behaviour under the influence of surface residual stresses, Interim report on contract N00014-78-C-06074, Southwest research institute, San Antonio, USA, 1982.

[74] D. Löhe, K.-H. Lang, O. Vöhringer, Residual stress and fatigue behaviour, in: G.E. Totten, Howes, Maurice A. H, T. Inoue (Eds.), Handbook of residual stress and deformation of steel, ASM International, Materials Park, OH, 2002, pp. 27–53.

[75] T. Ludian, L. Wagner, Mechanical surface treatments for improving fatigue behaviour in titanium alloys, Advances in Materials Sciences 8 (2008) 44–52.

[76] J. Müller, H.J. Rack, T. Ludian, L. Wagenr, Microstructureal and mean stress effects in fatigue performance of shot peened Ti-6Al-4V, in: M. Niinomi (Ed.), Ti-2007 science and technology: Proceedings of the 11th World Conference on Titanium (JIMIC5), Japan Institute of Metals, Sendai, Japan, 2007, pp. 375–378.

[77] K. Zay, S. Yang, Y. Kosaka, L. Wagner, Shot peening and ball-burnishing to improve HCF strength of the new titanium alloy TIMETAL-54M, in: J. Champaigne (Ed.), Proceedings of 11th international conference on shot peening, 2011, p. 303.

[78] K. Zay, E. Maawad, H.-G. Brokmeier, L. Wagner, C. Genzel, Influence of mechanical surface treatments on the high cycle fatigue performance of TIMETAL 54M, Materials Science and Engineering: A 528 (2011) 2554–2558.

[79] H. Polanetzi, J. Ehrl, I. Stoll, L. Wagner, Influence of surface enhancement processes on mechanical properties of the titanium alloys Ti6246, in: J. Champaigne (Ed.), Proceedings of 11th international conference on shot peening, 2011.

[80] L. Wagner, M. Kocan, T. Ludian, Effect of the various titanium alloy classes on the fatigue response to shot peening, Metal finishing news 5 (2004) 35.

[81] R.C. Mcclung, A literature survey on the stability and significance of residual stresses during fatigue, Fat Frac Eng Mat Struct 30 (2007) 173–205.

[82] T. Krull, Bruch- und Ermüdungsverhalten der β-Titanlegierung Ti-6246 bei sehr hohen Festigkeiten, PhD thesis, Shaker, Aachen, 2007.

[83] L. Wagner, J. Gregory, Thermo-mechanical surface treatment of Titanium alloys, Materials Science Forum (1994) 159–172.

[84] L. Wagner, Mechanical surface treatments on titanium, aluminum and magnesium alloys, Materials Science and Engineering: A 263 (1999) 210–216.

[85] R.O. Ritchie, B. Karihaloo, I. Milne (Eds.), Comprehensive Structural Integrity, Elsevier Science & Technology Books, San Diego, 2003.

[86] J. Romualdi, E. Appolonia, Effect of Internal Heating on the Fatigue properties of Titanium, Ft. Belvoir Defense Technical Information Center, 1953.

[87] E. Levine, Deformation Mechanisms in Titanium at Low Temperatures, Transaction AIME 236 (1966) 1558.

[88] M. Sugano, S. Kanno, T. Satake, Fatigue behavior of titanium in vacuum, Acta Metallurgica 37 (1989) 1811–1820.

[89] Z. Ismarrubie, H. Yussof, M. Sugano, Fatigue Damage Mechanism of Titanium in Vacuum and in Air, Procedia Engineering 41 (2012) 1559–1565.

[90] T. Dörr, L. Wagner, Fatigue behaviour of shot peened TIMETAL 1100: Effects of microstructure and stress gradient, in: J.K. Gregory, H.J. Rack, D. Eylon (Eds.), Surface performance of titanium: Proceedings of a Symposium on Surface Performance of Titanium, Minerals, Metals & Materials Society, Warrendale, Pa, 1996.

[91] T. Dörr, L. Wagner, Influence of stress gradient on fatigue behaviour of shot peened TIMETAL 1100, in: J. Champaigne (Ed.), 6th international conference on shot peening, San Francisco, USA, 1996, p. 223.

[92] C. Sauer, G. Lütjering, Influence of α layers at β grain boundaries on mechanical properties of Ti-alloys, Materials Science and Engineering: A 319-321 (2001) 393–397.

[93] K. Zay, Considering Mean Stress and Environmental Effects in Understanding the Fatigue Performance of Mechanically Surface Treated Titanium Alloys, PhD thesis, TU-Clausthal, Clausthal-Zellerfeld, Germany, 2011.

[94] K. Tokaji, J.-C. Bian, T. Ogawa, M. Nakajima, The microstructure dependence of fatigue behaviour in Ti15Mo5Zr3Al alloy, Materials Science and Engineering: A 213 (1996) 86–92.

[95] K. Tokaji, H.-N. Ko, M. Nakajima, H. Itoga, Effects of humidity on crack initiation mechanism and associated S–N characteristics in very high strength steels, Materials Science and Engineering: A 345 (2003) 197–206.

[96] M.J. Caton, S.K. Jha, Small fatigue crack growth and failure mode transitions in a Ni-base superalloy at elevated temperature, International Journal of Fatigue 32 (2010) 1461–1472.

[97] D. McDowell, F. Dunne, Microstructure-sensitive computational modeling of fatigue crack formation, International Journal of Fatigue 32 (2010) 1521–1542.

[98] C. Przybyla, R. Prasannavenkatesan, N. Salajegheh, D.L. McDowell, Microstructure-sensitive modeling of high cycle fatigue, International Journal of Fatigue 32 (2010) 512–525.

[99] S. Adachi, Means stress dependence of fatigue strength in Titanium alloys, PhD thesis, TU-Hamburg-Harburg, Hamburg, Germany, 1987.

[100] G. Jago, J. Bechet, Influence of microstructure of (α + β) Ti-6.2.4.6 alloy on high-cycle fatigue and tensile test behaviour, Fat Frac Eng Mat Struct 22 (1999) 647–655.

[101] J. Mendez, S. Mailly, P. Villechaise, Temperature and environmental effects on low cycle fatigue resistance of Titanium alloys, in: J. Petit, L. Rémy (Eds.), Temperature-fatigue interaction, Elsevier, Amsterdam, 2002, pp. 95–102.

[102] S. Jha, J. Larsen, A. Rosenberger, G. Hartman, Dual fatigue failure modes in Ti–6Al–2Sn–4Zr–6Mo and consequences on probabilistic life prediction, Scripta Materialia 48 (2003) 1637–1642.

[103] V. Sinha, J. Spowart, M. Mills, J. Williams, Observations on the faceted initiation site in the dwell-fatigue tested in Ti-6242 alloy: Crystallographic orientation and size effects, Metallurgical and Materials Transactions A 37A (2006) 1507–1518.

[104] C. Szczepanski, S. Jha, J. Larsen, J. Jones, Microstructural Influences on Very-High-Cycle Fatigue-Crack Initiation in Ti-6246, Metall and Mat Trans A 39 (2008) 2841–2851.

[105] M. Bache, W. Evans, H. Davies, Electron back scattered diffraction (DBSD) analysis of quasi-cleavage and hydrogen induced fractures under cyclic and dwell loading in Titanium alloys, Journal of Materials Science (1997) 3435–3442.

[106] J. Gilbert, H. Piehler, On the nature and crystallographic orientation of subsurface cracks in high cycle fatigue of Ti-6Al-4V, Metallurgical Transactions A 24A (1993) 669–680.

[107] S. Jha, J. Larsen, Random heterogeneity scales and probabilistic description of the long-lifetime regime of fatigue, Technical report, AFRL-RX-WP-TP-2008-4052, Dayton, USA, 2007.

[108] A. Pilchak, A. Bhattacharjee, A. Rosenberger, J. Williams, Low ΔK faceted crack growth in titanium alloys, International Journal of Fatigue 31 (2009) 989–994.

[109] V. Sinha, M. Mills, J. Williams, Crystallography of fracture facets in a near alpha titanium alloy, Metall and Mat Trans A 37 (2006) 2015–2026.

[110] V. Sinha, M.J. Mills, J.C. Williams, Determination of crystallographic orientation of dwell-fatigue fracture facets in Ti-6242 alloy, J Mater Sci 42 (2007) 8334–8341.

[111] H. Tan, H. Gu, C. Laird, N. Munroe, Cyclic deformation behaviour of high purity titanium single crystals: Part I. Orientation dependence of stress-strain response, Metall and Mat Trans A 29A (1998) 507–512.

[112] J. Mayeur, Three dimensional modelling of Titanium-Aluminum alloys with application to attachment fatigue. Master thesis, Georgia Institute of Technology, Atlanta, USA, 2004.

[113] D. Davidson, K. Chan, R. McClung, S. Hudak, Small fatigue cracks, in: R.O. Ritchie, B. Karihaloo, I. Milne (Eds.), Comprehensive Structural Integrity, Elsevier Science & Technology Books, San Diego, July 2003, pp. 129–164.

[114] D.L. Davidson, R.G. Tryon, M. Oja, R. Matthews, K.S. Ravi Chandran, Fatigue Crack Initiation In WASPALOY at 20 °C, Metall and Mat Trans A 38 (2007) 2214–2225.

Curriculum Vitae

Personal information

Surname: Shan
Given name: Yang
Gender: Female
Date of birth: Feb. 21.1984
Place of birth: Wuhan, China
Citizenship: Chinese
Current post address:
Walther-Nernst-Str. 1,
38678, Clausthal-Zellerfeld, Germany
Tel: +49-05323722757
Fax: +49-5323722766
E-mail: sunvening@gmail.com, shan.yang@tu-clausthal.de

Education:

2003-2007	Bachelor degree in thermal energy and power engineering
2007-2009	Master degree in thermal engineering
Since 2009	PhD candidate in materials science and engineering

Professionl experience:

2007-2009	Research assistant at state key laboratory of coal combustion, Wuhan, China
2009-2013	Research fellowship sponsored by China scholarship counsel at institute of materials science and engineering, Clausthal University of Technology, Clausthal-Zellerfeld, Germany
Since 2013	Employed as research assistant at institute of materials science and engineering, Clausthal University of Technology, Clausthal-Zellerfeld, Germany

Name, Vorname: Yang Shan

Datum: 31 Mai, 2014

Eidesstattliche Erklärung

Hiermit erkläre ich an Eides Statt, dass ich die bei der Fakultät für Natur- und Materialwissenschaften der Technischen Universität Clausthal eingereichte Dissertation selbständig und ohne unerlaubte Hilfe verfasst und die benutzten Hilfsmittel vollständig angegeben habe.

Name, Vorname: Yang Shan
Datum: 31 Mai, 2014

Eidesstattliche Erklärung

Hiermit erkläre ich an Eides Statt, dass die eingereichte Dissertation weder in Teilen noch in Ihrer Gesamtheit einer anderen Hochschule zur Begutachtung vorliegt oder vorgelegen hat und dass ich bisher noch keinen Promotionsversuch unternommen habe.